令和 4 年博士論文

多機能ナノマテリアルによる腫瘍 *in vivo* イメージングと新規治療法の開発

Development of Multifunctional Nanomaterials for *In vivo* Imaging and Novel Therapy of Tumors

名古屋大学大学院　工学研究科
生命分子工学専攻　博士後期課程

Luo Minchuan

Abstract

Strategies enabling the development of imaging probes with the function of novel photo-assisted therapy have provided potential tools for precise diagnosis and treatment of tumors. In this thesis, we first review biomedical imaging modality and advanced noninvasive therapies of tumors, and summarize representative nanomaterials. Then, we report a fluorescent and magnetic nanoprobe (QMNP-RGD) and successfully demonstrate that QMNP-RGD can be efficiently delivered into U87MG cells and used for fluorescence/magnetic resonance (MR) bimodal imaging. Besides, we also developed a multifunctional nanoprobe (BCGCR) integrating fluorescence/MR bimodal imaging and photothermal-enhanced chemodynamic therapy (CDT) of the targeted tumor, which is produced by covalent conjugation of bovine serum albumin (BSA)-stabilized CuS/Gd_2O_3 nanoparticles (NPs) with Cy5.5 fluorophore and tumor-targeting ligand RGD. We believe that these strategies of integrating various components with respective functions will be beneficial to exploring other advanced nanomaterials for the clinical application of multimodal imaging-guided synergetic cancer therapies.

Keywords: nanomaterial, imaging, photo-assisted therapy, *in vivo*, tumor.

Table of contents

Chapter 1: Preface

1.1 Biomedical imaging technology

Cancer has become a major cause of mortality in this contemporary world. In order to realize the detection and diagnosis of cancer, researches have focused their attention on imaging technology, by which complicated physiological and pathological processes can be monitored. Nowadays, advanced nanoprobes are being widely developed for novel biomedical imaging that can realize the diagnosis of diseased tissues in the early stage without surgery or biopsy. In relative to conventional anatomy-based biomedical imaging, novel biomedical imaging is noninvasive, safe and real-time, which shows great potential in clinical applications.

Due to the highly complicated physiological environment and activities in a living body, high sensitivity and resolution are usually required for novel biomedical imaging. Scientists have developed different imaging modalities and corresponding nanoprobes (Figure 1-1). [1-4] For instance, optical imaging (OI) includes fluorescence imaging (FI), bioluminescence imaging (BLI), chemiluminescence imaging (CLI) et al., which has high sensitivity and is equipped with multicolor for imaging. However, OI suffers from low penetration depth, so it is usually applied to the analysis of shallow tissues in living body. Magnetic resonance imaging (MRI) is able to analyze deep tissues with high spatial resolution, but low sensitivity and high cost are inevitable. Computed tomography (CT), which scans the tissue via X-rays, shows high spatial resolution and unlimited tissue-penetration depth as MRI. But it involves high cost and radiation risk. Positron emission tomography (PET) possesses good penetrability, high intensity and specificity in spite of low spatial resolution, high cost and radiation risk. Photoacoustic imaging (PAI) combines high sensitivity from OI and good penetrability from ultrasound imaging (USI), which has great prospects for application in clinical diagnosis. We will review the applications of these different imaging modalities.

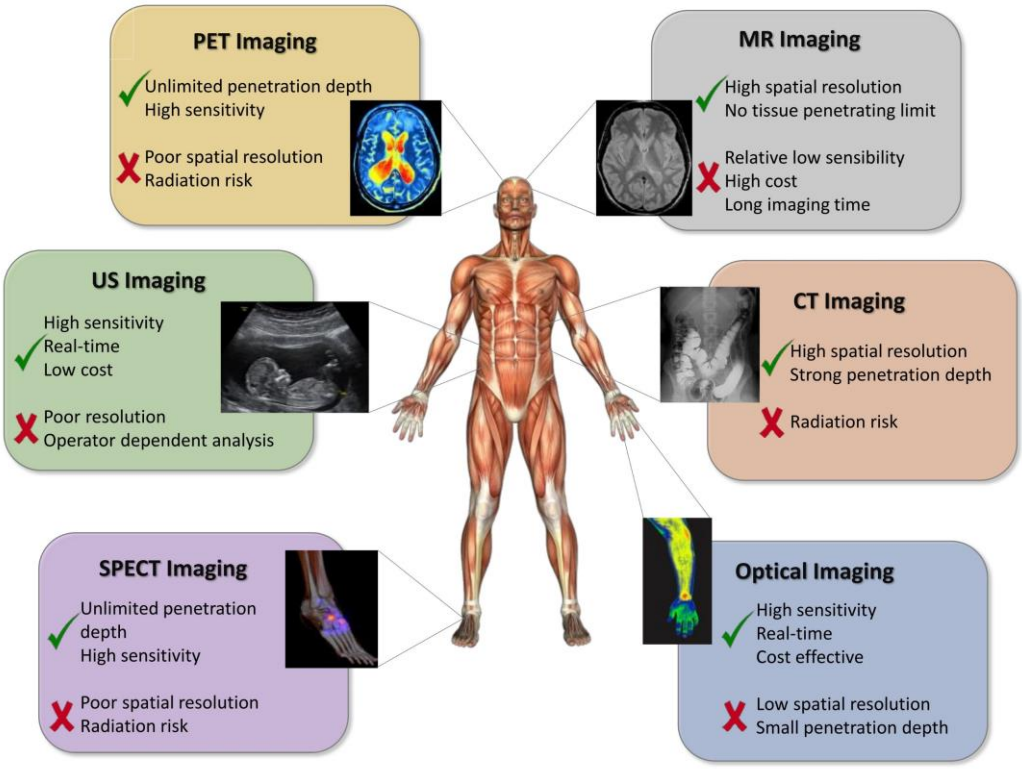

Figure 1-1. Different imaging modalities with respective strengthens and weaknesses (reprinted from ref [4]).

1.1.1 Optical imaging

FI, a convenient, low-cost and noninvasive OI technology, can provide the signal with high sensitivity [5]. However, FI suffers from low spatial resolution and poor penetrability. Therefore, it's widely applied to the analysis of *in vitro* cells and superficial tissues in living body in the early stage. There are two common ways to the development of fluorescent materials. One of them is to produce inorganic nanomaterials with fluorescence emission such as noble metal nanoclusters [6, 7] and quantum dots (QDs) [8-10]. Li et al. designed a kind of oligonucleotide-templated silver nanoclusters (AgNCs) via a facile one-pot process, and confirmed the internalization into MCF-7 cancer cells with red emission (Figure 1-2a). [11] Our group labeled Adipose tissue-derived stem cell (ASC) by commercial CdSe QDs with the help of octa-arginine peptide (R8) and achieved the *in vivo* fluorescence imaging in mice (Figure 1-2b). [12] The other way is to utilize organic fluorophores. [13] Zhu et al. incorporated two types of organic dyes into polymeric chains via an emulsion

polymerization method. [14] The produced nanoparticles exhibited red or green fluorescence upon exposure to UV (< 400 nm) or visible (> 420 nm) light, which made HEK293 cells show the corresponding fluorescence after transduction. In order to obtain images with deep tissue penetration, researchers have developed fluorescent materials with emission values in the near infrared range (NIR: NIR-I: approximately 700-900 nm, NIR-II: approximately 1000-1600 nm) to reduce the strong absorption, scattering and autofluorescence of the organism. Ultrasmall silver sulfide (Ag_2S) QDs with tunable emission from 500 to 1200 nm were produced by Tang et al., which was applied to FI of tumors in living mice after covalent conjugation of a tumor-targeting molecule RGD (Figure 1-2c). [15] Organic NIR fluorophores have also been developed for the modification of nanoparticles, which endow them with the ability of *in vivo* FI (Figure 1-2d). [16]

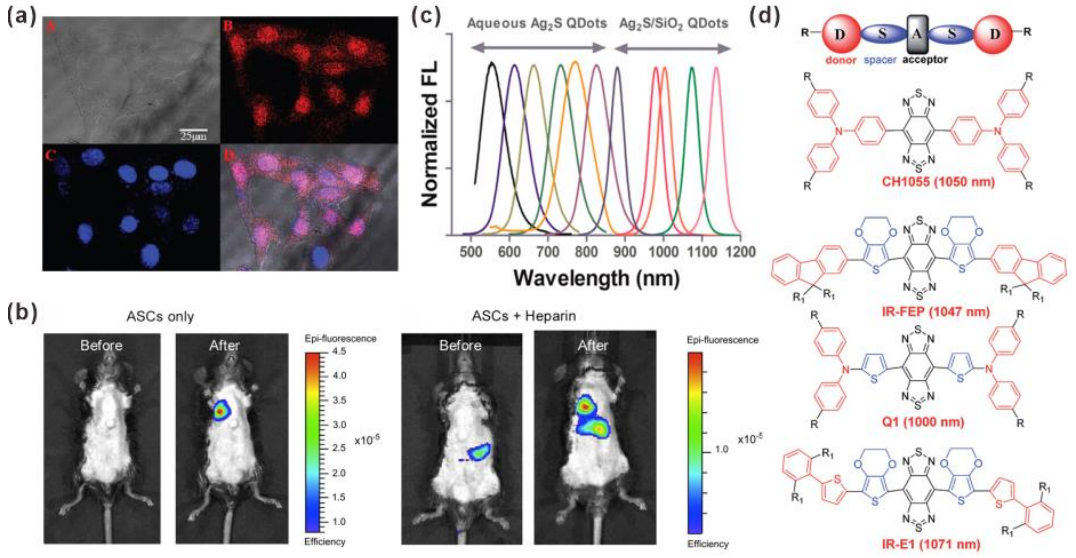

Figure 1-2. FI technology. (a) Intracellular distribution of internalized NC-AS1411-T5-stabilized AgNCs in MCF-7 cells (reprinted from ref [11]). (b) The *in vivo* fluorescence images of mice with acute liver failure transplanted with ASCs labeled with QDs800 in combination without or with heparin before laparotomy (reprinted from ref [12]). (c) Normalized emission spectra of Ag_2S QDs and Ag_2S/SiO_2 QDs (reprinted from ref [15]). (d) Some small organic NIR-II fluorophores (reprinted from ref [16]).

In comparison with FI, BLI has the deeper penetration depth and higher

signal-to-noise ratio due to lack of extra excitation. [17] The mechanism of BLI is to produce organic molecules with emission via the reaction of luciferase and fluorescein substrates. One strategy for BLI of tumors is based on the enzyme digestion, which is to create fluorescein substrates by the specific enzyme overexpressed in tumors. A probe Gly-Gly-Arg-D-aminoluciferin (GGR-AmLuc) was designed by Chen et al., which converted into D-aminoluciferin (AmLuc) by a kind of serine protease-urokinase-type plasminogen activator (uPA). This AmLuc with BL emission could be successfully observed at firefly luciferase-transfected MDA-MB-231 tumors in living mice. [18] Zhou et al. produced a peptide-linked amphiphilic block copolymer-based probe (PABC), which could be activated by fibroblast activation protein (FAP) and applied to the BLI of FAP *in vivo*. The high sensitivity enabled persistent BLI of tumors in living mice compared with free D-luciferin. [19]

1.1.2 Magnetic resonance imaging

As a widely used clinical imaging technology, MRI has high spatial resolution, deep tissue penetration and good soft tissue contrast. [20] The mechanism of imaging is related to the response of spinning nucleus (mainly protons) to an external magnetic field. There is a large quantity of protons in water molecules, proteins and fat from the human body, which results in the high background signal and limits the sensitivity. Hence, appropriate MR contrast agents (CAs) are required to intensify the contrast between pathological tissues and normal tissues.

Currently, most developed MR CAs are gadolinium (Gd), manganese (Mn) or iron (Fe)-based complexes and nanomaterials. [21-24] Gd chelates are able to decrease the spin-lattice relaxation time (T_1) of surrounding water protons, resulting in brighter T_1-weighted MR signals. The approval of $[Gd(DTPA)(H_2O)]^{2-}$ in 1988 promotes the development of clinical MRI worldwide (Figure 1-3a). [21] Cai et al. conjugated Gd-DTPA on Recombinant human heavy chain (H-chain) ferritin (HFn), and achieved MRI of MDA-MB-231 tumors in living mice. [25] Compared with Gd complexes, Gd-based nanoparticles usually has a higher longitudinal relaxivity (r_1)

due to the spatial confinement of the closely packed Gd nanoparticles, which imped the rotation and prolong the tumbling time (τ_R). [26] Excellent MR nanoprobes with outstandingly high relaxivities as 68.02 mM^{-1} s^{-1} and 39.08 mM^{-1} s^{-1} respectively was designed by encapsulating Gd_2O_3 nanoparticles within functionalized PEG, which led to a significant MRI enhancement *in vivo* (Figure 1-3b). [27, 28]

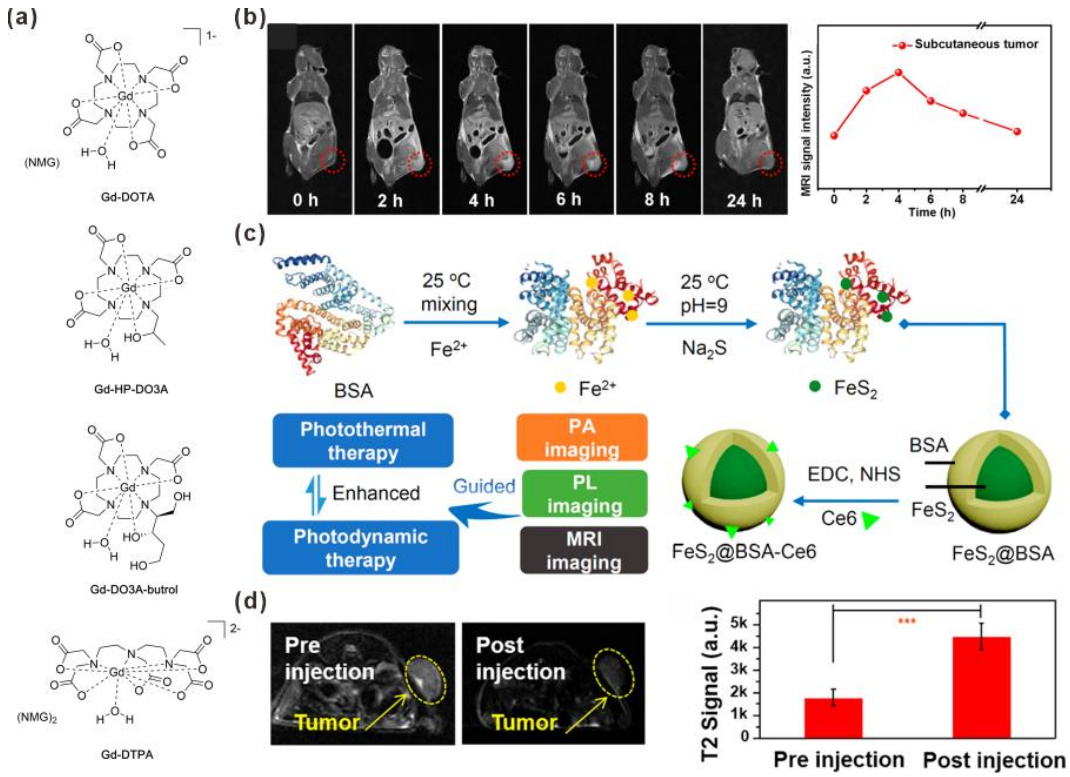

Figure 1-3. MRI technology. (a) Commercially approved Gd complexes as T_1 CAs (NMG = meglumine, reprinted from ref [21]). (b) *in vivo* MR images of subcutaneous 4T1 tumor-bearing mice pre- and post-intravenous administration of folate-PEGylated SiO_2@Gd_2O_3:5%Yb^{3+}/2%Er^{3+}/6%Li^+ CDSNPs (20 mg kg^{-1}) measured at various times and MRI signal intensity variation curve of the tumoral site (reprinted from ref [28]). (c) Synthetic route and applications of FeS_2 nanodots (reprinted from ref [31]). (d) MR images and (f) quantified MR signals of 4T1 tumor-bearing nude mice before and 8 h after iv injection of FeS_2@BSA-Ce6 nanodots (3.5 mg/kg Ce6 and 12 mg/kg FeS_2, reprinted from ref [31]).

In contrast to Gd-based MR CAs, Fe-based ones has lower cytotoxicity and better biocompatibility. Most Fe-based NPs are T_2-weighted MR CAs, which generates strong T_2-negative MR contrast and reduces the brightness of the target. [29] Our

group used a positively charged superparamagnetic iron oxide (SPOI) NPs (TMADM) to label ASCs and achieved *in vitro* MRI of them. [30] Jin et al. designed a facile method for synthesis of ultrasmall FeS_2 nanodots, which possessed a high r_2 relaxivity (85.36 mM^{-1} s^{-1}) for T_2-weighted MRI of 4T1 tumors in living mice (Figure 1-3c&d). [31] Nevertheless, Fe-based NPs are limited in the clinical application because of the dark signals, which means it's hard to distinguish early-stage tumors and hypointense tissues. Therefore, Mn-based NPs is an alternative as T_1-weighted MR CAs, which generates a bright signal against Fe-based ones. Besides, Mn has the lower distinct toxicity *in vivo* than Gd. Nanomaterials can be endowed with the magnetic property by doping or coating Mn compounds such as MnS or MnO_2, which exhibited good compatibility for *in vivo* MRI. [32-35]

1.1.3 Computed tomography

High-resolution three-dimensional (3D) tomographic images can be obtained by CT, based on the difference of tissues towards the absorption and transmissivity of X-rays. [36] It's difficult for soft tissues to absorb X-rays compared with hard tissues like bones, so CT is not sensitive enough for soft tissues like tumors. Some heavy atoms with large attenuation coefficients towards X-rays, such as barium (Ba), and iodine (I), have been clinically developed to enhance CT contrast for the detection of tumors and other diseases. [37, 38] For example, Wang et al. designed an acidic pH/glutathione (GSH) dual-stimuli activatable nanoprobe via the biocompatible CBT condensation reaction, which was able to condensate and self-assemble into NPs in the tumor microenvironment (TME) (Figure 1-4a). [37] At 0.5 h post-injection of this probe with a low dose (21.79 mg I/kg), 4T1 tumor tissues exhibited enhanced CT contrast against that from the control group (Figure 1-4b&c). PEGylated $BaGdF_5$ NPs were designed by Wang et al. via a hydrothermal method, which showed good X-ray attenuation properties for CT imaging of VX2 tumors in living mice. [38]

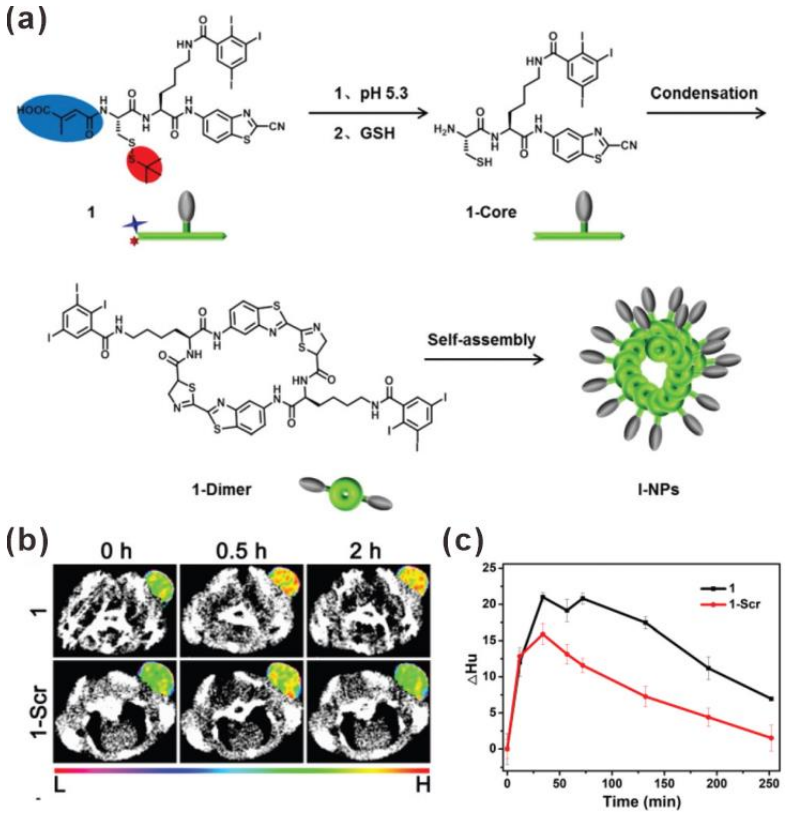

Figure 1-4. CT technology. (a) Schematic illustration of a dually pH/GSH-activatable condensation and self-assembly of I-NPs. (b) CT imaging of 4T1 tumor-bearing living mice at 0, 0.5 and 2 h after intravenous (i.v.) injections of 1 (upper) or 1-Scr (lower). (c) CT contrast enhanced density (ΔHu) of tumor at different time intervals (reprinted from ref [37]).

1.1.4 Positron emission tomography

PET is a radionuclide imaging technology that uses isotopes such as ^{11}C, ^{18}F and ^{64}Cu to generate imaging signals, which is highly sensitive and specific, penetrable and quantifiable. [39, 40] Cheng et al. developed radiolabeled constructs (^{89}Zr-Df-MCL) by reassembling cancer cell membranes with Tween-80 into multicompartment membrane-derived liposomes (MCLs) and conjugating ^{89}Zr via deferoxamine chelator. [41] ^{89}Zr-Df-MCL exhibited excellent radiochemical stability for PET imaging of *in vivo* 4T1 tumors. Hu et al. designed an enzyme-activatable probe (P-CyFF-^{68}Ga) with its cold probe (P-CyFF-Ga) for NIR fluorescence/PET bimodality imaging of enzymatic activity (Figure 1-5a). [42] P-CyFF-^{68}Ga and P-CyFF-Ga were able to be converted into dephosphorylated CyFF-^{68}Ga and

CyFF-Ga via alkaline phosphatase (ALP), and subsequently assemble into fluorescent and radioactive NPs (NP-^{68}Ga) together, which was prone to anchoring on the ALP-positive HeLa cell membrane and enriched NIR fluorescence and radioactivity (Figure 1-5b-d).

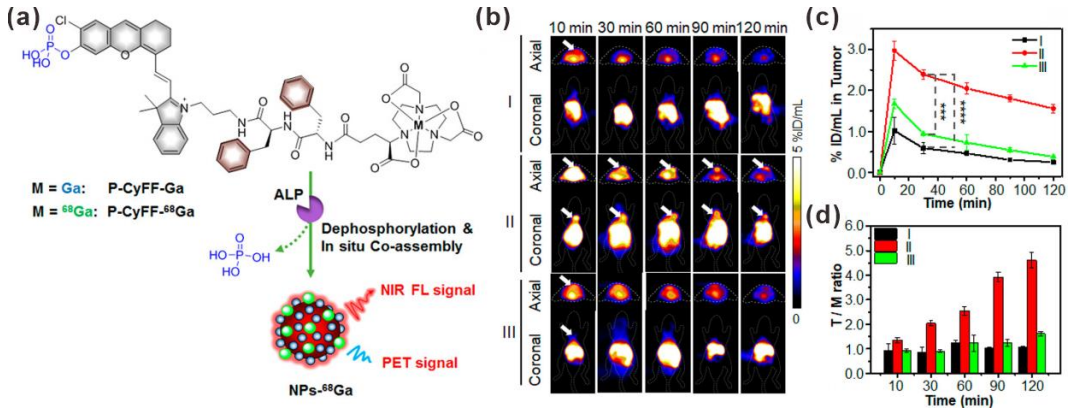

Figure 1-5. PET technology. (a) Schematic illustration of ALP enabled fluorogenic reaction and in situ coassembly of NIR and radioactive NPs for *in vivo* imaging (b) PET imaging of HeLa tumor in mice at 10, 30, 60, 90, and 120 min post-injection. White arrows indicate the tumor sites. (c) Quantification of tumoral radioactivity (%ID/mL) and (d) Tumor-to-muscle (T/M) ratios at the indicated time point post-injection: (I) i.v. injection of P-CyFF-^{68}Ga (~7.4 MBq); (II) i.v. injection of P-CyFF-^{68}Ga (~7.4 MBq,) and P-CyFF-Ga (50 μM, 200 μL,); (III) i.v. injection of P-CyFF-^{68}Ga (~7.4 MBq) and P-CyFF-Ga (50 μM, 200 μL) at 30 min after i.t. injection of Na_3VO_4 (10 mM, 50 μL) (reprinted from ref [42]).

1.1.5 Photoacoustic imaging

PAI is a novel imaging technology that combines optical and ultrasound imaging. [43] The mechanism is that endogenous substances (hemoglobin and melanin) or exogenous CAs absorb pulsed laser light, convert into thermal energy via non-radiative transition, induce thermoelastic expansion of the surrounding medium, and release ultrasonic signals, which can be detected by the ultrasound sensor and be transferred into the image. Compared with OI, PAI can provide information with deeper tissue penetration and superior spatial resolution *in vivo*. However, high background signals of PAI result from the absorption of light by tissues. Researchers are fabricating various PA probes to improve the contrast and sensitivity. [44, 45]

Tian et al. presented a single diagnostic nanoplatform named carbon nitride nanoparticles (CN-NPs) for efficient NIR-II PAI by integrating an aromatic compound (PTCDA) with a large π-structure into melem via high-temperature polymerization (Figure 1-6a). [46] The accumulation and metabolism of CN-NPs *in vivo* could be monitored using PAI in real time (Figure 1-6b). Lucero et al. reported a PAI-based companion diagnostics (CDx) (PACDx) for the selective recognition of elevated glutathione (GSH) in a lung cancer model (Figure 1-6c). [47] Mice bearing lung xenografts could be identified by PAI, and they realized the imaging of GSH in orthotopic lung cancer and liver metastasis models using PACDx (Figure 1-6d).

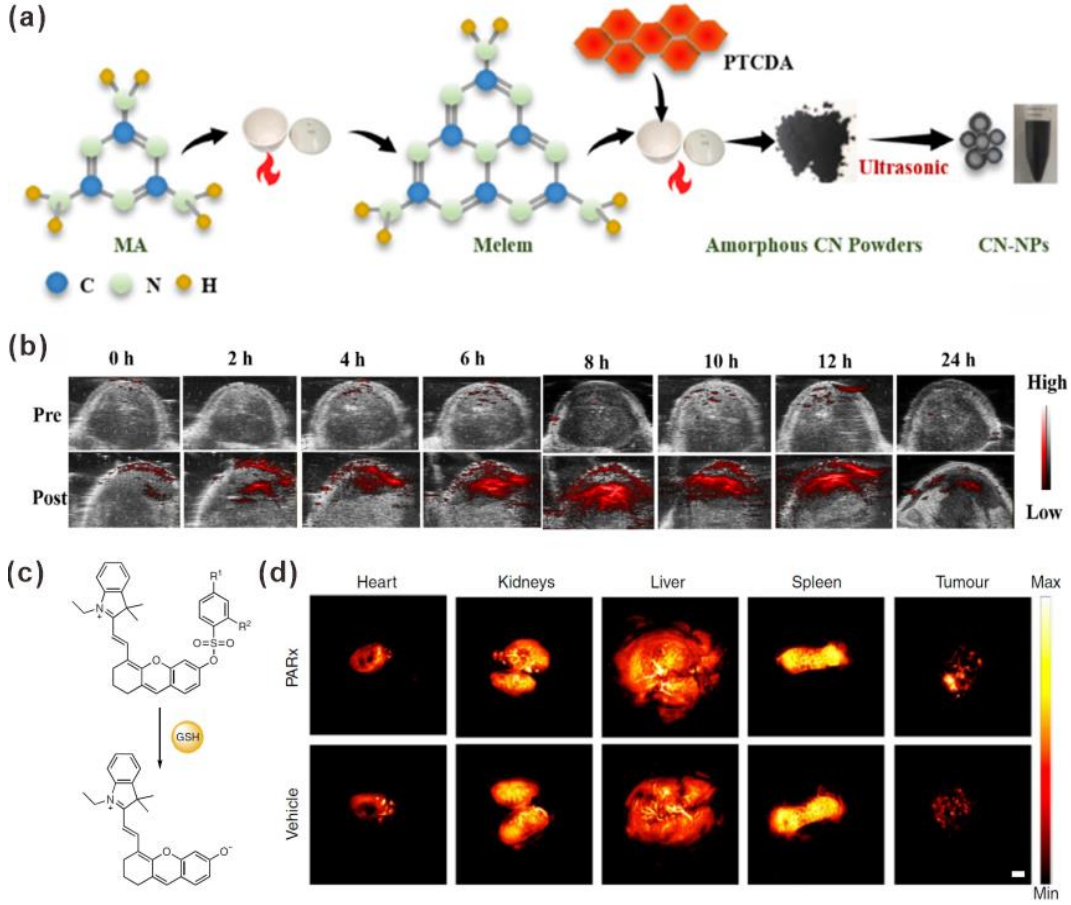

Figure 1-6. PAI technology. (a) Schematic diagram for the preparation of CN-NPs. (b) PA images of the mice at 0, 2, 4, 6, 8, 10, 12, and 24 h after i.v. injection of CN-NPs (reprinted from ref [46]). (c) General schematic for GSH-responsive PACDx. (d) Representative *ex vivo* PA images of heart, kidneys, liver, spleen and tumor irradiated at 680 nm, after systemic injection of PARx (400 μM, 10% DMSO/PBS, retro-orbital injection) or vehicle. Scale bar = 2 mm (reprinted from ref [47]).

1.1.6 Bi- or Multi-modal imaging

Due to the inherent limitations of each imaging modality for *in vivo* analysis, it is difficult for mono-modal imaging to simultaneously meet the requirements of sensitivity, spatial resolution and tissue penetration depth. Therefore, the design of multimodal imaging probes that integrates two or more imaging modalities is beneficial to obtaining accurate information, and will become the trend of the development of imaging CAs for precise diagnostics in the future. The basic idea is to integrate components with respective functions by synthesis, doping or modification. Yan et al. designed a small-molecule-based activatable NIR fluorescence and MR bimodal probe (P-CyFF-Gd) for molecular imaging (Figure 1-7a). [48] They demonstrated that P-CyFF-Gd could be activated by endogenous ALP overexpressed on the membrane tumor cells, producing membrane-localized assembled NPs, which achieved simultaneous enhancements in NIR fluorescence and r_1 relaxivity for high-sensitivity, high-spatial-resolution and real-time imaging of the ALP activity in tumors of living mice (Figure 1-7b&c). Shi et al. developed a tumor-targeted and matrix metalloprotease-2 (MMP-2)-activatable nanoprobe (T-MAN) by covalent modification of Gd-doping CuS micellar nanoparticles with cRGD and an MMP-2-cleavable fluorescent substrate, which displayed low-background FI and high-spatial-resolution MRI of gastric tumors and lymph node (LN) metastasis in living mice. [49]

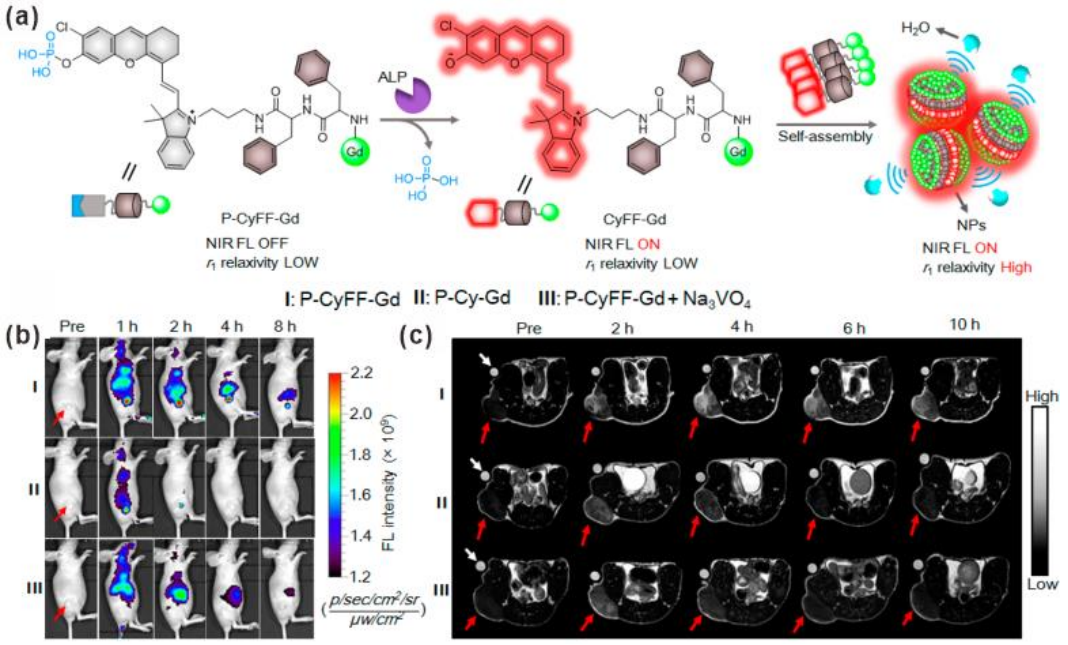

Figure 1-7. Bimodal imaging technology. (a) Chemical structure of P-CyFF-Gd and ALP-induced fluorogenic reaction and in situ self-assembly of P-CyFF-Gd into NPs. (b) Fluorescence images of mice receiving i.v. injection of P-CyFF-Gd (I), P-Cy-Gd (II), or P-CyFF-Gd (50 μM, 200 μL) together with i.t. injection of 10 mM Na_3VO_4 (50 μL) (III) at 0, 1, 2, 4, and 8 h. (c) T_1-weighted MR images of HeLa tumor-bearing mice receiving intraperitoneal (i.p.) injection of P-CyFF-Gd (I), P-Cy-Gd (II), or P-CyFF-Gd (0.015 mmol kg^{-1} Gd^{3+}) together with i.t. injection of Na_3VO_4 (10 mM, 50 μL) (III). Images were acquired before (Pre), 2, 4, 6, and 10 h after injection using TE/TR = 15/446 ms at 1 T (reprinted from ref [48]).

1.2 Novel cancer therapies

At present, cancer therapies remain a vital challenge in the clinical application because conventional therapeutic strategies including surgery, chemotherapy and radiotherapy, involve inevitable weaknesses. They are invasive, poorly specific and lowly efficient. Besides, they cause substantial damage to normal cells and immune cells, leading to adverse side effects towards main organs, which becomes counterproductive to recovery and ultimately results in the overall debilitation of the patient. By virtue of the development of various NPs with unique physicochemical properties, novel therapies based on nanomedicines have provided hopeful

opportunities for cancer treatment (Figure 1-8). [50-52] For example, Magnetic hyperthermia therapy and photothermal therapy (PTT) are able to heat and thermally ablate tumor tissues by virtue of external alternating magnetic field or laser irradiation. Photodynamic therapy (PDT), a type of light-triggered therapy, can convert oxygen into reactive oxygen species (ROS) and causes oxidative damage to tumor cells with the help of photosensitizer. Sonodynamic therapy (SDT) activates sonosensitizers to produce excessive ROS via certain acoustic cavitation effects under ultrasound (US), resulting in cancer cell apoptosis. Likewise, chemodynamic therapy (CDT) is a continuous chemical process that converts H_2O_2 in the TME into toxic ROS, generally based on Fenton or Fenton-like reactions. We will introduce novel therapy strategies in the following.

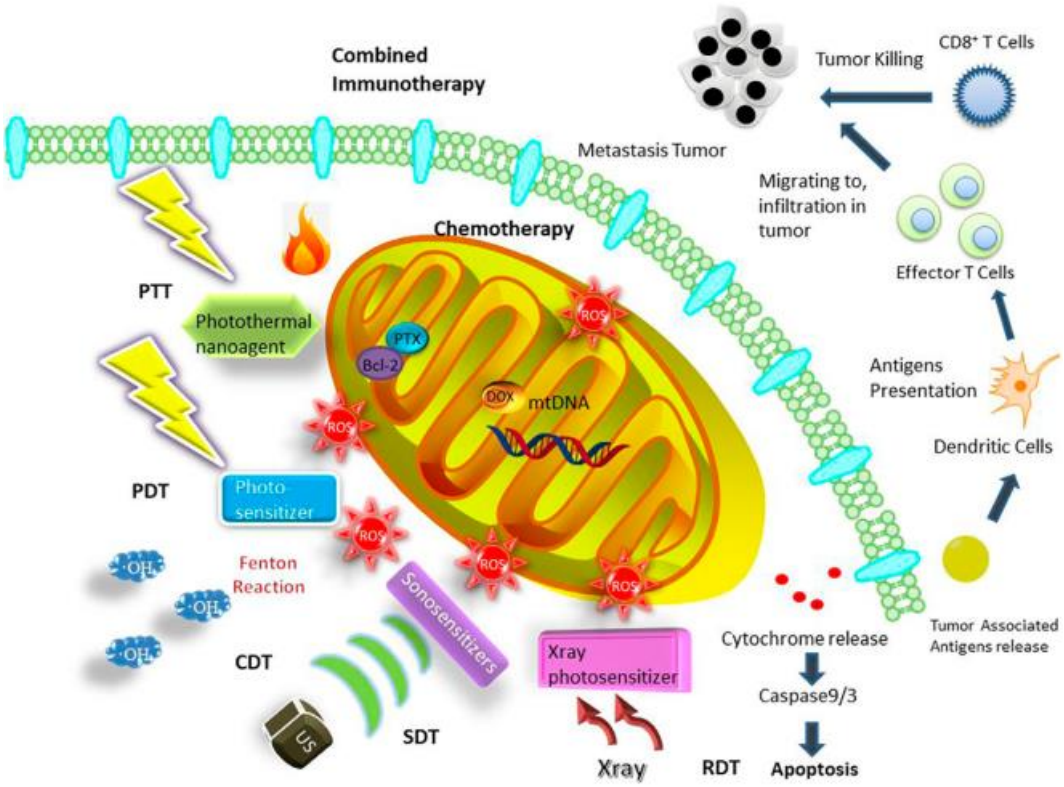

Figure 1-8. Scheme of different therapies based on various nanomaterials (reprinted from ref [50]).

1.2.1 Photothermal therapy

PTT triggers photo-heat conversion to generate localized hyperthermia, resulting in tumor ablation. It's highly spatial-temporal, noninvasive and reduced damage to normal tissues. PTT is generally conducted by exposure under laser irradiation

assisted with photothermal agents, which possess strong and broad absorption, high photothermal conversion efficiency (PCE), excellent photostability and superb biocompatibility, such as organic molecules, noble metal NPs, black phosphorus and carbon nanomaterials. [53-55] Metal sulfides are emerging as potential noble metal photothermal agents. Yang et al. propose a ultrasmall-sized iron-based NPs (FeS@BSA QDs) via albumin-mediated biomimetic synthesis. [56] FeS@BSA QDs exhibited strong absorption at 650 nm and increased temperature under laser irradiation (Figure 1-9a). After i.v. injection of FeS@BSA QDs and subsequent laser irradiation, the temperature of tumor in mice gradually increased, which was much higher than the one of PBS plus laser treated (Figure 1-9b&c). This temperature was high enough to ablate tumors by monitoring relative tumor volume changes over 16 days after treatment (Figure 1-9d&e). Similarly, MoS_2 exhibits broad absorption and the ability of photo-heat conversion under laser irradiation. [57] It could be used for PTT of Hela tumors in living mice after being stabilizing by BSA and PEG. Different from FeS and MoS_2, CuS NPs has strong NIR absorption, which maybe serve as the appropriate frequency for PTT because of high energy of photons, low absorption and scattering by tissues, and deep penetration depth. Therefore, various CuS NPs with high PCE were developed for PTT of tumors *in vivo*. [58-60]

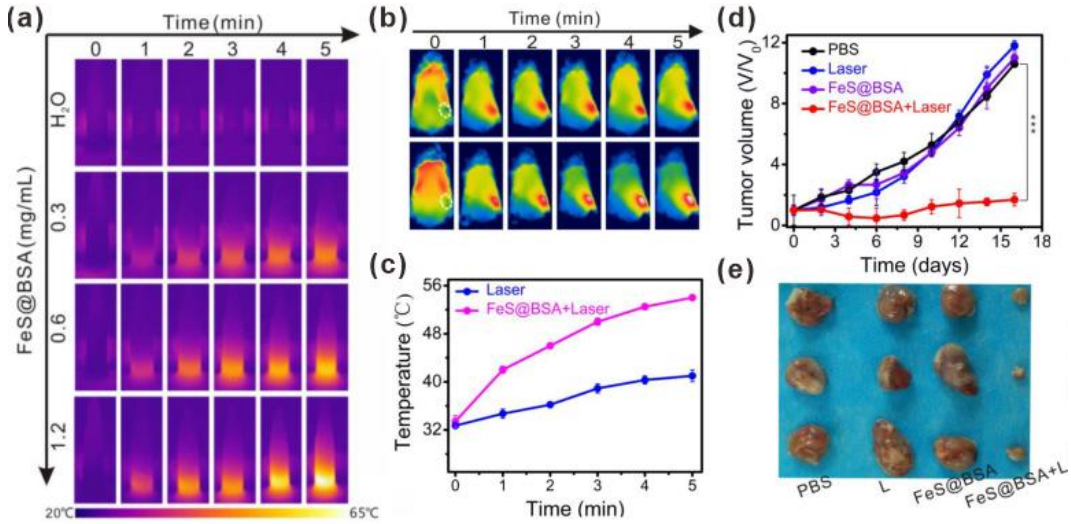

Figure 1-9. PTT. (a) Time (0-5 min) and concentration (0.3-1.2 mg/mL)-dependent infrared thermal images of FeS@BSA QDs before and after laser irradiation (660 nm, 2 W/cm^2). (b) Photothermal images of 4T1 tumor-bearing mice injected with PBS or

FeS@BSA QDs plus laser irradiation, respectively. (c) The temperature growth curve during 5 min of laser irradiation. (d) Relative tumor volume changes of mice in four groups (PBS, laser irradiation, FeS@BSA QDs, and FeS@BSA QDs plus laser irradiation) over 16 days. (e) Photos of the excised tumors from mice on the day 16 after different treatments (reprinted from ref [56]).

1.2.2 Photodynamic therapy

PDT causes oxidative damage to tumor cells by generating cytotoxic ROS such as superoxide ($\cdot O_2^-$), singlet oxygen ($^1O_2$) or hydroxyl ($\cdot$OH) via the reaction of activated photosensitizers (PSs) and oxygen under the laser irradiation, which is also noninvasive and highly selective, and has been exploited as a burgeoning cancer treatment strategy. [61-63] To date, common PSs comprise inorganic nanomaterials and organic molecules. Semiconductor nanomaterials are able to produce electron-hole pairs under laser irradiation, and these separated electrons and holes further convert H_2O and O_2 into ROS. Besides, some organic molecules with large π-conjugated structure possess the ability to generate $^1O_2$ under NIR light excitation. Li et al. proposed metal-free helical nanofibers produced by coassembly of a cationic porphyrin and adenosine triphosphate (ATP) for PDT in aqueous solution (Figure 1-10a). [64] The porphyrin-ATP nanofibers showed enhanced tumor-site delivery of PSs owing to overexpressed extracellular ATP. Good tumor therapeutic efficacy based on PDT resulted from the enzyme-induced release of PSs via biodegradation of ATP (Figure 1-10b-d). An et al. synthesized a multifunctional molecule (1-RGD), in which pheophorbide a (PPa) was connected for FI and PDT. [65] The special ability of PPa to generate $^1O_2$ under NIR excitation enabled the elimination of U87MG tumor tissues in living mice.

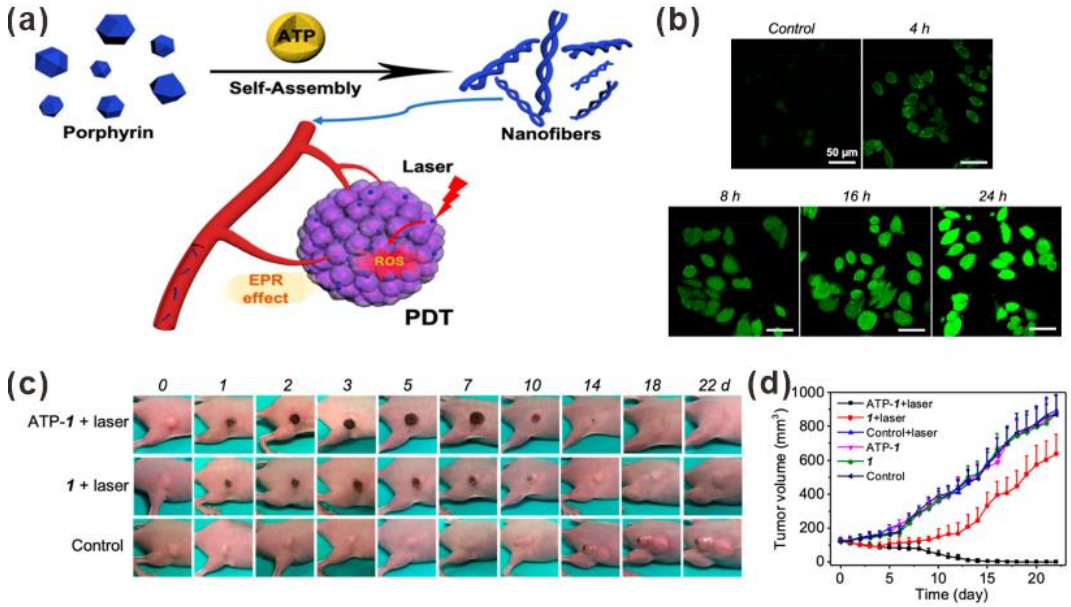

Figure 1-10. PDT. (a) Schematic illustration of ATP-templated self-assembly of porphyrin for precise PDT. (b) FI of cells showing the ROS generation via incubation of 1-ATP nanofibers and DCFH-DA followed by irradiation. (c) Representative photos of tumor-bearing mice after treatment. The mice were injected with 1-ATP nanofibers, unencapsulated porphyrin 1, or 5% glucose (control group). At 4 h post-injection, tumor sites were irradiated (635 nm, 0.3 W cm^{-2}, 10 min). (d) The variation of tumor volume after treatment (reprinted from ref [64]).

1.2.3 Sonodynamic therapy

SDT uses ultrasound to excite sonosensitizers with the generation of cytotoxic ROS towards tumors, which has many advantages over PDT: US is able to penetrate deeper tissues than light in human body and the safe US has been widely used in clinical diagnosis. [66-68] Various inorganic nanoparticles and organic molecules have been developed as sonosensitizers, including TiO_2 NPs, Si NPs, protoporphyrin IX (PpIX), and chlorin e6 (Ce6). [69] Sun et al. designed a hybrid FeCuS-lipid NP (AIBA@FeCuS-FeCO) for US-induced synergistic therapy of orthotopic gastric tumors *in vivo*, which was integrated by free radical initiators (AIBA), radical-sensitive CO donors ($Fe_3(CO)_{12}$), and radical-degradable FeCuS NPs (Figure 1-11a). [70] After US irradiation, this nanomaterial could be degraded with the release of cytotoxic AIBA radicals, CO, Fe^{2+}, and Cu^{2+}, permitting hydroxyl radical

generation and causing the ferroptosis of tumor (Figure 1-11b). Moreover, the subsequent introduction of disulfiram (DSF) further chelated with the liberated Cu^{2+} into toxic bis(N,N-diethyl dithiocarbamato)copper(II) chelates to ablate orthotopic gastric tumors thoroughly via a synergetic therapeutic effect (Figure 1-11c). Chen et al. fabricated an organic sonosensitizer via integration of 8-arm-PEG-NH_2, 1,2,4,5-tetrakis(4-carboxyphenyl)-porphyrin (TCPP) and Gd^{3+} into Gd-PPNs, in which TCPP possess excellent SDT efficiency to inhibit the growth of pancreatic tumor growth in living mice. [71]

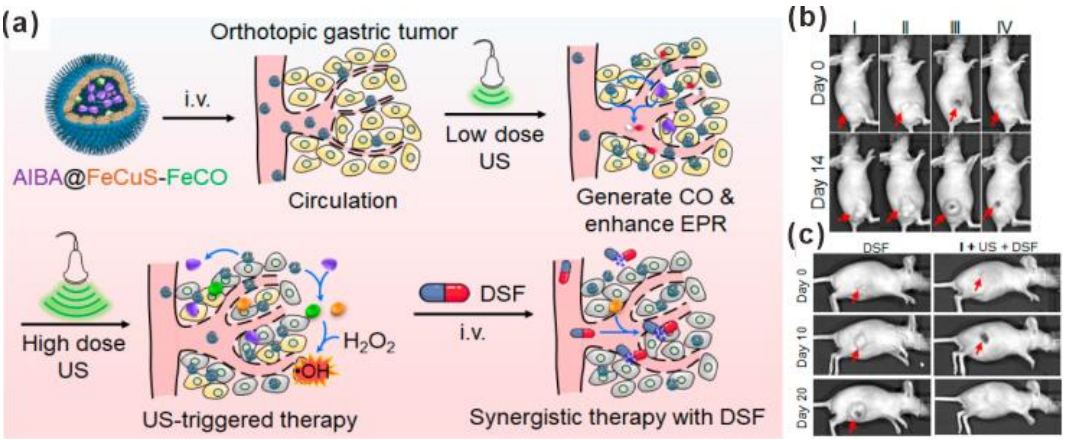

Figure 1-11. SDT. (a) Schematic illustration of the process of AIBA@FeCuS-FeCO and DSF for US-induced synergistic therapy of orthotopic gastric tumors *in vivo*. (b) Photographs of mice before (day 0) and after (day 14) treatments with I, PBS; II, AIBA@FeCuS-FeCO; III, US treatment; IV, AIBA@FeCuS-FeCO + US. (c) Photographs of mice on days 0, 10, and 20 after treatments with DSF only or AIBA@FeCuS-FeCO (I) and US plus DSF (reprinted from ref [70]).

1.2.4 Chemodynamic therapy

Compared with PDT and SDT, external energy input is not necessary in the case of CDT. CDT employs endogenous H_2O_2 in the TME to produce cytotoxic ROS via Fenton or Fenton-like reactions, thus Fe, Mn, Cu-based NPs are generally developed for this purpose. [72, 73] For example, adenosine triphosphate (ATP)-responsive Fenton NPs (GOx@ZIF@MPN) was designed by Zhang et al. via incorporating glucose oxidase (GOx) in zeolitic imidazolate framework (ZIF) and decorating metal polyphenol network (MPN) for tumor ablation. [74] The shell MPN was degraded in

the ATP-overexpressed TME with the release of Fe(III), tannic acid (TA) and the internal GOx. GOx reacted with the endogenous glucose to generate abundant H_2O_2, and TA reduced Fe(III) into Fe(II) simultaneously, which promoted the Fenton reaction to produce ample ROS for CDT of tumors *in vivo*. However, Fe^{2+}-based nanomaterials are not efficient enough in the weakly acidic TME (pH 6.5-6.9) and the amount of ROS produced is largely limited by the low reaction rate (55 M^{-1} s^{-1}) even in an ideal pH condition. [75] Cuprous ion (Cu^{+}) is an alternative due to the much higher reaction rate (~1 × 10^4 M^{-1} s^{-1}) and the feasibility of its application in weakly acidic and neutral media. [76] Considering the existence of sufficient endogenous biothiols (e.g., ~10 mM glutathione [GSH]) in cancer cells, Cu^{+} can be produced via the redox between cupric ion (Cu^{2+}) and GSH. Ma et al. prepared copper-amino acid mercaptide NPs (Cu-Cys NPs) by the facile self-assembly of L-cysteine and Cu^{2+} (Figure 1-12a). [77] After endocytosis into tumors, the Cu-Cys NPs could react with local GSH and reduce Cu^{2+} to Cu^{+}, which consumed H_2O_2 to generate ROS via a Fenton-like reaction for the apoptosis of tumors in living mice (Figure 1-12b&c).

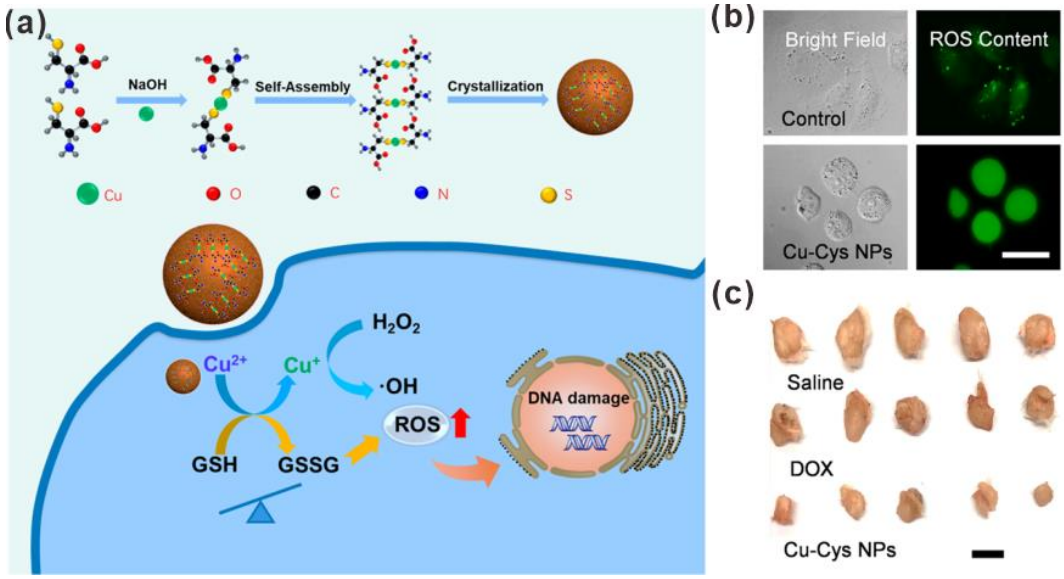

Figure 1-12. CDT. (a) Schematic of the preparation of Cu-Cys NPs and the copper-containing nanomaterial induced chemodynamic therapy. (b) ROS staining of ADSCs and MCF-7R cells treated by Cu-Cys NPs or not. Scale bar, 50 μm. (c) Photo of resected tumors from MCF-7R tumor-bearing mice after 40 days of treatment. Scale bar, 1 cm (reprinted from ref [77]).

1.2.5 Synergetic therapies

In the actual application, single modality of therapy maybe not thorough enough to eliminate tumors by administering a low dose of nanomaterials. Taking biocompatibility into consideration, it's unlikely to use drugs with extremely high dose in spite of the complete curative efficiency. Hence, synergetic therapies have been attracted much attention to promote the therapeutic effect. Similar to the bi- or multimodal imaging mentioned before, components with respective functions are integrated for this purpose. Hao et al. designed Prussian blue analogues (PBAs) with superior tumor synergetic therapeutic effects by simply mixing cobalt nitrate, sodium citrate and potassium hexacyanoferrate(III) (Figure 1-13a). [78] PBAs exhibited not only high PCE (41.44%) and photodynamic effect, but also chemodynamic effect resulted from the Fenton reaction and ferroptosis, which was beneficial to tumor ablation without obvious toxicity *in vivo* (Figure 1-13b&c). a second NIR photothermal Fenton nanocatalyst (PFN) was produced by Sun et al. via capsulation of MnO_2 and CuS NPs in the template HSA. [79] CuS NPs from PFN had strong NIR absorption and enabled the generation of localized heat under laser irradiation, which enabled PTT and intensified the nanocatalyst-induced Fenton-like reaction for CDT of tumors in living mice.

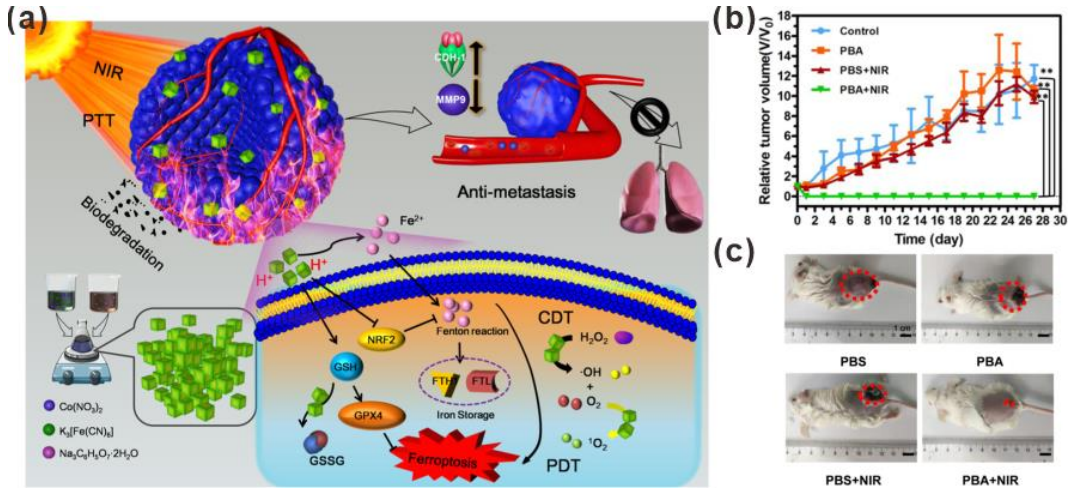

Figure 1-13. Synergetic therapies. (a) Schematic of the preparation of biodegradable PBA NPs and PTT/PDT/CDT therapeutic effect. (b) The variation of relative tumor volume after treatment of PBS, PBA, PBS + NIR or PBA + NIR. (c) Representative

photos of mice at 27-day after respective treatment (reprinted from ref [78]).

1.3 Application prospects and challenges

We summarized recent developments of various imaging modalities and advanced therapies of tumors. Despite these excellent findings, there are several challenges for nanomaterials that need solving to achieve the nanomaterials-based cancer treatment of human body. The primary risk from nanomaterials in the clinical application is the toxicity. Nanomaterials cannot totally arrive at tumors after administration, although many researches on designing nanosystems with targeting tumors, including passive and active targeting, has been in progress. Therefore, to realize the "zero damage" to normal tissues is still a challenge. Besides, normal tissues are easily damaged in the process of treatment. Similar to the chemotherapy, the highly cytotoxic ROS from dynamic therapy can cause inevitable wound towards main organs. The hypothermia from thermal therapy must do irreversible harm to normal tissues near tumors. Apart from the toxicity, the efficiency of various therapies should be taken into consideration. The penetration depth of laser irradiation is limited, thus it's dispensable to construct photo-based agents with high efficiency for photo-assisted therapy in order to reduce the dose of administration. The generation of ROS responsive to pH tend to be low in the TME, thus pH independent nanocatalysts with high catalytic efficiency should be further created. On the whole, nanomaterials integrating imaging and therapy are expected to bring effective applications in the future.

1.4 References

[1] Zhao, J.; Chen, J.; Ma, S.; Liu, Q.; Huang, L.; Chen, X.; Lou, K.; Wang, W. *Acta Pharm. Sin. B* **2018**, *8*, 320-338.

[2] Han, X.; Xu, K.; Taratula, O.; Farsad, K. *Nanoscale* **2019**, *11*, 799-819.

[3] Morato, Y. L.; Paredes, K. O.; Chamizo, L. L.; Marciello, M.; Filice, M. *Polymers* **2021**, *13*, 2989.

[4] Morato, Y. L.; Marciello, M.; Chamizo, L. L.; Paredes, K. O.; Filice, M. *Magnetic Nanoparticle-Based Hybrid Materials* **2021**, 343-386.

[5] Thomas, J. A. *Chem. Soc. Rev.* **2015**, *44*, 4494-4500.

[6] Tao, Y.; Li, M.; Ren, J.; Qu, X. *Chem. Soc. Rev.*, **2015**, *44*, 8636-8663.

[7] Zhang, L.; Wang, E. *Nano Today* **2014**, *9*, 132-157.

[8] Xu, G.; Zeng, S.; Zhang, B.; Swihart, M. T.; Yong, K.; Prasad, P. N. *Chem. Rev.* **2016**, *116*, 12234-12327.

[9] Cassette, E.; Helle, M.; Bezdetnaya, L.; Marchal, F.; Dubertret, B.; Pons, T. *Adv. Drug Deliver. Rev.* **2013**, *65*, 719-731.

[10] Yukawa, H.; Baba, Y. *Anal. Chem.* **2017**, *89*, 2671-2681.

[11] Li, J.; Zhong, X.; Cheng, F.; Zhang, J.; Jiang, L.; Zhu, J.; *Anal. Chem.* **2012**, *84*, 4140-4146.

[12] Yukawa, H.; Watanabe, M.; Kaji, N.; Okamoto, Y.; Tokeshi, M.; Miyamoto, Y.; Noguchi, H.; Baba, Y.; Hayashi, S. *Biomaterials* **2012**, *33*, 2177-2186.

[13] Sameiro, M.; Gonçalves, T. *Chem. Rev.* **2009**, *109*, 190-212.

[14] Zhu, L.; Wu, W.; Zhu, M.; Han, J. J.; Hurst, J. K.; Li, A. D. Q. *J. Am. Chem. Soc.* **2007**, *129*, 3524-3526.

[15] Tang, R.; Xue, J.; Xu, B.; Shen, D.; Sudlow, G. P.; Achilefu, S. *ACS Nano* **2015**, *9*, 220-230.

[16] Ding, F.; Zhan, Y.; Lu, X.; Sun, Y. *Chem. Sci.* **2018**, *9*, 4370-4380.

[17] Li, J.; Chen, L.; Du, L.; Li, M. *Chem. Soc. Rev.* **2013**, *42*, 662-676.

[18] Chen, Y.; Wu. C.; Wang, C.; Zhang, T.; Hua, Y.; Shen, Y.; Liang, G. *Anal. Chem.* **2021**, *93*, 9970-9973.

[19] Zhou, Y.; Yin, K.; Dong, H.; Yang, S.; Li, J.; Luo, J.; Yang, R. *Anal. Chem.* **2021**, *93*, 3726-3732.

[20] Jun, Y.; Lee, J.; Cheon, J. *Angew. Chem. Int. Ed.* **2008**, *47*, 5122-5135.

[21] Wahsner, J.; Gale, E. M.; Rodríguez-Rodríguez, A.; Caravan, P. *Chem. Rev.* **2019**, *119*, 957-1057.

[22] Caravan, P.; Ellison, J. J.; McMurry, T. J. Lauffer, R. B. *Chem. Rev.* **1999**, *99*, 2293-2352.

[23] Drahoš, B.; Lukeš, I.; Tóth, É. *Eur. J. Inorg. Chem.* **2012**, 1975-1986.

[24] Caspani, S.; Magalhães, R.; Araújo, J. P.; Sousa, C. T. *Materials* **2020**, *13*, 2586.

[25] Cai, Y.; Wang, Y.; Zhang, T.; Pan, Y. ACS Appl. *Nano Mater.* **2020**, *3*, 8771-8783.

[26] Wang, L.; Lin, H.; Ma, L.; Sun, C.; Huang, J.; Li, A.; Zhao, T.; Chen, Z.; Gao, J. *J. Mater. Chem. B* **2017**, *5*, 8004-8012.

[27] Kuang, Y.; Cao, Y.; Liu, M.; Zu, G.; Zhang, Y.; Zhang, Y.; Pei, R. *ACS Appl. Mater. Interfaces* **2018**, *10*, 26099-26107.

[28] Yin, J.; Wang, X.; Zheng, H.; Zhang, J.; Qu, H.; Tian, L.; Zhao, F.; Shao, Y. *ACS Appl. Nano Mater.* **2021**, *4*, 3767-3779.

[29] Chen, R.; Yu, H.; Jia, Z.; Yao, Q.; Teng, G. *Int. J. Nanomed.* **2011**, *6*, 511-519.

[30] Yukawa, H.; Nakagawa, S.; Yoshizumi, Y.; Watanabe, M.; Saito, H.; Miyamoto, Y.; Noguchi, H.; Oishi, K.; Ono, K.; Sawada, M.; Kato, I.; Onoshima, D.; Obayashi, M.; Hayashi, Y.; Kaji, N.; Ishikawa, T.; Hayashi, S.; Baba, Y. *Plos One* **2014**, *9*, 110142.

[31] Jin, Q.; Liu, J.; Zhu, W.; Dong, Z.; Liu, Z.; Cheng, L. *ACS Appl. Mater. Interfaces* **2018**, *10*, 332-340.

[32] Zhao, Y.; Meng, J.; Sheng, X.; Tian, Y. *Adv. Optical Mater.* **2016**, *4*, 1115-1123.

[33] Zhang, M.; Liu, X.; Luo, Q.; Wang, Q.; Zhao, L.; Deng, G.; Ge, R.; Zhang, L.; Hu, J.; Lu, J. *Chem. Eng. J.* **2020**, *389*, 124450.

[34] Li, S.; Zhang, L.; Chen, X.; Wang, T.; Zhao, Y.; Li, L.; Wang, C. *ACS Appl. Mater. Interfaces* **2018**, *10*, 24137-24148.

[35] Huang, H.; Li, K.; Liu, Q.; Zhao, Y.; Xu, H.; Wu, W.; Sun, K.; Ni, J.; Lin, J. *RSC Adv.* **2019**, *9*, 2718-2730.

[36] DeKrafft, K. E.; Xie, Z.; Cao, G.; Tran, S.; Ma, L.; Zhou, O. Z.; Lin, W. *Angew. Chem.* **2009**, *121*, 10085-10088.

[37] Wang, A.; Yin, L.; He, L.; Xia, H.; Chen, F.; Zhao, M.; Ding, J.; Shi, H.

Nanoscale **2018**, *10*, 20126-20130.

[38] Wang, T.; Jia, G.; Cheng, C.; Wang, Q.; Li, X.; Liu, Y.; He, C.; Chen, L.; Sun, G.; Zuo, C. *New J. Chem.* **2018**, *42*, 11565-11572.

[39] Velikyan, I. *Theranostics* **2014**, *4*, 47-80.

[40] Grant, F. D.; Fahey, F. H.; Packard, A. B.; Davis, R. T.; Alavi, A.; Treves, S. T. *J. Nucl. Med.* **2008**, *49*, 68-78.

[41] Yu, B.; Goel, S.; Ni, D.; Ellison, P. A.; Siamof, C. M.; Jiang, D.; Cheng, L.; Kang, L.; Yu, F.; Liu, Z.; Barnhart, T. E.; He, Q.; Zhang, H.; Cai, W. *Adv. Mater.* **2018**, *30*, 1704934.

[42] Hu, Y.; Miao, Y.; Zhang, J.; Chen, Y.; Qiu, L.; Lin, J.; Ye, D. *Nano lett.* **2021**, *21*, 10377-10385.

[43] Su, J. L.; Wang, B.; Wilson, K. E.; Bayer, C. L.; Chen, Y.; Kim, S.; Homan, K. A.; Emelianov, S. Y. *Expert Opin. Med. Diagn.* **2010**, *4*, 497-510.

[44] Wu, D.; Huang, L.; Jiang, M. S.; Jiang, H. *Int. J. Mol. Sci.* **2014**, *15*, 23616-23639.

[45] Wang, L.; Yang, P.; Zhao, X.; Wang, H. *Nanoscale* **2016**, *8*, 2488-2509.

[46] Tian, Y.; Zhao, D.; Huang, X.; Guan, X.; Wang, F.; Wei, X. *ACS Appl. Mater. Interfaces* **2022**, *14*, 7626-7635.

[47] Lucero, M. Y.; Chan, *J. Nat. Chem.* **2021**, *13*, 1248-1256.

[48] Yan, R.; Hu, Y.; Liu, F.; Wei, S.; Fang, D.; Shuhendler, A. J.; Liu, H.; Chen, H.; Ye, D. *J. Am. Chem. Soc.* **2019**, *141*, 10331-10341.

[49] Shi, H.; Sun, Y.; Yan, R.; Liu, S.; Zhu, L.; Liu, S.; Feng, Y.; Wang, P.; He, J.; Zhou, Z.; Ye, D. *Nano Lett.* **2019**, *19*, 937-947.

[50] Gao, Y.; Tong, H.; Li, J.; Li, J.; Huang, D.; Shi, J.; Xia, B. *Front. Bioeng. Biotech.* **2021**, *9*, 720508.

[51] Shen, X.; Liu, X.; Li, T.; Chen, Y.; Chen, Y.; Wang, P.; Zheng, L.; Yang, H.; Wu, C.; Deng, S.; Liu, Y. *Front. Chem.* **2021**, *9*, 746646.

[52] Hao, Y.; Zhang, W.; Gao, Y.; Wei, Y.; Shu, Y.; Wang, J. *J. Mater. Chem. B* **2021**, *9*, 250-266.

[53] Xu, C.; Pu, K. *Chem. Soc. Rev.* **2021**, *50*, 1111-1137.

[54] Liu, S.; Wang, L.; Lin, M.; Liu, Y.; Zhang, L.; Zhang, H. *Chinese J. Polym. Sci.* **2019**, *37*, 115-128.

[55] Chen, Y.; Su, Y.; Hu, S.; Chen, S. *Adv. Drug Deliver. Rev.* **2016**, *105*, 190-204.

[56] Yang, W.; Xiang, C.; Xu, Y.; Chen, S.; Zeng, W.; Liu, K.; Jin, X.; Zhou, X.; Zhang, B. *Biomaterials* **2020**, *255*, 120186.

[57] Zhang, Y.; Xiu, W.; Sun, Y.; Zhu, D.; Zhang, Q.; Yuwen, L.; Weng, L.; Teng, Z.; Wang, L. *Nanoscale* **2017**, *9*, 15835-15845.

[58] Yang, W.; Guo, W.; Le, W.; Lv, G.; Zhang, F.; Shi, L.; Wang, X.; Wang, J.; Wang, S.; Chang, J.; Zhang, B. *ACS Nano* **2016**, *10*, 10245-10257.

[59] Wen, R.; Lv, X.; Yang, T.; Li, Y.; Tang, Y.; Bai, X.; Ke, H.; Shen, J.; Chen, H. *Sci. China Mater.* **2017**, *60*, 554-562.

[60] Zhang, C.; Fu, Y.; Zhang, X.; Yu, C.; Zhao, Y.; Sun, S. *Dalton Trans.* **2015**, *44*, 13112-13118.

[61] Li, X.; Lee, S.; Yoon, J. *Chem. Soc. Rev.* **2018**, *47*, 1174-1188.

[62] Lan, M.; Zhao, S.; Liu, W.; Lee, C.; Zhang, W.; Wang, P. *Adv. Healthcare Mater.* **2019**, *8*, 1900132.

[63] Shi, X.; Zhang, C. Y.; Gao, J.; Wang, Z. *WIREs Nanomed. Nanobiotechnol.* **2019**, *11*, 1560.

[64] Li, Z.; Li, S.; Guo, Y.; Yuan, C.; Yan, X.; Schanze, K. S. *ACS Nano* **2021**, *15*, 4979-4988.

[65] An, R.; Cheng, X.; Wei, S.; Hu, Y.; Sun, Y.; Huang, Z.; Chen, H.; Ye, D. *Angew. Chem.* **2020**, *132*, 20817-20825.

[66] Yan, P.; Liu, L.; Wang, P. *ACS Appl. Bio Mater.* **2020**, *3*, 3456-3475.

[67] Zhou, M.; Wang, M.; Dai, Z. *Mater. Chem. Front.* **2020**, *4*, 2223-2234.

[68] Um, W.; Pramod, K. E. K.; Lee, J.; Kim, C. H.; You, D. G.; Park, J. H. *Chem. Commun.* **2021**, *57*, 2854-2866.

[69] Liang, S.; Deng, X.; Ma, P.; Cheng, Z.; Lin, J. *Adv. Mater.* **2020**, *32*,

2003214.

[70] Sun, Y.; An, C.; Wu, L.; Zeng, W.; Wang, J.; Wang, Y.; He, J.; Gao, G.; Ye, D. *ACS Nano* **2021**, *15*, 16298-16313.

[71] Chen, Y.; Yin, B.; Liu, Z.; Wang, H.; Fu, Z.; Ji, X.; Tang, W.; Ni, D.; Peng, W. *Nano Res.* **2022**, early access.

[72] Zhang, L.; Li, C.; Wang, S.; Zhang, X. *Adv. Healthcare Mater.* **2022**, *11*, 2101971.

[73] Jia, C.; Guo, Y.; Wu, F. *Small* **2022**, 18, 2103868.

[74] Zhang, L.; Wan, S.; Li, C.; Xu, L.; Cheng, H.; Zhang, X. *Nano Lett.* **2018**, *18*, 7609-7618.

[75] Duesterberg, C. K.; Mylon, S. E.; Waite, T. D. *Environ. Sci. Technol.* **2008**, *42*, 8522-8527.

[76] Brillas, E.; Baños, M. A.; Camps, S.; Arias, C.; Cabot, P. L.; Garrido, J. A.; Rodríguez, R. M. *New J. Chem.* **2004**, *28*, 314-322.

[77] Ma, B.; Wang, S.; Liu, F.; Zhang, S.; Duan, J.; Li, Z.; Kong, Y.; Sang, Y.; Liu, H.; Bu, W.; Li, L. *J. Am. Chem. Soc.* **2019**, *141*, 849-857.

[78] Hao, Y.; Mao, L.; Zhang, R.; Liao, X.; Yuan, M.; Liao, W. *ACS Appl. Bio Mater.* **2021**, *4*, 7081-7093.

[79] Sun, H.; Zhang, Y.; Chen, S.; Wang, R.; Chen, Q.; Li, J.; Luo, Y.; Wang, X.; Chen, H. *ACS Appl. Mater. Interfaces* **2020**, *12*, 30145-30154.

Chapter 2: Fluorescent/Magnetic Nano-aggregation via Electrostatic Force between Modified Quantum Dot and Iron Oxide Nanoparticles for Bimodal Imaging of U87MG Tumor Cells

2.1 Introduction

Malignant tumors remain one of the most serious diseases in humans. Imaging technology has attracted much attention for early-stage cancer diagnoses, mainly comprising fluorescence imaging (FI) [1], positron emission tomography (PET) [2], ultrasound (US) imaging [3], photoacoustic (PA) imaging [4], computed tomography (CT) [5] and magnetic resonance imaging (MRI) [6] according to different imaging principles. However, despite the merits of each imaging modality, they all suffer from weaknesses, such as a low spatial resolution, low sensitivity, high cost or radiation risk. For instance, both FI and PET possess a high sensitivity despite their low spatial resolution. [7, 8] In contrast, deep tissue penetration can be realized via CT or MRI, but it's difficult to conduct quantitative analyses using the obtained images. [7, 8] Therefore, researchers have attempted to develop versatile nanoprobes for bi- or multi-modal imaging in order to acquire different aspects of information for accurate clinical diagnoses.

In recent decades, various fluorescent and magnetic nanomaterials have been developed and applied to tumor cell targeting due to their special characteristics, such as the small size effect, surface effect and quantum size effect. [9-11] However, producing ideal nanoprobes with a high fluorescence intensity, rapid magnetic signal, and specific recognition towards tumors remains challenging. Quantum dots (QDs), a type of colloidal semiconductor nanocrystal, are generally 2-10 nm in diameter. Owing to their special core/shell structure, QDs have attractive merits over traditional organic dyes, such as narrow emission spectra, tunable emission and good resistance against photobleaching, which plays a significant role in sensitive FI for cytologic diagnoses. [12-15] Nevertheless, FI has difficulty in providing information on tissue

penetration depth. MRI, which relies on paramagnetic and superparamagnetic metal (Mn, Fe, Gd) nanomaterials, can produce non-invasive, high-spatial-resolution images without radiation for tumor detection. [16-18] SPIO NPs, a kind of outstanding T_2-weighted MR contrast agent, are able to effectively decrease the transverse relaxation time (T_2) of water molecules and heighten the image contrast and sensitivity. [19] They have been widely developed due to their high contrast in comparison to T_1-weighted ones, low cytotoxicity and splendid biocompatibility. It therefore seems useful to bind QDs with SPIO NPs for fluorescence/MR dual-modal imaging to improve the diagnostic efficiency.

The modification of nanomaterials is basically achieved by covalent conjugation such as the classic coupling reaction between carboxyl and amine groups via EDC. However, covalent conjugation generally involves harsh reaction conditions and insufficient coupling efficiency. [20, 21] A facile and efficient method for assembling QDs and SPIO NPs for biological imaging is thus desired.

We herein report the generation of quantum-magnetic nanoparticles with tumor-targeting RGD (QMNP-RGD) for fluorescence/T_2-weighted MR bimodal imaging of tumor cells, which were produced by convenient electrostatic binding of RGD peptide-modified QDs and trimethylamine dextran-coated magnetic iron oxide nanoparticles (TMADM). Successful imaging of *in vitro* tumor cells indicates that this fluorescence and magnetic nanomaterial has great potential utility for cancer theranostics in biological and clinical applications.

2.2 Experimental section

2.2.1 Chemicals and reagents

Carboxyl QD655, 1-ethyl-3-(3-dimethylaminopropyl)carbodiimide hydrochloride (EDC) and Alexa Fluor™ 488 Phalloidin were purchased from Thermo Fisher Scientific (MA, USA). Cyclo(RGDfk) was acquired from Cayman Chemical (MI, USA). Hoechst 33342 solution were purchased from FUJIFILM Wako Pure Chemical Co. (Osaka, Japan). All other chemicals (analytical reagent grade) were acquired from qualified reagent suppliers.

2.2.2 Instruments and apparatuses

Dynamic light scattering (DLS) and zeta potential analyses were conducted on a Malvern Zetasizer ZEN3600 (Malvern Instruments Ltd., UK). An infinite 200 pro microplate reader (Tecan, Austria) was used for absorption measurements. Fluorescent images of cells were acquired by a BZ-X700 fluorescent microscope (Keyence, Japan), an A1RMP multiphoton confocal laser scanning microscope (Nikon, Japan) or an IVIS Spectrum CT system (PerkinElmer, USA). Flow cytometry assays were conducted on a BD LSRFortessa™ X-20 flow cytometer (BD Biosciences, USA). *In vitro* MR images were acquired on a 1.5 ± 0.1 T MR VivoLVA 1506 MRI system (Japan REDOX, Japan).

2.2.3 Synthesis of QD-RGD

QD-RGD was synthesized by peptide conjugation via EDC. In brief, 420 μL borate buffer (pH 7.4) was added to a 1.5-mL tube. 60 μL 8 μM QD655 and 0.15 mg cyclo(Arg-Gly-Asp-d-Phe-Lys) (cRGDfk) were then added, followed by the addition of 0.09 mg EDC solution. The mixture was stirred in the dark for 2 h at room temperature. Finally, QD-RGD was obtained by ultrafiltration (30 kDa, 4000 rpm; Pall corp., USA) via borate buffer (pH 8.4) and stored 4 °C in the dark before use.

2.2.4 Synthesis of TMADM

TMADM were obtained from Meito Sangyo Co. Ltd (Aichi, Japan), with a transverse relaxivity (r_2) calculated as approximately 151 mM^{-1} s^{-1} per Fe. [22, 23] In brief, TMADM was prepared by decorating magnetic iron oxide with polysaccharide (trimethylamine dextran). Polysaccharide was synthesized as follows: 100 g dextran was dissolved in 100 mL water, followed by the addition of sodium hydroxide and diethylaminoethyl chloride. The temperature was increased to 60 °C followed by stirring for 2-3 h. Hydrochloric acid was added to adjust the pH to 8.0. Methanol and acetone at 2.0-fold were added under continuous stirring. The precipitate was obtained, redispersed in 500 mL water, filtrated, concentrated under low pressure, and lyophilized. 15 g aforementioned product (polysaccharide) was then dissolved in 40 mL water under nitrogen atmosphere. 0.9 g ferrous chloride in 8.8 mL 1 M ferric

chloride solution was added under continuous stirring, and 1.5 M NaOH was used to adjust the pH to 11.0. The obtained solution was purified by ultrafiltration via borate buffer (pH 9.0). Acetone was then added to precipitate TMADM, which was purified through a membrane filter (0.2 μm).

2.2.5 Synthesis of QMNP-RGD

QMNP-RGD were prepared by adding positively charged TMADM (10 μg/mL for Fe, 0.5 mL) into excessive negatively charged QD-RGD (100 nM, 0.5 mL) with the help of ultrasound, kept for 30 min, and purified by precipitation to remove excessive QD-RGD. QMNP as the control material was similarly produced by substituting QDs with QD-RGD.

2.2.6 Cell culture

Human glioma U87MG cells were cultured in DMEM (Gibco) medium containing 10% (v/v%) fetal bovine serum (FBS) and 1% (v/v) penicillin/streptomycin (PS) in a cell incubator with 5% CO_2 at 37 °C. Phosphate-buffered saline (PBS; pH 7.2, 1×) and 0.25% (m/v%) trypsin with 0.1% (m/v%) EDTA 4Na were used to rinse and digest cells, respectively.

2.2.7 Cytotoxicity assay (CCK-8)

~1×10^4 U87MG cells were seeded in 96-well plates and allowed to grow overnight. QMNP-RGD with different concentrations in DMEM (2% FBS, 1% PS) at a total volume of 0.1 mL were added. After incubation for 4, 9 and 24 h, the solution was thrown away, and rinsed carefully. 0.1 mL DMEM and 10 μl Cell-Counting-Kit-8 (CCK-8) solution were added for another 1 h incubation. The absorbances of samples (A_{sample}) at 450 nm were acquired on a microplate reader, while those of cell samples without any treatment were used as the control ($A_{control}$). The cell viability was evaluated by the formula $(A_{sample}-A_{blank})/(A_{control}-A_{blank}) \times 100\%$ (A_{blank} is the absorbance of 0.1 mL DMEM medium and 10 μL CCK-8 solution without cells) at 450 nm.

2.2.8 *In vitro* fluorescence imaging of cells

To acquire the time-dependent fluorescence images, ~3×10^4 U87MG cells were

seeded in 24-well plates and allowed to grow overnight. QMNP-RGD (1 μg/mL for Fe) in DMEM (2% FBS, 1% PS) at a total volume of 0.5 mL were added and incubated in the cell incubator for 1, 2, 3, 4 and 6 h.

To prove the$\alpha_v\beta_3$ integrin-mediated active delivery, ~ 3×10^4 U87MG cells were seeded in 24-well plates and allowed to grow overnight. QD (2 nM), QD-RGD (2 nM), QMNP (1 μg/mL for Fe), QMNP-RGD (1 μg/mL for Fe) or QMNP-RGD + RGD (1 μg/mL for Fe, pretreated by 10 μM cRGDfk for 1 h to block $\alpha_v\beta_3$ integrin) in DMEM (2% FBS, 1% PS) at a total volume of 0.5 mL was added and incubated in the cell incubator for 2 h.

After that, the solution was thrown away, and the cells were rinsed with PBS twice. Finally, fluorescence images were acquired on a fluorescent microscope through a Texas red (TxRed) filter (Ex: 560 ± 20 nm, Em: 630 ± 32 nm).

2.2.9 Internalization analysis

~1×10^5 U87MG cells were seeded in a 35-mm glass-bottom dish and allowed to grow overnight. QMNP-RGD (1 μg/mL for Fe) in DMEM (2% FBS, 1% PS) at a total volume of 1.5 mL were added and incubated in the cell incubator for 2 h. After that, the solution was thrown away, and the cells were rinsed with PBS twice, followed by fixing with 4% polyfluoroalkoxy (PFA). A 1.5-mL PBS solution with Alexa Fluor™ 488 Phalloidin (300 nM) and Hoechst 33342 (0.1 μg/mL) was used for staining for 30 min, followed by rinsing of the cells twice. Fluorescence images were obtained on a confocal laser scanning microscope through the DAPI channel (Ex: 402.5 nm, Em: 450 ± 25 nm) for Hoechst 33342, the Alexa 488 antibody channel (Ex: 487.8 nm, Em: 525 ± 25 nm) for Alexa Fluor™ 488 Phalloidin and the QD655 channel (Ex: 600 nm, Em: 700 ± 37 nm) for QMNP-RGD.

2.2.10 Flow cytometric analysis

~2×10^5 U87MG cells were seeded in 6-well plates and allowed to grow overnight. QDs (2 nM), QD-RGD (2 nM), QMNP (1 μg/mL for Fe), QMNP-RGD (1 μg/mL for Fe) or QMNP-RGD + RGD (1 μg/mL for Fe, pretreated by 10 μM cRGDfk for 1 h to block $\alpha_v\beta_3$ integrin) in DMEM (2% FBS, 1% PS) in a total volume of 2 mL was

added to each well and incubated in the cell incubator for 2 h. Untreated cells were used as a control group (blank). The solution was subsequently thrown away, and the cells were rinsed with PBS twice. To detach the cells, 0.8 mL trypsin was added and left for 2 min in the cell incubator, followed by the addition of 0.5 mL culture medium to stop digestion. The cells were transferred into 1.5-mL tubes and collected after centrifugation (1500 rpm) for 5 min. The cells were then rinsed with 1 mL PBS, centrifuged (1500 rpm) for 5 min again, dispersed in 0.5 mL FACS buffer (PBS with 1% BSA and 0.1% NaN_3) and filtered via 70-μm cell strainers. For each sample, 1×10^4 live cells were used for flow cytometric analyses through the PerCP-Cy5.5 channel (Ex: 488 nm, Em: 695 ± 20 nm) with detailed parameters as follows: FSC, 50; SSC, 220; PerCP-Cy5.5, 400.

2.2.11 Bimodal imaging of cell pellets

For FI, ~5×10^5 U87MG cells were seeded in 6-cm cell culture dishes and allowed to grow overnight. QDs (2 nM), QD-RGD (2 nM), QMNP (1 μg/mL for Fe), QMNP-RGD (1 μg/mL for Fe) or QMNP-RGD + RGD (1 μg/mL for Fe, pretreated by 10 μM cRGDfk for 1 h to block $\alpha_v\beta_3$ integrin) in DMEM (2% FBS, 1% PS) at a total volume of 3 mL was added and incubated in the cell incubator for 2 h. The solution was then thrown away, and the cells were rinsed with PBS twice. 1 mL trypsinwas added to detach the cells and held for 2 min in the cell incubator, followed by the addition of 0.5 mL culture medium to stop digestion. The cells were then transferred into 1.5-mL tubes and centrifuged (1200 rpm) for 4 min. Fluorescence imaging was performed using IVIS equipment (Ex: 605 nm, Em: 660 nm).

For *in vitro* MRI, ~2×10^6 U87MG cells were seeded in 10-cm cell culture dishes. TMADM (1 μg/mL for Fe), QMNP (1 μg/mL for Fe), QMNP-RGD (1 μg/mL for Fe) or QMNP-RGD + RGD (1 μg/mL for Fe, pretreated by 10 μM cRGDfk for 1 h to block $\alpha_v\beta_3$ integrin) in DMEM (2% FBS, 1% PS) at a total volume of 5 mL was added to each well and incubated in the cell incubator for 2 h. Untreated cells were used as a control group (blank). Subsequently, the cells were rinsed, trypsinized, transferred into 0.2-mL tubes and centrifuged (1200 rpm, 4 min). MR images were acquired on a

1.5 T MRI machine with parameters as follows: T_2-weighted sequence, spin echo; TR/TE, 3000/69 ms; image size, 128 × 256; slice thickness, 1 mm; slice number, 18; interval, 0.5 mm; field of view (FOV), 80 mm × 40 mm. The acquisition time of each scan was 04 min 05 s. Acquired MR images were transferred to the ImageJ software program for a quantitative analysis.

2.3 Results and discussion

The electrostatic assembly of QMNP-RGD is illustrated in Figure 2-1, including the preparation of TMADM and modification of QDs with RGD peptide. First, commercial QDs were selected as the fluorophore due to their high fluorescence intensity and remarkable stability. Since being verified as a type of tumor-targeting ligand for active recognition towards $\alpha_v\beta_3$ integrin, which is overexpressed on the membrane of many kinds of tumor cells, [24, 25] RGD peptide has been used to decorate QDs (denoted as QD-RGD) to promote delivery into tumors. As QDs are stabilized by negatively charged carboxylic groups, it is necessary to create a positively charged magnetic nanomaterial for electrostatic binding with QD-RGD. We therefore introduced a cationic polysaccharide to encapsulate SPIO NPs to form fluorescent and magnetic nanoprobes (QMNP-RGD) based on the electrostatic force.

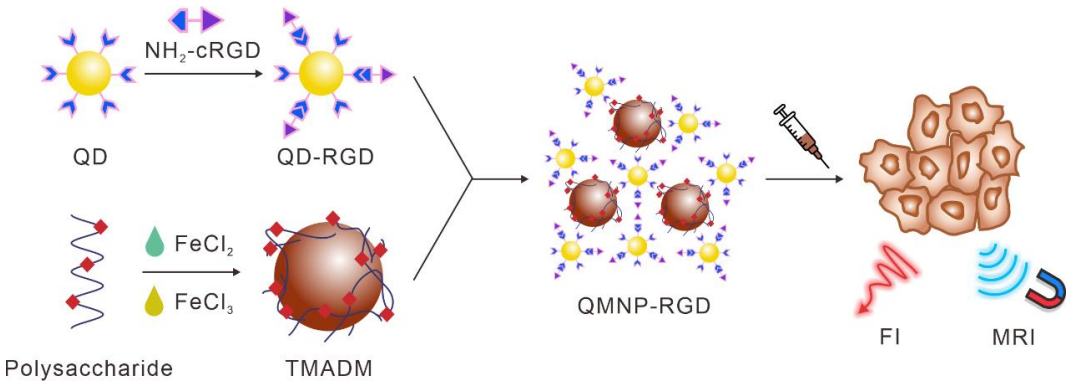

Figure 2-1. Schematic illustration of the design of QMNP-RGD for fluorescence/MR bimodal imaging of *in vitro* U87MG tumor cells.

We first examined the integration of QMNP-RGD by the size and zeta potential detection (Figure 2-2). DLS analysis showed that the hydrodynamic diameter and zeta voltage of QDs were 15 nm and -42 mV. After modification with the RGD peptide, the size increased to ~21 nm. Correspondingly, a weakly negative zeta voltage (-26

mV) of QD-RGD was noted, since negatively charged carboxyl groups from QDs were partially taken up by the RGD peptides. TMADM conversely showed a larger size (53 nm) and a positive zeta voltage (+7.2 mV), which enabled integration with negatively charged QD-RGD via electrostatic force. When TMADM were mixed with QD-RGD, QMNP-RGD were formed, showing an average diameter of 208 nm due to slight aggregation. The zeta voltage of QMNP-RGD (-25 mV) remained negative, as with QD-RGD, probably because QD-RGD was outmost for the nano-aggregation.

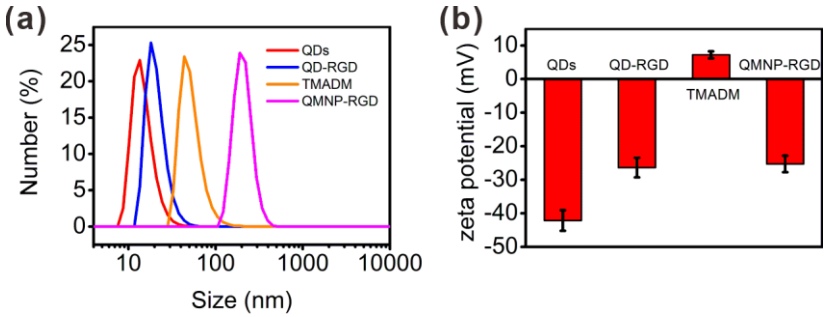

Figure 2-2 (a) DLS analysis results and (b) zeta potentials of QDs, QD-RGD, TMADM and QMNP-RGD.

Encouraged by the successful preparation, we first evaluated the cytotoxicity of QMNP-RGD towards $\alpha_v\beta_3$ integrin-positive U87MG tumor cells by a CCK-8 assay before applying it to bimodal imaging. Tumor cells were incubated with different concentrations of QMNP-RGD for 4, 9 or 24 h at 37 °C. As shown in Figure 2-3, QMNP-RGD had almost no effect on cell viability towards U87MG tumor cells, even at concentrations of up to 5 μg/mL for Fe, suggesting that QMNP-RGD would be useful as a biocompatible nanoprobe for tumor cell studies.

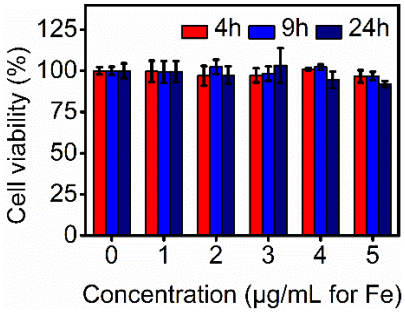

Figure 2-3. U87MG cell viabilities after incubation with different concentrations of QMNP-RGD for 4, 9, 24 h.

The utility for fluorescence imaging of *in vitro* U87MG tumor cells was next

investigated. After incubation with QMNP-RGD for different durations, the fluorescence inside U87MG cells was bright on fluorescent microscopy (Figure 2-4), demonstrating the successful uptake of QMNP-RGD by U87MG cells. To further confirm the effective uptake, Alexa Fluor™ 488 Phalloidin and Hoechst 33342 were used to co-stain tumor cell microfilaments and nuclei, respectively, after incubation with QMNP-RGD. Strong red fluorescence as well as blue and green fluorescence were observed at the same depth via a confocal laser scanning microscope, indicating that QMNP-RGD did indeed enter tumor cells (Figure 2-5).

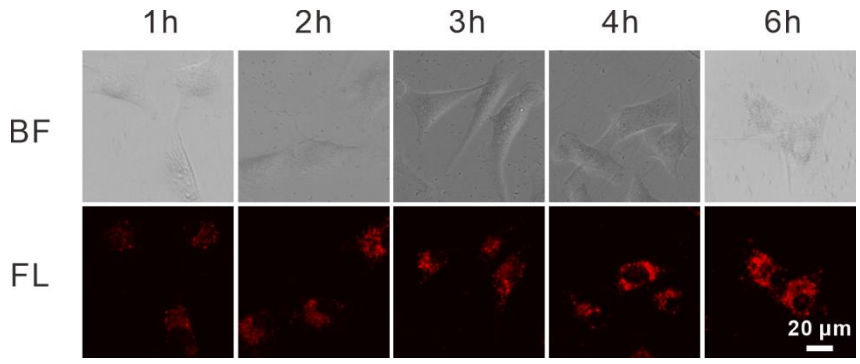

Figure 2-4. Fluorescence images of *in vitro* U87MG cells after incubation with QMNP-RGD (1 μg/mL for Fe) for 1, 2, 3, 4 and 6 h (Ex: 560 ± 20 nm, Em: 630 ± 32 nm).

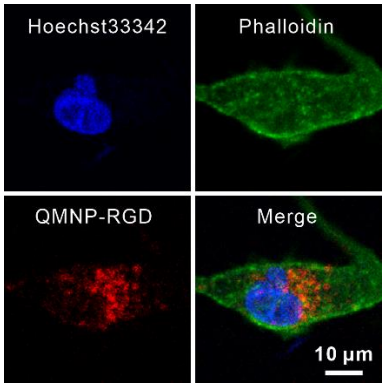

Figure 2-5. Fluorescence images of *in vitro* U87MG cells after incubation with QMNP-RGD (1 μg/mL for Fe) for 2 h, followed by staining with Alexa Fluor™ 488 Phalloidin (300 nM) and Hoechst 33342 (0.1 μg/mL) for 30 min.

We then investigated the RGD-mediated active transport towards individual U87MG cell reflected by fluorescence imaging (Figure 2-6). After incubation for the same duration (2 h), U87MG cells incubated with QDs (Group I) did not exhibit any

red fluorescence, whereas apparent fluorescence was noted in U87MG cells incubated with QD-RGD (Group II), suggesting the successful decoration of RGD peptide on QDs. Similarly, the fluorescence in U87MG cells incubated with QMNP-RGD (Group III) was stronger than that in cells incubated with RGD-free QMNP (Group IV). This bright fluorescence in tumor cells was able to be effectively reduced by pretreatment with free cRGDfk due to a lack of RGD-mediated active recognition. RGD was thus concluded to play a significant role in active recognition and the increased U87MG cellular uptake of the nanomaterial.

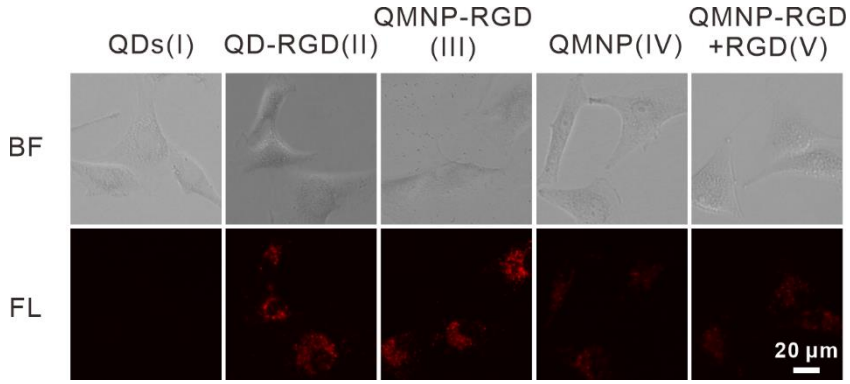

Figure 2-6. Fluorescence images of *in vitro* U87MG cells incubated with (I) QDs (2 nM), (II) QD-RGD (2 nM), (III) QMNP-RGD (1 μg/mL for Fe), (IV) QMNP (1 μg/mL for Fe) or (V) QMNP-RGD + RGD (1 μg/mL for Fe, pretreated by 10 μM cRGDfk for 1 h) for 2 h (Ex: 560 ± 20 nm, Em: 630 ± 32 nm).

The overall fluorescence intensity in cells and uptake efficiency were monitored by flow cytometry, with U87MG cells incubated with different nanomaterials for 2 h (Figure 2-7). Generally, U87MG cells incubated with QD-RGD or QMNP-RGD exhibited strong fluorescence compared with other groups. The fluorescence intensity threshold was set at approximately 500 a.u. based on the intrinsic fluorescence intensity of blank cells, and the uptake efficiency was then calculated based on this threshold value. As depicted in Fig. 2-7b, the delivery ratio for U87MG cells incubated with QDs was only 15% after 2 h incubation but was increased to 81% using QD-RGD. A high delivery ratio (93%) was obtained for tumor cells incubated with QMNP-RGD, which was higher than that following incubation with QMNP (18.7%) or pretreatment with RGD (27%), indicating that the RGD peptide facilitated

the U87MG cellular uptake of nanomaterial.

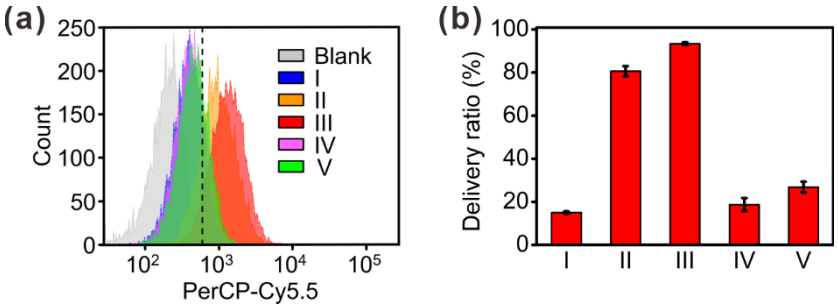

Figure 2-7. (a) Results of a flow cytometric analysis of fluorescence intensity in U87MG cells after incubation with (I) QDs (2 nM), (II) QD-RGD (2 nM), (III) QMNP-RGD (1 μg/mL for Fe), (IV) QMNP (1 μg/mL for Fe) or (V) QMNP-RGD + RGD (1 μg/mL for Fe, pretreated by 10 μM cRGDfk for 1 h) for 2 h (Ex: 488 nm, Em: 695 ± 20 nm). (b) Statistics of delivery ratios in (a).

Inspired by such a high delivery ratio with QMNP-RGD due to RGD-mediated active recognition, we next evaluated its effect on *in vitro* fluorescence/MR bimodal imaging of U87MG cell pellets (Figure 2-8). The fluorescence from QD-RGD-treated cell pellets was markedly brighter than that from QD-treated ones (be almost four-fold). Similarly, QMNP-RGD-treated cell pellets also showed strong fluorescence relative to QMNP- and RGD + QMNP-RGD-treated ones, which was consistent with the results above. Along with the assessment of the intracellular fluorescence, T_2-weighted MRI of cell pellets was conducted as well. After incubation with QMNP-RGD, the T_2-weighted MR brightness was decreased to 38 a.u. against that from blank cell pellets (144 a.u.), which was far lower than that from QMNP-treated ones (143 a.u.) or RGD + QMNP-RGD-treated ones (128 a.u.). Worth mentioning is that QD-free TMADM-incubated cell pellets also showed a low brightness (8.7 a.u.), as positively charged particles are beneficial for the intracellular incorporation based on their attraction to the negatively charged cell surface. These findings demonstrated that $\alpha_v\beta_3$ integrin on the U87MG cell membrane played an important role in the active transport and subsequent uptake of QMNP-RGD, resulting in high intracellular fluorescence intensity and MR contrast for *in vitro* bimodal imaging of tumor cells.

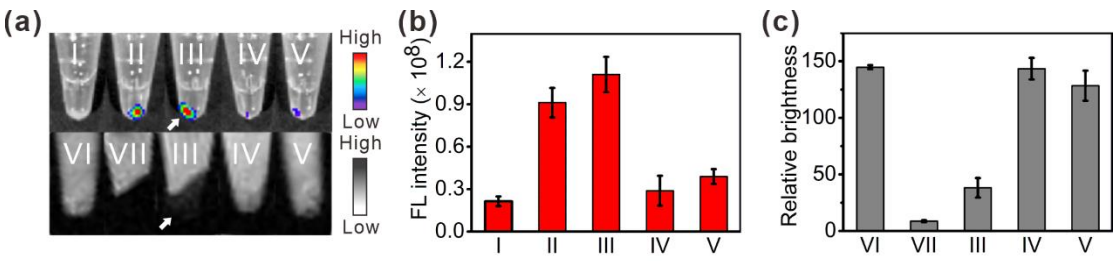

Figure 2-8. (a) Fluorescence (up) (Ex/Em = 605/660 nm) and T_2-weighted MR (down) (TR/TE = 3000/69 ms at 1.5 T) images of U87MG cell pellets after incubation with (I) QDs (2 nM), (II) QD-RGD (2 nM), (III) QMNP-RGD (1 μg/mL for Fe), (IV) QMNP (1 μg/mL for Fe), (V) QMNP-RGD + RGD (1 μg/mL for Fe, pretreated by 10 μM cRGDfk for 1 h), (VI) untreated or (V) TMADM (1 μg/mL for Fe) for 2 h. (b) Statistics of total FL intensities in (a) up. (c) Relative brightness of cell pellets in (a) down. White arrows indicate obvious signal changes in group (III).

2.4 Conclusion

In summary, a tumor-targeted nanoprobe (QMNP-RGD) was developed by a facile method of electrostatic binding of RGD-modified negatively charged QDs and positively charged SPIO NPs, and we verified that this kind of probe was able to be efficiently and rapidly taken up by tumor cells. They were also shown to be useful for fluorescence/MR bimodal imaging of *in vitro* tumor cells. QMNP-RGD exhibited excellent biocompatibility by the integration method of electrostatic binding, which is promising for the development of advanced nanomaterials with diverse features to meet different requirements in biological and clinical imaging.

2.5 References

[1] Yang, Y.; Fan, X.; Li, L.; Yang, Y.; Nuernisha, A.; Xue, D.; He, C.; Qian, J.; Hu, Q.; Chen, H.; Liu, J.; Huang, W. *ACS Nano* **2020**, *14*, 2509-2521.

[2] Lv, G.; Qiu, L.; Sun, Y.; Li, K.; Liu, Q.; Zhao, Q.; Qin, S.; Lin, J. *J. Nucl. Med.* **2020**, *61*, 117-122.

[3] Ho, Y.; Wu, C.; Jin, Q.; Lin, C.; Chiang, P.; Wu, N.; Fan, C.; Yang, C.; Yeh, C. *Biomaterials* **2020**, *232*, 119723.

[4] Zhou, Z.; Li, B.; Shen, C.; Wu, D.; Fan, H.; Zhao, J.; Li, H.; Zeng, Z.; Luo,

Z.; Ma, L.; Tan, C. *Small* **2020**, *16*, 2004173.

[5] Jungmann, G.; Kaissis, G. A.; Ziegelmayer, S.; Harder, F.; Schilling, C.; Yen, H.; Steiger, K.; Weichert, W.; Schirren, R.; Demir, I. E.; Friess, H.; Makowski, M. R.; Braren, R. F.; Lohöfer, F. K. *Cancers* **2021**, *13*, 2069.

[6] Yin, Z.; Ji, Q.; Wu, D.; Li, Z.; Fan, M.; Zhang, H.; Zhao, X.; Wu, A.; Cheng, L.; Zeng, L. *ACS Appl. Mater. Interfaces* **2021**, *13*, 14928-14937.

[7] Wu, M.; Shu, J. *Contrast Media Mol. I.*, **2018**, 1382183.

[8] Park, Y. I.; Lee, K. T.; Suh, Y. D.; Hyeon, T. *Chem. Soc. Rev.* **2015**, *44*, 1302.

[9] Shi, H.; Sun, Y.; Yan, R.; Liu, S.; Zhu, L.; Liu, S.; Feng, Y.; Wang, P.; He, J.; Zhou, Z.; Ye, D. *Nano Lett.* **2019**, *19*, 937-947.

[10] Zhang, Y.; Ma, Q.; Yan, Y.; Guo, C.; Xu, S.; Wang, L. *Anal. Chem.* **2020**, *92*, 15679-15684.

[11] Luo, Z.; Hu, D.; Gao, D.; Yi, Z.; Zheng, H.; Sheng, Z.; Liu, X. *Adv. Mater.* **2021**, *33*, 2102950.

[12] Yukawa H.; Baba, Y. *Anal. Chem.* **2017**, *89*, 2671-2681.

[13] Yukawa, H.; Watanabe, M.; Kaji, N.; Okamoto, Y.; Tokeshi, M.; Miyamoto, Y.; Noguchi, H.; Baba, Y.; Hayashi, S. *Biomaterials* **2012**, *33*, 2177-2186.

[14] Liu, Y.; Liao, M.; He, X.; Liu, X.; Kou, X.; Xiao, D. *Anal. Sci.* **2015**, *31*, 971-977.

[15] Yukawa H.; Baba, Y. *Anal. Sci.* **2018**, *34*, 525-532.

[16] Sun, H.; Zhang, Y.; Chen, S.; Wang, R.; Chen, Q.; Li, J.; Luo, Y.; Wang, X.; Chen, H. *ACS Appl. Mater. Interfaces* **2020**, *12*, 30145-30154.

[17] Jin, Q.; Liu, J.; Zhu, W.; Dong, Z.; Liu, Z.; Cheng, L. *ACS Appl. Mater. Interfaces* **2018**, *10*, 332-340.

[18] Sun, S.; Dong, L.; Cao, Y.; Sun, H.; Yan, X. *Anal. Chem.* **2013**, *85*, 8436-8441.

[19] Yukawa, H.; Nakagawa, S.; Yoshizumi, Y.; Watanabe, M.; Saito, H.; Miyamoto, Y.; Noguchi, H.; Oishi, K.; Ono, K.; Sawada, M.; Kato, I.; Onoshima, D.;

Obayashi, M.; Hayashi, Y.; Kaji, N.; Ishikawa, T.; Hayashi, S.; Baba, Y. *Plos One* **2014**, *9*, 110142.

[20] Zhang, Y.; Park, K.; Suazo, K. F.; Distefano, M. D. *Chem. Soc. Rev.* **2018**, *47*, 9106-9136.

[21] Lee J. M.; Cooper, A. I.; *Chem. Rev.* **2020**, *120*, 2171-2214.

[22] Ogihara, Y.; Yukawa, H.; Onoshima, D.; Baba, Y. *Anal. Sci.* **2017**, *33*, 143-146.

[23] Oishi, K.; Miyamoto, Y.; Saito, H.; Murase, K.; Ono, K.; Sawada, M.; Watanabe, M.; Noguchi, Y.; Fujiwara, T.; Hayashi, S.; Noguchi, H. *Plos One* **2013**, *8*, 57046.

[24] Danhier, F.; Breton, A. L.; Préat, V. *Mol. Pharmaceutics* **2012**, *9*, 2961-2973.

[25] Temming, K.; Schiffelers, R. M.; Molema, G.; Kok, R. J. *Drug Resist. Update.* **2005**, *8*, 381-402.

Chapter 3: Multifunctional Magnetic CuS/Gd_2O_3 Nanoparticles for Fluorescence/MR Bimodal Imaging-guided Photothermal-intensified Chemodynamic Synergetic Therapy of Targeted Tumors

3.1 Introduction

Worldwide, cancer has become a dominant cause of mortality. The induced generation of cytotoxic ROS, such as superoxide ($\cdot O_2^-$), singlet oxygen ($^1O_2$) or hydroxyl (·OH), which are capable of killing cancer cells by causing oxidative damage to intracellular biomolecules, has been exploited as a burgeoning cancer treatment strategy. [1-4] Photodynamic therapy (PDT), a type of light-triggered therapy, can convert oxygen into ROS, which is minimally invasive and highly selective, with low side effects compared with conventional therapies. [5] However, PDT suffers from limited penetration depth and the ROS generation efficiency in the TME is low. [6-9] Different from PDT, CDT is a continuous chemical process that converts H_2O_2 in the TME into toxic ·OH, which has also been validated as an effective tool for cancer treatment. [10-12]

Nowadays, CDT is generally based on Fenton or Fenton-like reactions, in which various nanomaterials are utilized as a catalyst to accelerate the disproportionation of H_2O_2 into oxidative ·OH. Fe^{2+}-based nanomaterials have been applied to tumor treatment, but they are not efficient enough in the weakly acidic TME (pH 6.5-6.9) because strong acidity (pH 2-4), which is required for the classic Fe^{2+}-guided Fenton reaction, is physiologically inaccessible. [13] Besides, the amount of ROS produced is largely limited by the low reaction rate (55 M^{-1} s^{-1}) even in an ideal pH condition. [13] In order to make the most of CDT that is appropriate for the weakly acidic TME, researchers have focused their attention on the development of other transition metal (Mn, Cu)-based nanomaterials for Fenton-like reactions. [11, 12] Among these promising candidates, cuprous ion (Cu^+) is an alternative due to the much higher reaction rate ($\sim 1 \times 10^4$ M^{-1} s^{-1}) and the feasibility of its application in weakly acidic

and neutral media. [14] Nevertheless, the presence of sufficient endogenous biothiols (e.g., ~10 mM glutathione [GSH]) in cancer cells, which can scavenge the produced ·OH, restricts the efficiency of CDT. One strategy is to convert ample GSH into glutathione disulfide (GSSG) by cupric ion (Cu^{2+}) via a redox reaction. [15-17] It is therefore essential to develop novel Cu^{2+}-based nanomaterials as a practicable and efficient CDT agent.

Copper chalcogenides are emerging as potential inorganic nanomaterials for this purpose. In particular, CuS NPs, a kind of p-type semiconductor photosensitizer, possess strong and broad NIR absorbance, high PCE, excellent photostability, and low toxicity. [18-22] These endow CuS NPs with a PTT effect, which allows the thermal ablation of tumors by generating localized heat under NIR laser irradiation. This is noninvasive, provides deep penetration, and reduces the damage to normal tissues. [23-26] Moreover, recent research on CuS nanomaterials has demonstrated that the hyperthermia caused by laser irradiation can promote Fenton-like reactions and accelerate the release of ROS, contributing to enhanced CDT of tumor. [27, 28] This enables nanomaterial-mediated synergetic PTT and CDT for high-efficiency cancer treatment.

Basically, the preparation of CuS NPs was achieved in organic or aqueous phases. Organic syntheses are involved in high-temperature, toxic solvent, deoxygenated conditions, and the tedious phase transfer process before biological application. [20-22] It is preferable to propose a facile and moderate method for preparing CuS NPs for CDT-assisted PTT. In this study, we report the simultaneous production of versatile magnetic gadolinium oxide (Gd_2O_3) and CuS NPs through a simple one-pot synthesis method at room temperature and further decorate them into a fluorescent and tumor-targeting nanoprobe (BCGCR), which integrates NIR fluorescence/T_1-weighted MR bimodal imaging and NIR light-triggered PTT and enhanced CDT of tumors. Successful imaging and treatment of tumors in living mice suggest that this multifunctional nanomaterial has great prospects for application in progressive cancer theranostics in biomedical studies.

3.2 Experimental methods

3.2.1 Chemicals and reagents

Copper (II) chloride dihydrate ($CuCl_2 \cdot 2H_2O$), gadolinium (III) chloride hexahydrate ($GdCl_3 \cdot 6H_2O$), sodium hydroxide (NaOH), bovine serum albumin (BSA), sodium sulfide pentahydrate ($Na_2S \cdot 5H_2O$), methylene blue (MB) and Hoechst 33342 solution were purchased from FUJIFILM Wako Pure Chemical Co. (Osaka, Japan). Sulfo-NHS-Cy5.5 ester was obtained from Abcam (Cambridge, UK). Cyclo(RGDfk) and 2,7-dichlorodihydrofluorescein diacetate (DCFH-DA) were obtained from Cayman Chemical (Michigan, USA). Sulfo-NHS-acetate was purchased from BroadPharm California (USA). 1-ethyl-3-(3-dimethylaminopropyl)carbodiimide hydrochloride (EDC), N-hydroxysulfosuccinimide (sulfo-NHS), Alexa Fluor™ 488 Phalloidin, Lyso-Tracker Green DND-26, Calcein AM and propidium iodide (PI) were obtained from Thermo Fisher Scientific (Massachusetts, USA). All other chemicals of analytical reagent grade were obtained from qualified reagent supplies.

3.2.2 Instruments and apparatuses

XPS were recorded on an ESCALAB250 system with Al Kα as an X-ray resource (Thermo Scientific, America). EDS line scanning results were obtained using a SU-1500 scanning electron microscope (Hitachi, Japan) with an EMAX X-ray spectrometer (Horiba, Japan). X-ray powder diffraction (XRD) patterns were obtained on a SmartLab X-ray diffractometer (Rigaku, Japan). TEM images were obtained by a H-7650 transmission electron microscope (Hitachi, Japan) with an accelerating voltage of 100 kV. DLS and the zeta potential analysis were performed using a Malvern Zetasizer ZEN3600 (Malvern Instruments Ltd., UK). Cu^{2+} and Gd^{3+} concentrations were measured using a SPS7800 inductively coupled plasma atomic emission spectrometer (ICP-AES) (Seiko Instruments Inc., Japan). An infinite 200 pro microplate reader (Tecan, Austria) was used for UV-vis-NIR absorption spectra and fluorescence spectra scanning. Fluorescent images of cells were acquired using a BZ-X700 all-in-one fluorescent microscope (Keyence, Japan) or an A1RMP multiphoton confocal laser scanning microscope (Nikon, Japan). Flow cytometry

assays were conducted using a BD LSRFortessa™ X-20 flow cytometer (BD Biosciences, America). *In vitro/vivo* MR imaging was acquired using a 1.5 ± 0.1 T MR VivoLVA 1506 MRI system (Japan REDOX, Japan). Whole-body fluorescence images were acquired using an IVIS Spectrum CT system (PerkinElmer, America). A 980 nm NIR laser (Shanghai Dream Lasers Technology Co., Ltd., China) was used to evaluate the photothermal effect and for *in vitro/vivo* PTT/CDT experiments. Thermal images with real-time temperature were recorded using an FLIR C2 IR thermal camera (FLIR Systems, Inc., America).

3.2.3 Synthesis of BSA stabilized CuS/Gd_2O_3 (BCG)

BCG was produced by biomineralization according to previously reported methods, with modification. [29, 30] Briefly, 200 mg BSA was dispersed in 7 mL H_2O by ultrasound, followed by the addition of 1 mL 40 mM $CuCl_2 \cdot 2H_2O$ and 1 mL 20 mM $GdCl_3 \cdot 6H_2O$ under continuous stirring. After 2 min, 0.4 mL 1 M NaOH was used to adjust the pH of the mixture to ~12, and 0.16 mL 1 M $Na_2S \cdot 5H_2O$ was subsequently added. The colloid mixture was further stirred in the dark for another 5 h at room temperature, followed by dialysis (MWCO = 10 K) for 24 h via ultrapure water to remove unreacted ions. Finally, the deep brown mixture was stored at 4°C in the dark for further modification.

3.2.4 Modification of BCG with Cy5.5 and RGD

For modification of Cy5.5 with BCG, 0.1 mL PBS (pH 7.2, 10×) and 0.5 mg sulfo-NHS-Cy5.5 was added to 0.9 mL BCG containing 10 mg BSA and the mixture was stirred in dark conditions overnight. 10 mg sulfo-NHS-acetate was added and stirred for another 2 h to block residual -NH_2 groups of BSA. The unreacted sulfo-NHS-Cy5.5 and sulfo-NHS-acetate were removed by ultrafiltration (30 kDa, 3000 g, Millipore) via PBS (pH 7.2, 1×), and Cy5.5 conjugated BCG was obtained (denoted as BCGC). In order to further conjugate tumor targeting peptide (RGD), 2 mg EDC was added to the prepared mixture and stirred for 15 min. Subsequently, 2 mg sulfo-NHS was added and allowed for another 1 h reaction to activate carboxyl groups, followed by addition of 0.9 mg cRGDfk. The reaction was allowed overnight

and the mixture was purified by ultrafiltration (30 kDa, 3000 g) via PBS (pH 7.2, 1×). The obtained BCGCR NPs were resuspended in PBS and stored at 4°C in the dark for application. The concentrations of Gd and Cu in the prepared mixture was determined by ICP-AES.

3.2.5 Photothermal effect evaluation

BCGCR (0, 0.125, 0.25, 0.5 and 1 mM Cu^{2+}, respectively) in 0.3 mL PBS was added to a 48-well plate, followed by irradiation with a 980 nm laser at a power density of 0.8 W/cm^2 for 5 min. BCGCR (0.5 mM Cu^{2+}) in 0.3 mL PBS was irradiated with various power densities (0, 0.2, 0.5, 0.8 and 1.0 W/cm^2) for 5 min. For temperature quantification, thermal images were recorded every 1 min using an IR thermal camera.

To evaluate the photothermal conversion efficiency, BCGCR (1 mM Cu^{2+}) in 0.3 mL PBS was added into a 48-well plate, followed by irradiation with a 980 nm laser at a power density 0.8 W/cm^2 for 7 min. Thermal images with temperature quantification were recorded every 1 min using an IR thermal camera, which captured the whole processes of both the temperature increase and subsequent natural cooling.

3.2.6 Measurement of ·OH Generation

10 mg/mL BCG was mixed with 1 mM GSH solution for 30 min to obtain the intermediate product BCG-GSH. The obtained BCG-GSH (0.5 mM Cu^{2+}) was mixed with 10 μg/mL MB and 20 mM H_2O_2 at different pH values (5.4, 6.4 or 7.4) at different temperatures. To investigate enhanced ·OH generation under irradiation, BCG-GSH (0.5 mM Cu^{2+}) was mixed with 10 μg/mL MB and 20 mM H_2O_2 at pH 5.4, followed by laser irradiation (0.8 W/cm^2) for 5 min. Besides, BCG, BCG + GSH (1 mM), BCG + H_2O_2, BCG + GSH + H_2O_2 at the same concentration respectively was mixed with 10 μg/mL MB for 5 min as a control group. The ·OH generation was evaluated according to MB degradation, which was measured via the absorbance decrease on a microplate reader.

3.2.7 Cell culture

Human glioma U87MG cells and human embryonic kidney HEK293T cells were

cultured in DMEM (Gibco) medium with 10% fetal bovine serum (FBS) (v/v%) and 1% penicillin/streptomycin (PS) (v/v%) in the cell incubator with 5% CO_2 at 37°C. PBS (pH 7.2, 1×) and 0.25% (m/v%) trypsin with 0.1% (m/v%) EDTA 4Na were used for cell rinse and digest respectively.

3.2.8 FI of cells

To obtain time-dependent fluorescence images, U87MG cells (~2 × 10^4) were seeded in a 48-well plate and allowed to grow for 24 h. BCGCR (100 μg/mL) in 0.25 mL DMEM medium was added to U87MG cells and incubated for 1, 2, 3, 4 and 6 h respectively. Then, the solution was removed and rinsed with PBS twice.

To verify $\alpha_v\beta_3$ integrin mediated active delivery, U87MG and HEK293T cells (~2 × 10^4) were seeded in a 48-well plate and allowed to grow for 24 h. BCGCR (100 μg/mL) in 0.25 mL DMEM medium was added to U87MG and HEK293T cells. Besides, RGD-free BCGC (100 μg/mL) and RGD+BCGCR (100 μg/mL, pretreated with 10 μM cRGDfk for 1 h to block $\alpha_v\beta_3$ integrin) in 0.25 mL DMEM medium was added to U87MG cells. After incubation for 2 h, the solution was removed and rinsed with PBS twice.

Finally, fluorescence images were acquired using a fluorescent microscope through a Cy5.5 filter (Ex: 650 ± 22 nm, Em: 720 ± 30 nm).

3.2.9 Internalization analysis

U87MG cells (~1 × 10^5) were seeded in a 35-mm glass-bottom dish and allowed to grow for 24 h. BCGCR (50 μg/mL) in 1.0 mL DMEM medium was added and incubated for 2 h. After that, the solution was removed and rinsed by PBS once, followed by fixing with 4% polyfluoroalkoxy (PFA). These cells were then co-stained using 0.1 μg/mL Hoechst 33342 and 300 nM Alexa Fluor™ 488 Phalloidin for another 30 min, and rinsed with PBS twice.

To examine the intracellular location further, BCGCR-treated U87MG cells (mentioned above) were subsequently co-stained with 0.1 μg/mL Hoechst 33342 and 200 nM Lysotracker (LysoTracker™ Green) for 20 min. These cells were rinsed with PBS twice, and fresh DMEM medium was added.

Finally, fluorescence images were acquired using a confocal laser scanning microscope through the DAPI channel (Ex: 402.5 nm, Em: 450 ± 25 nm) for Hoechst 33342, Alexa 488 antibody channel (Ex: 487.8 nm, Em: 525 ± 25 nm) for Alexa Fluor™ 488 Phalloidin or LysoTracker™ Green and Cy5.5 channel (Ex: 639.8 nm, Em: 700 ± 37 nm) for BCGCR.

3.2.10 Flow cytometry

U87MG cells and HEK293T cells (~2 × 10^5) were seeded in 6-well plates and allowed to grow for 24 h. BCGCR (10 μg/mL) in 2 mL DMEM medium was added to U87MG and HEK293T cells. Besides, RGD free BCGC (10 μg/mL) and RGD+BCGCR (10 μg/mL, pretreated with 10 μM cRGDfk for 1 h to block $\alpha_v\beta_3$ integrin) in 2 mL DMEM medium was added to U87MG cells. After incubation for 2 h, the solution was removed and these cells were rinsed by PBS once. To detach these cells, 0.5 mL trypsin was added into each well and kept for 2 min, followed by addition of 0.5 mL culture medium to stop digestion. These cells were transferred into 1.5 mL tubes and collected by centrifugation (1500 rpm) for 5 min. After abandon of supernatants, dispersed by 1 mL PBS and centrifuged (1500 rpm) for 5 min again, these cells were resuspended by 0.5 mL FACS buffer (PBS with 1% BSA and 0.1% NaN_3) and filtered through 70 μm cell strainers. For each sample, 1 × 10^4 cells were analyzed on a flow cytometer through AlexaFluor700 channel (Ex: 633 nm, Em: 710 ± 25 nm) with detailed voltages as follows: for U87MG cell: FSC, 60; SSC, 220; AlexaFluor700, 450 and for HEK293T cell: FSC, 100; SSC, 250; AlexaFluor700, 450.

3.2.11 Bimodal imaging of cell pellets

For *in vitro* FI, U87MG cells and HEK293T cells (~1 × 10^6) were seeded in 10 cm cell culture dishes and allowed to grow for 24 h. BCGCR (10 μg/mL) in 5 mL DMEM medium was added to U87MG and HEK293T cells. Besides, RGD free BCGC (10 μg/mL) and RGD+BCGCR (10 μg/mL, pretreated with 10 μM cRGDfk for 1 h to block $\alpha_v\beta_3$ integrin) in 5 mL DMEM medium was added to U87MG cells. After incubation for 2 h, the solution was removed and these cells were rinsed by PBS

once. To detach these cells, 4 mL trypsin was added into each dish and kept for 2 min, then 4 mL culture medium to stop digestion. These cells were finally transferred into 1.5 mL tubes and centrifuged (1200 rpm, 4 min). Fluorescence images were obtained on an IVIS imaging system (Ex: 675 nm, Em: 720 nm). Fluorescence intensity was quantified by a region of interest (ROI) analysis using Living Image Software (4.5.2, PerkinElmer, MA, U.S.A).

For *in vitro* MRI, U87MG cells and HEK293T cells (~2×10^6) were seeded in 10 cm cell culture dishes and allowed to grow for 24 h. BCGCR (10 μM Gd^{3+}) in 5 mL DMEM medium was added to U87MG and HEK293T cells. Besides, RGD free BCGC (10 μM Gd^{3+}) and RGD+BCGCR (10 μM Gd^{3+}, pretreated with 10 μM cRGDfk for 1 h to block $\alpha_v\beta_3$ integrin) in 5 mL DMEM medium was added to U87MG cells. After incubation for 24 h and similar treatments mentioned above, these cells were transferred into 0.2 mL tubes and centrifuged (1200 rpm, 4 min) finally. MR images were obtained on a 1.5T MRI system using the following parameters: T_1-weighted sequence, spin echo; TR/TE, 500/9.0 ms; image size, 128 × 256; slice thickness, 1 mm; slice number, 18; interval, 0.5 mm; field of view (FOV), 60 mm × 30 mm. The acquisition time for each scanning was 01 min 05 s. Acquired MR images were transferred into ImageJ software for quantitative analysis. Percentage signal enhancement (%SE) was calculated as the % difference ratio between the signal intensities (SI) from respective samples and the one from blank samples: $\%SE = [(SI(s) - SI(b)]/SI(b) \times 100\%$

3.2.12 Quantitative analysis of the Gd uptake in cells

U87MG cells and HEK293T cells (~2×10^6) were seeded in 10 cm cell culture dishes and allowed to grow for 24 h. BCGCR (10 μM Gd^{3+}) in 5 mL DMEM medium was added to U87MG and HEK293T cells. Besides, RGD free BCGC (10 μM Gd^{3+}) and RGD+BCGCR (10 μM Gd^{3+}, pretreated with 10 μM cRGDfk for 1 h to block $\alpha_v\beta_3$ integrin) in 5 mL DMEM medium was added to U87MG cells. After incubation for 24 h, these cells were rinsed, trypsinized, counted and centrifuged. After digestion in 1 mL aqua regia assisted by ultrasound, and dilution with 4 mL H_2O, Gd^{3+}

concentrations were determined by ICP-AES; then the average uptake of Gd in each cell was calculated.

3.2.13 Evaluation of GSH consumption

U87MG cells (~2×10^5) were seeded in 6-well plates and allowed to grow for 24 h. RGD free BCGC (100 μg/mL) or BCGCR (100 μg/mL) in 2 mL DMEM medium was added to each well and incubated for 6 h. Untreated cells were used as control group (blank). After that, the solution was removed and rinsed carefully by PBS twice, and these cells were collected to measure the intracellular GSH via a GSH assay kit.

3.2.14 ROS generation analysis

U87MG cells (~2×10^4) were seeded in a 48-well plate and allowed to grow for 24 h. RGD free BCGC (100 μg/mL) or BCGCR (100 μg/mL) in 0.25 mL DMEM medium was added to each well and incubated for 6 h. Untreated cells were used as control group (blank). After that, the solution was removed and rinsed carefully by PBS once. 0.2 mL DMEM medium with DCFH-DA (10 μM) was used for another 30 min-incubation, then the cells were rinsed twice. Subsequently, 0.2 mL fresh DMEM medium was added and these cells were irradiated (or not) by a 980 nm laser (0.8 W/cm^2) for 5 min, followed by rinsing with PBS once. Finally, the level of ROS generation from cells was evaluated using a fluorescent microscope with a GFP filter (Ex: 470 ± 20 nm, Em: 525 ± 25 nm).

3.2.15 *In vitro* evaluation of cytotoxicity towards normal HEK293T cells (CCK-8)

HEK293T cells (~5×10^3) were seeded in 96-well plates and allowed to grow for 24 h. BCGCR (0, 10, 25, 50, 100, 150, 200 μg/mL) in 0.1 mL DMEM medium was added and incubated for 24 h. After that, the solution was removed and these cells were rinsed with PBS once carefully. 0.1 mL DMEM medium and 10 μL CCK-8 solution were added to each well, then the cells were incubated for another 2 h. The absorbance of samples (A_{sample}) at 450 nm in each well was determined using a microplate reader, while cell samples without any treatment ($A_{control}$) were used as a control. The *in vitro* cytotoxicity was evaluated by calculating the cell viability according to the following formula: $(A_{sample}-A_{blank})/(A_{control}-A_{blank}) \times 100\%$ (A_{blank} is

the absorbance from 0.1 mL DMEM medium and 10 μL CCK-8 solution without cells).

3.2.16 *In vitro* evaluation of PTT and enhanced CDT (CCK-8)

U87MG cells (~5 × 10^3) were seeded in 96-well plates and allowed to grow for 24 h. BCGC or BCGCR (0, 10, 25, 50, 100, 150, 200 μg/mL) in 0.1 mL DMEM medium was added and incubated for 24 h. After that, the solution was removed and these cells were rinsed with PBS twice carefully. Fresh DMEM medium was added to each well, and these cells were irradiated by a 980 nm laser (0.8 W/cm^2) for 5 min, then allowed to grow for another 4 h. 10 μL CCK-8 solution was added to each well, then the cells were incubated for another 2 h. The measurement of absorbance and the subsequent calculation of cell viability were conducted as described above.

3.2.17 Dead/Live cell co-staining FI induced by PTT and enhanced CDT

U87MG cells (~2 × 10^4) were seeded in a 48-well plate and allowed to grow for 24 h. BCGC or BCGCR (200 μg/mL) in 0.25 mL DMEM medium was added and incubated for 24 h. Untreated cells were used as control group (blank). After that, the solution was removed and these cells were rinsed with PBS twice. Fresh DMEM medium was added to wells, and these cells were irradiated (or not) under a 980 nm laser (0.8 W/cm^2) for 5 min. After irradiation, these cells were allowed to continue growing for another 4 h. 0.2 mL Fresh DMEM medium with 2 μM Calcein AM and 8 μM PI was added into each well for 30 min-staining, then cells were rinsed using PBS twice. Finally, fluorescence images acquired using a fluorescent microscope through GFP filter (Ex: 470 ± 20 nm, Em: 525 ± 25 nm) for Calcein AM and TRITC filter (Ex: 545 ± 12 nm, Em: 605 ± 35 nm) for PI.

3.2.18 Animals and tumor models

BALB/c female mice at the age of 5-6 weeks were purchased from Japan SLC, Inc. and used according to the regulations of Divisions of Experimental Animals, Nagoya University. Xenograft U87MG tumor model was built by s.c. injection of U87MG cells (~2 × 10^6) suspended in 100 μL PBS into the right hind limb of mice. *In vivo* experiments would be conducted until tumors with a single aspect of 5-7 mm were

formed after ~4 weeks.

3.2.19 FI of tumors in mice

Three mice bearing s.c. U87MG tumors in each group were i.v. injected with BCGC or BCGCR (5 mg/kg) in 100 μL PBS. To inhibit active recognition, mice from one group were pretreated with careful i.t. injection of cRGDfk (2 mM) in 100 μL PBS for 1 h before i.v. injection of BCGCR. Whole body fluorescence images were obtained before injection and 10 h, 1 day, 2 days, 4 days, and 7 days post-injection on an IVIS imaging system (Ex: 675 nm, Em: 720 nm). Fluorescence intensities were quantified by a region of interest (ROI) analysis, as described above.

3.2.20 FI of tumor tissue slices

Mice bearing s.c. U87MG tumors were treated as described in the previous section and sacrificed on the 2nd day. Tumor tissues of the mice were excised, fixed with 10% formalin, cut into slices (thickness: 10 μm) using a vibrating blade microtome, and fluorescence images acquired using a fluorescent microscope with a Cy5.5 filter (Ex: 650 ± 22 nm, Em: 720 ± 30 nm).

3.2.21 MRI of tumors in mice

Three mice bearing s.c. U87MG tumors in each group were i.v. injected with BCGC or BCGCR (20 μmol/kg Gd^{3+}) in 200 μL PBS. To inhibit active recognition, tumors from one group were pretreated with careful i.t. injection of cRGDfk (2 mM) in 100 μL PBS for 1 h before i.v. injection of BCGCR. MR images were acquired before injection and at 1 day, 2 days, 4 days, and 7 days post-injection using a 1.5T MRI system with the following parameters: T_1-weighted sequence, spin echo; TR/TE, 500/9.0 ms; image size, 128 × 256; slice thickness, 1 mm; slice number, 18; interval, 0.5 mm; field of view (FOV), 60 mm × 30 mm. The acquisition time for each scan was 01 min 05 s. Acquired MR images were transferred into the ImageJ software program for a quantitative analysis. Percentage signal enhancement (%SE) was calculated as the % difference ratio between the tumor signal intensity (SI) at each time point t and the SI before injection (t_0): $\%SE(t) = [(SI(t) - SI(t_0)]/SI(t_0) \times 100\%$

3.2.22 FI of tumors and main organs ex vivo

Three mice bearing s.c. U87MG tumors in each group were i.v. injected with BCGC or BCGCR (2 mg/kg) in 50 μL PBS and sacrificed after 2 days. The tumors and main organs, including the kidneys, liver, heart, spleen, stomach, intestines and lungs, were collected. Fluorescence images of tumors and these organs were acquired and their intensities were quantified by a region of interest (ROI) analysis, as described above.

3.2.23 Biodistribution analysis

Three mice bearing s.c. U87MG tumors in each group were i.v. injected with BCGC or BCGCR (10 mg/kg Cu^{2+}) in 200 μL PBS, followed by sacrifice and dissection after 2 days. Tumors and major organs, including the liver, kidneys, spleen, stomach, intestines, heart and lungs were collected and weighed, then cut into small pieces, then digested in 5 mL aqua regia with assistance by ultrasound. The Cu^{2+} concentrations were determined by ICP-AES, then the biodistribution %ID/g was calculated.

3.2.24 PTT and enhanced CDT evaluation of tumors in mice

Eight mice bearing s.c. U87MG tumors in each group were i.v. injected with 200 μL PBS or BCGCR (5 mg/kg Cu^{2+}) dispersed in 200 μL PBS. After 2 days, four mice among each group were irradiated by a 980 nm laser (0.8 W/cm^2) for 10 min, during which the temperature variation was monitored using an IR thermal camera. The tumor volume and body weight of each mouse were measured every three days until the 15^{th} day. Volumes were estimated according to the formula $V = (L \times W^2)/2$, in which length (L) and width (W) of each tumor were measured by a caliper. The relative tumor volumes of each mouse were calculated as V/V_0 (V_0 was the tumor volume before irradiation). Mice were sacrificed on the 15^{th} day and tumors were excised and photographed.

3.2.25 Histopathological analysis

Mice bearing s.c. U87MG tumors were treated as described in the previous section and sacrificed on the 2^{nd} day. The tumor tissues of mice were excised, fixed with 10% formalin, cut into slices (thickness: 4 μm), and stained with hematoxylin-eosin H&E.

To examine latent side effects, major organs including the heart, liver, spleen, lungs and kidneys from treated mice were collected on the 15th day, and applied to histopathological analysis. The images were acquired using a BZ-X700 microscope with bright field.

3.2.26 Hematological assay

Three healthy mice in each group were i.v. injected with 100 μL PBS or BCGCR (5 mg/kg Cu^{2+}) dispersed in 100 μL PBS. After 15 days, blood samples were collected for blood routine test.

3.2.27 Statistical Analysis

Results are expressed as the mean ± SD unless specially stated. Statistical comparison between two groups were evaluated by Student's t-test. Statistical significance was considered as $P < 0.05$, which can be divided as three types including (*) for $P < 0.05$, (**) for $P < 0.01$, and (***) for $P < 0.001$. All statistical calculations were conducted using OriginPro (OriginLab Corp., MA, USA).

3.3 Results and discussion

3.3.1 Design and characterization of BCGCR

The assembly of versatile BCGCR is illustrated in Figure 3-1a, including the preparation of BSA-capped CuS/Gd_2O_3 NPs (denoted as BCG) and subsequent decoration. BCG is produced using BSA as a template and stabilizer via a biomimetic mineralization according to the methods of previous reports, with some modification. [29, 30] Cu^{2+} and Gd^{3+} are anchored in BSA to form a Cu^{2+}-BSA-Gd^{3+} complex based on the affinity between amino acid residues and metal ions. Then, OH^- is introduced to adjust the pH (approaching 12), which induces BSA to extend into a hollow structure. [31] Afterwards, CuS nanocrystals form and gradually grow following the addition of S^{2-}, while Gd^{3+} reacts with OH^- to generate Gd_2O_3 NPs. The obtained BCG is further conjugated with a Cy5.5 fluorophore for NIR fluorescence with diminished scattering, absorption and autofluorescence from the living organism, which is suitable for highly sensitive *in vivo* FI. [32-36] Assisted by magnetic Gd_2O_3 NPs for MRI, which provides high spatial resolution and unlimited penetrability

[37-40], this nanoprobe can be applied for dual modality imaging to guide cancer treatment using an NIR laser. Then sulfo-NHS-acetate was introduced to block -NH_2 of BSA to prevent self-polymerization in the subsequent peptide conjugation. The assembly of RGD peptide facilitates active transport towards tumors, since it has been accepted as a valid tumor-targeting ligand for selective recognition towards $\alpha_v\beta_3$ integrin overexpressed on the membrane of various tumor cells. [41, 42]

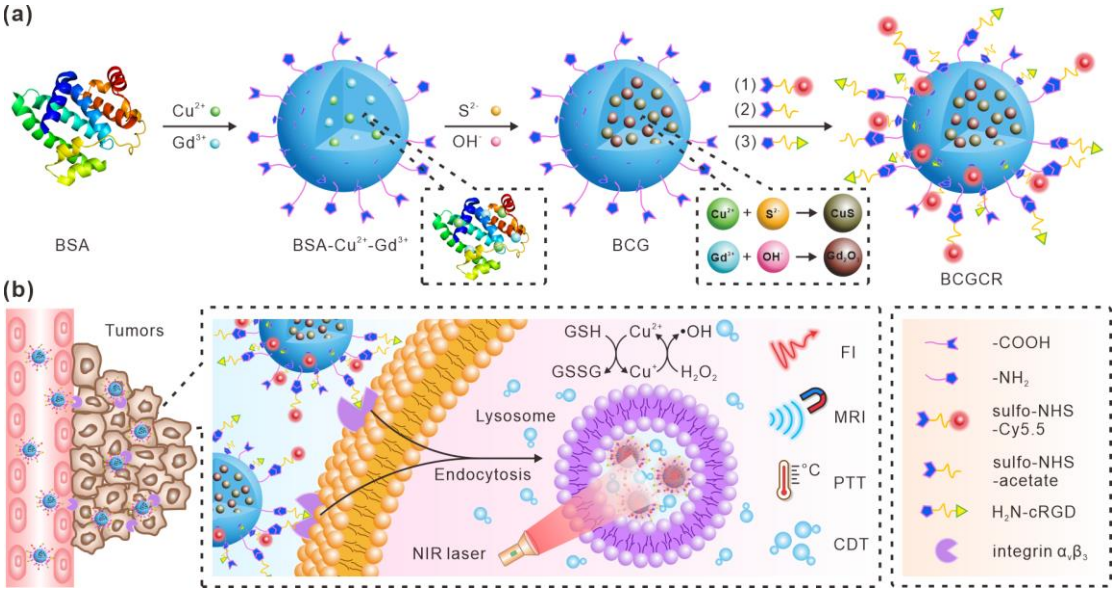

Figure 3-1. Schematic illustration of BCGCR. (a) The design. (b) The mechanisms of fluorescence/MR bimodal imaging-guided PTT and intensified CDT of targeted tumors.

Figure 3-1b depicts the mechanism of tumor detection and photo-assisted treatment using BCGCR. Benefiting from the enhanced permeability and retention (EPR) effect, as well as $\alpha_v\beta_3$ integrin-mediated active recognition, BCGCR can partially arrive at tumors after intravenous administration, and preferentially accumulate into lysosomes by endocytosis. The process of BCGCR accumulation can be monitored in real time using both NIR FI from Cy5.5 fluorophores with an intense signal and tissue-penetrable MRI owing to Gd element. Guided by the dual-mode imaging, the tumor site is exposed under NIR laser irradiation for treatment. The hyperthermia produced by internal CuS with high PCE ablates tumors and simultaneously accelerates the ionization of CuS. Then the generation of ·OH is promoted by both hyperthermia and released Cu^{2+}, leading to the disintegration of cellular proteins and

DNA. As a consequence, the synergistic PTT and enhanced CDT of tumors can be realized under guidance by bimodal imaging.

We first examined and ascertained the components of BCG. The X-ray photoelectron spectroscopy (XPS) spectrum of BCG in Figure 3-2 includes several characteristic peaks attributed to O 1s, S 2p, Cu 2p, Gd 4d, suggesting the existence of these elements. The composition of BCG was further verified by an energy dispersive spectrometry (EDS) analysis with element line scanning data (Figure 3-3a). The X-ray diffraction (XRD) pattern of BCG exhibited distinct peaks at 29.42° and 47.07° assigned to the characteristic peaks of both hexagonal CuS and cubic Gd_2O_3, indicating the successful preparation of these nanocrystals (Figure 3-3b). Next, the BCG morphology was investigated by transmission electron microscopy (TEM), exhibiting a uniform spherical structure with an average size of 5 nm (Figure 3-4a), which was slightly smaller than the hydrodynamic size calculated by a dynamic light scattering (DLS) analysis (~13 nm) (Figure 3-4b). Besides, it is obvious that the broad NIR absorption band from BCG was consistent with the one from Gd-free CuS NPs, indicating strong localized surface plasmon resonance (LSPR) from inner CuS nanocrystals (Figure 3-4c).

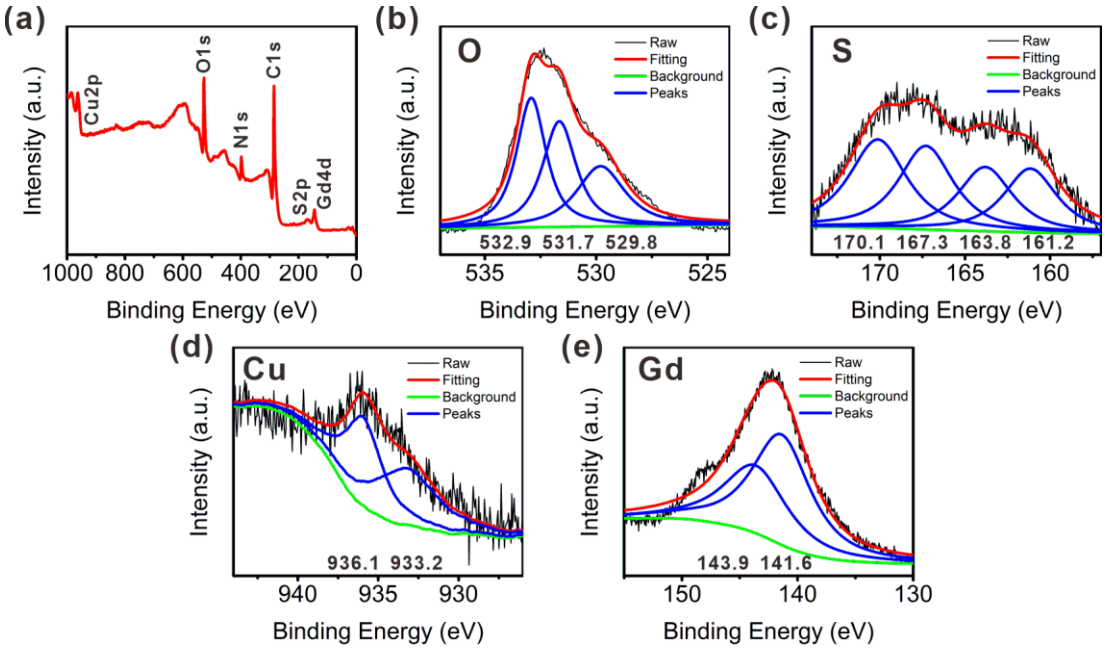

Figure 3-2. XPS spectra of BCG. (a) Original spectrum. (b) Characteristic peaks of O 1s (−COOH and −OH in BSA: 532.9 ev, $Gd(OH)_3$: 531.7 ev, Gd_2O_3: 529.8 ev). (c)

Characteristic peaks of S 2p ($CuSO_4$: 170.1 ev and 167.3 ev, CuS: 163.8 ev and 161.2 ev). (d) Characteristic peaks of Cu 2p (CuS: 933.2 ev). (e) Characteristic peaks of Gd 4d (Gd_2O_3: 143.9 ev, $Gd(OH)_3$: 141.6 ev). [30, 43]

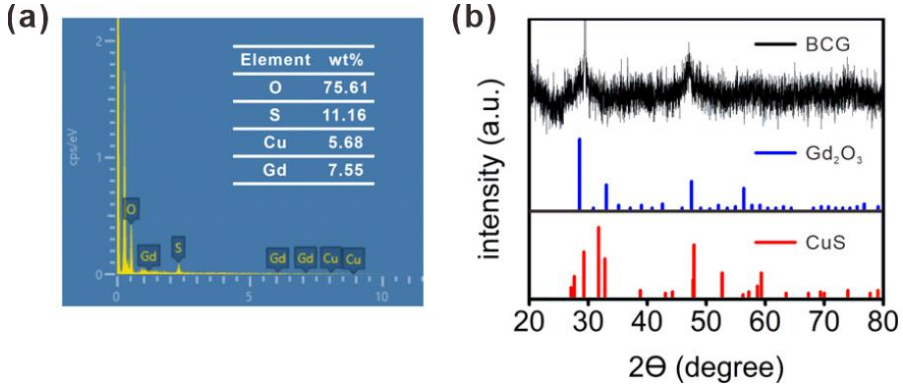

Figure 3-3. (a) The EDS analysis of BCG and wt% for O, S, Cu and Gd elements. (b) Powder XRD patterns of BCG, as referenced by the standard hexagonal CuS (JCPDS 06-0464) and cubic Gd_2O_3 (JCPDS 12-0797), in which 1/8 of the original mass of BSA was used to synthesize BCG to reduce the interference towards the signal of CuS and Gd_2O_3.

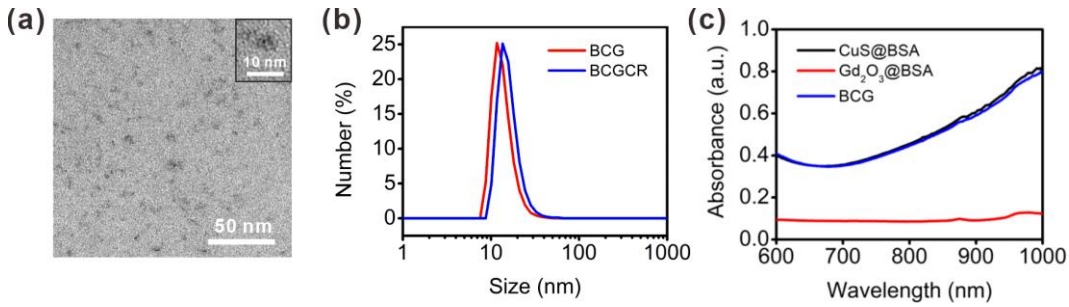

Figure 3-4. (a) TEM image of BCG. (b) The DLS analysis of BCG and BCGCR. (c) Absorption spectra of CuS capped by BSA, Gd_2O_3 capped by BSA and BCG (20 mg/mL) with similar synthesis conditions.

Inspired by the successful preparation, we used the sulfo-NHS-Cy5.5 fluorophore and cRGDfk to decorate BCG into a multifunctional nanoprobe (BCGCR) (Figure 3-5). TEM indicates that BCGCR took on a similar morphology to BCG (Figure 3-6a). A DLS analysis shows that the average hydrodynamic size of BCGCR was approximately 16 nm (Figure 3-4b), which was slightly larger than that of BCG due to the introduction of sulfo-Cy5.5, acetyl amino groups and cRGDfk. The zeta potential

of BCGCR remained negative (-16.8 mV) in comparison to BCG (-13.9 mV) due to the negatively charged sulfo groups from sulfo-Cy5.5 and carboxyl groups from BSA and RGD (Figure 3-6b). The absorption spectra illustrate that BCGCR inherited two characteristic absorption peaks (640 and 685 nm) from sulfo-Cy5.5 and strong NIR absorbance (700-1000 nm) from CuS NPs (Figure 3-6c). In order to assess the ability of BCGCR as a bimodal imaging agent, we first measured the fluorescence signal. As depicted in Figure 3-6d, the fluorescence spectrum of BCGCR resembled that of sulfo-Cy5.5, exhibiting strong NIR fluorescence around 710 nm, which showed great potential for *in vivo* FI. The red-shift of BCGCR fluorescence after modification probably resulted from the change in the chemical environment around the sulfo-Cy5.5 fluorophore. It was also found that the brightness of T_1-weighted MR images was amplified with the concentration of BCGCR, and the longitudinal relaxivity (r_1) was calculated as ~15.3 mM^{-1} s^{-1} per Gd^{3+} in aqueous solution (Figure 3-6e), almost 4 times as high as that of the clinical paramagnetic contrast agent Gd-DOTA (3.4 mM^{-1} s^{-1}). [44] The elevated r_1 relaxivity probably arose from the spatial confinement of encapsulated Gd within BSA, which impeded rotation and prolonged the tumbling time (τ_R). [45, 46] Moreover, BCGCR was stable in three different types of solution without any size change for at least one week (Figure 3-6f). Based on these results, BCGCR is expected to have applications as both a fluorescent nanoprobe and an effective T_1-weighted MR contrast agent for dual-modal imaging.

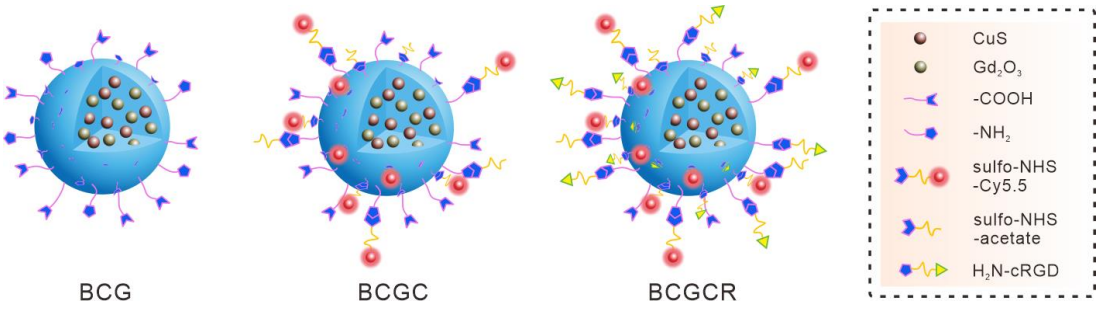

Figure 3-5. Cartoon diagrams of BSA-CuS-Gd_2O_3 (BCG), BSA-CuS-Gd_2O_3-Cy5.5 (BCGC) and BSA-CuS-Gd_2O_3-Cy5.5-RGD (BCGCR).

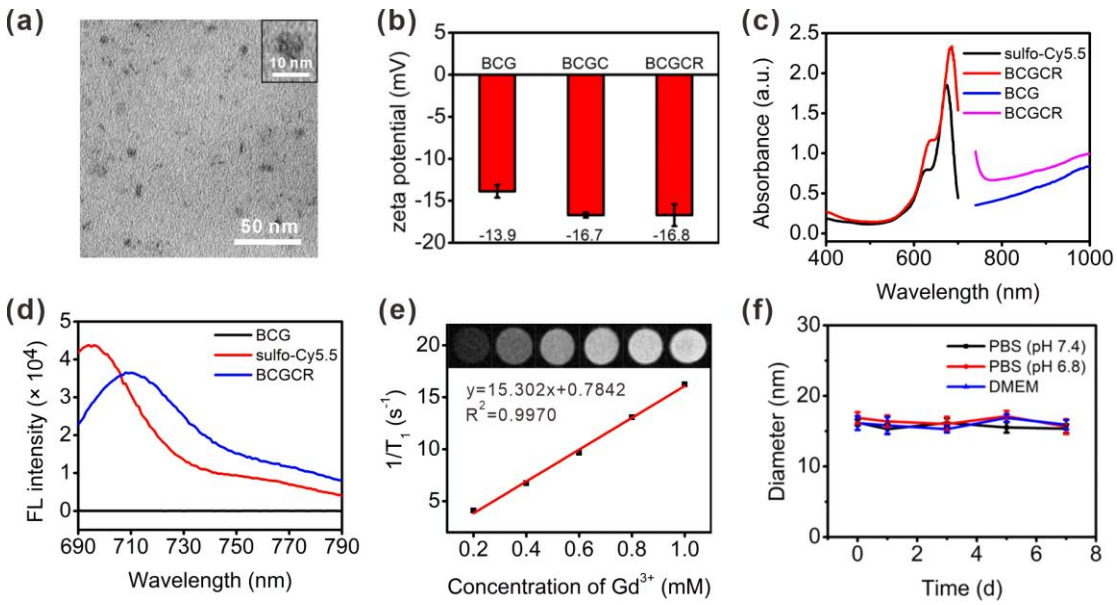

Figure 3-6. (a) TEM image of BCGCR. (b) Zeta potentials of BCG, BCGC and BCGCR. (c) Absorption spectra of sulfo-Cy5.5 (0.1 mg/mL, black), BCGCR (2 mg/mL, red), BCG (20 mg/mL, blue) and BCGCR (25 mg/mL, pink). (d) Fluorescence (FL) spectra of BCG (10 mg/mL), sulfo-Cy5.5 (2 μg/mL) and BCGCR (1 mg/mL). λ_{ex} = 660 nm. (e) Plots of $1/T_1$ of BCGCR versus different Gd^{3+} concentrations from 0.2 to 1.0 mM. Insert: T_1-weighted MR images (1.5 T) of aqueous BCGCR with Gd^{3+} concentrations of 0, 0.2, 0.4, 0.6, 0.8, 1.0 mM. TR/TE, 500/9.0 ms. (f) A long-term size investigation of BCGCR in PBS (pH 7.4), PBS (pH 6.8) and DMEM using a DLS analysis.

3.3.2 Evaluation of the photothermal effect and catalytic performance

We next evaluated the photothermal performance by irradiation with a 980 nm laser. As shown in Figure 3-7, the solution temperature exhibited a positive correlation with both the BCGCR concentration and the laser power density. For instance, after 5 min irradiation with a power density of 0.8 W/cm^2, the IR thermal image of the BCGCR solution (0.5 mM Cu^{2+}) gradually became bright and its temperature dramatically increased from 25.3°C to 50.6°C, whereas a negligible temperature increase was observed in ultrapure water. The PCE (η) of BCGCR was calculated as 30.3% (Figure 3-8a-b & Note 3-1), which was comparable with that of previously reported CuS NPs (Table 3-1). Besides, BCGCR possessed excellent photothermal stability for at least

five cycles of heating by irradiation and subsequent natural cooling, indicating great potential for application in PTT of tumors (Figure 3-8c).

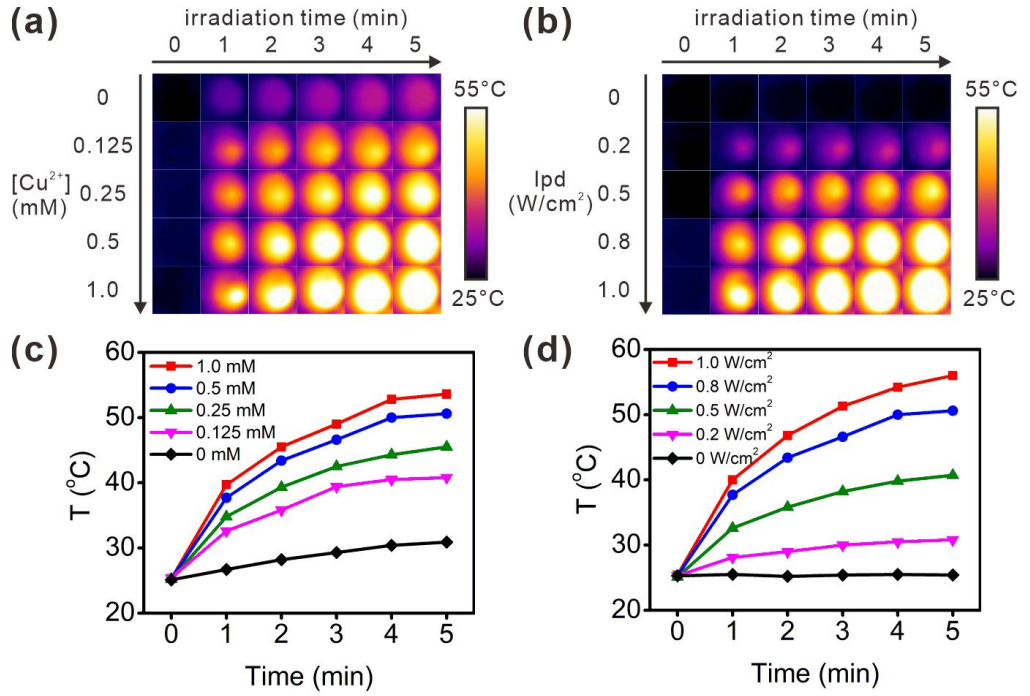

Figure 3-7. IR thermal images and average temperature variations of BCGCR solution under 980 nm laser irradiation for 5 min. (a & c) Different concentrations of BCGCR (0~1.0 mM Cu^{2+}) with a power density of 0.8 W/cm^2. (b & d) BCGCR (0.5 mM Cu^{2+}) with different laser power densities (lpd) (0~1 W/cm^2).

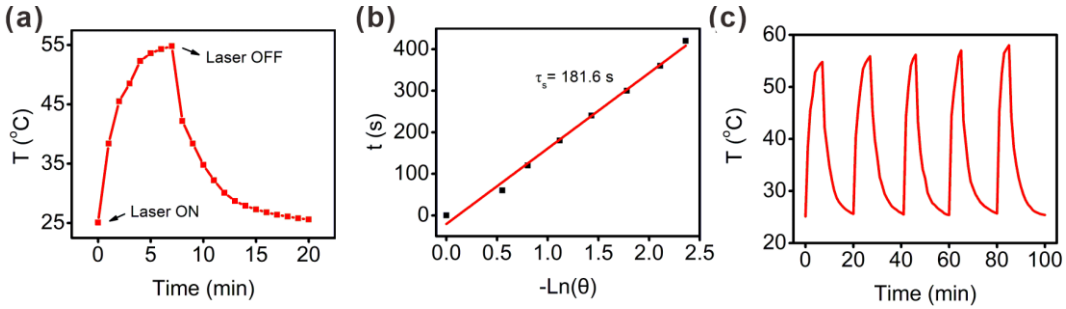

Figure 3-8. (a) Temperature variation of BCGCR solution (1 mM Cu^{2+}) under 980 nm laser irradiation (0.8 W/cm^2) for 7 min followed by natural cooling. (b) Measurement of the thermal time constant (τ_s) by linear fit of the time point t vs (- Lnθ) during the natural cooling period. The PCE was calculated as 30.3% according to Note 3-1. (c) Photothermal stability of aqueous BCGCR (1 mM Cu^{2+}) for five cycles of heating by irradiation (980 nm, 0.8 W/cm^2) and natural cooling.

Note 3-1. PCE Evaluation of BCGCR

PCE (η) is used to evaluate the extent of conversion of absorbed light into temperature increase, which can be calculated according to the method of previous reports [47-49] with the modified formula:

$$\eta = \frac{hS(T_{max,mix} - T_{max,s})}{I(1 - 10^{-A_\lambda})} \times 100\%$$

where h is the heat transfer coefficient; S is the surface area of the cuvette; $T_{max,mix}$ is the maximum temperature of solvent with nanoparticles (54.8°C from Figure 3-8a), while $T_{max,s}$ is that of solvent alone after irradiation for the same time (31.2°C); I is the laser power (0.8 W/cm^2 × π × (0.5 cm)^2 = 0.628 W); A_λ is the absorbance of nanoparticles at the wavelength λ (A_{980} = 0.86). hS can be calculated as follows:

$$hS = \frac{mC_{water}}{\tau_s}$$

$$\tau_s = -\frac{t}{ln\theta} = -\frac{t}{ln\frac{T - T_{sur}}{T_{max,mix} - T_{sur}}}$$

where m is the mass of the sample solution (0.3 g); C_{water} is the heat capacity of water (4.2 J g^{-1} K^{-1}); τ_s is the thermal time constant that can be determined as the slope by linear fit of the time point t vs (- Lnθ) during the natural cooling period; T is the temperature at the time point t; T_{sur} is the temperature of the surroundings.

According to Figure 3-8b, τ_s is calculated as 181.6 s. Hence,

$$hS = \frac{mC_{water}}{\tau_s} = \frac{0.3\ g \times 4.2\ J\ g^{-1}\ K^{-1}}{181.6\ s} = 0.00694\ W\ K^{-1}$$

$$\eta = \frac{hS(T_{max,mix} - T_{max,s})}{I(1 - 10^{-A_\lambda})} \times 100\% = \frac{0.00694\ W\ K^{-1} \times (327.95\ K - 304.35\ K)}{0.628\ W \times (1 - 10^{-0.86})} \times 100\%$$

$$= \frac{0.1638\ W}{0.5413\ W} \times 100\% = 30.3\%$$

Table 3-1. PCE Comparison between reported CuS NPs and BCGCR

CuS NPs	Irradiation wavelength (nm)	PCE (%)	Reference
Gd:CuS@BSA	980	32.3	30
Gd_2O_3/CuS NDs	785	45.5	29
T-MAN	808	70.1	21
PFN	1064	30.17	27
BSA@CuS@DOX	1064	52.81	50
Gd/CuS@PEI-FA-PS	1064	26.7	51
IONF@CuS	1064	42	52
RGD-CuS DENPs	1064	49.8	53
CuSCDs	808	39.7	54
CuS-MnS_2	808	67.5	55
Cu_2MnS_2	1064	49.4	56
HCuS@Cu_2S@Au	808	35	57
BCGCR	**980**	**30.3**	**This work**

To investigate the Fenton-like catalytic efficiency of BCGCR, methylene blue (MB), which can be degraded by ·OH and give rise to decreased absorbance, was selected as an indicator to reflect the ·OH generation level. [11, 15] As the absorbance of Cy5.5 from BCGCR overlapped and probably interfered with that of MB, BCG rather than BCGCR was used to evaluate ·OH production. Figure 3-9a shows that MB gradually faded under the condition of H_2O_2, BCG and GSH, suggesting that the generation of ·OH was induced by the Fenton-like reaction. In comparison, MB absorbance almost remained constant after incubation with BCG, BCG + GSH or BCG + H_2O_2 (Figure 3-9b). Without the help of Cu, it was difficult for MB degradation to proceed (Figure 3-9c). This Cu-triggered Fenton-like reaction could smoothly proceed at varying pH values of 5.4 simulating the weak acidity in lysosomes, 6.4 as the TME and 7.4 as the physiological environment (Figure 3-9d). In

order to verify the photothermal-intensified ·OH generation, we assumed 50°C as the temperature that could be reached for PTT and rapid MB degradation was observed at high temperatures (Figure 3-9d). Correspondingly, MB degradation was strengthened with the help of laser irradiation (Figure 3-9b). These data suggest the potential application of BCG (or BCGCR) as an efficient photothermal-enhanced CDT agent for cancer theranostics.

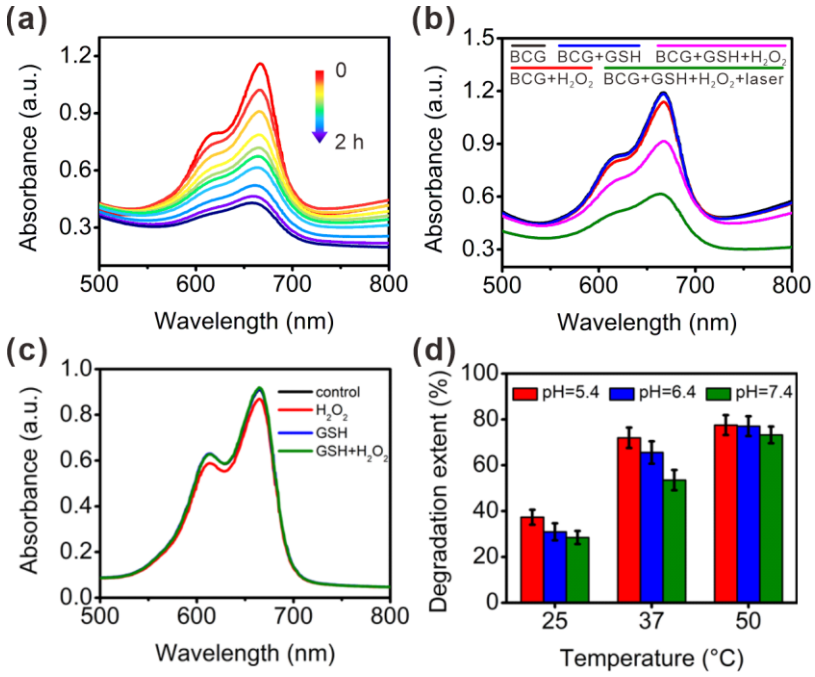

Figure 3-9. (a) Absorption spectra of MB (10 μg/mL) incubated with BCG-GSH (0.5 mM Cu^{2+}) and H_2O_2 (20 μM) at pH 5.4 for 0, 3, 5, 10, 15, 20, 30, 60, 90, 120 min. (b) Absorption spectra of (10 μg/mL) MB under different conditions at pH 5.4 with or without laser irradiation (980 nm, 0.8 W/cm^2) for 5 min. (c) Absorption spectra of (10 μg/mL) MB with H_2O_2 (20 mM), GSH (1 mM) or H_2O_2 + GSH at pH 5.4 for 5 min. (d) The extent of MB (10 μg/mL) degradation reflected by decreased absorbance after incubation with BCG-GSH (0.5 mM Cu^{2+}) and H_2O_2 (20 mM) at varying pH values and temperatures for 20 min.

3.3.3 *In vitro* bimodal imaging performance

Prompted by the above-mentioned characteristics, we used $\alpha_v\beta_3$ integrin-positive U87MG tumor cells to investigate its effects in *in vitro* fluorescence/MR bimodal imaging. [58, 59] Fluorescence images reveal that NIR fluorescence inside U87MG cells became bright with incubation time (Figure 3-10). The effective uptake of

BCGCR by U87MG cells was confirmed by a set of confocal fluorescence images at different depths (Figure 3-11). It was further proven by a colocalization study with the help of a lysosomal tracker that intracellular flecky fluorescence was principally located at the lysosomes (Figure 3-12). In contrast, weak fluorescence was found in (II) U87MG cells incubated with RGD-free BCGC, (III) U87MG cells pretreated with RGD followed by incubation with BCGCR or (IV) $\alpha_v\beta_3$ integrin-negative HEK293T cells incubated with BCGCR (Figure 3-13a). Flow cytometry shows that the fluorescence intensity in U87MG cells incubated with BCGCR was remarkably stronger in comparison to the other three above-mentioned groups (Figure 3-13b). The bright NIR fluorescence from BCGCR-treated U87MG cells was also observed against that from other groups (almost 4-fold) by FI of cell pellets (Figure 3-13c, top & 3-13d, red), which is well-correlated with the above-mentioned results.

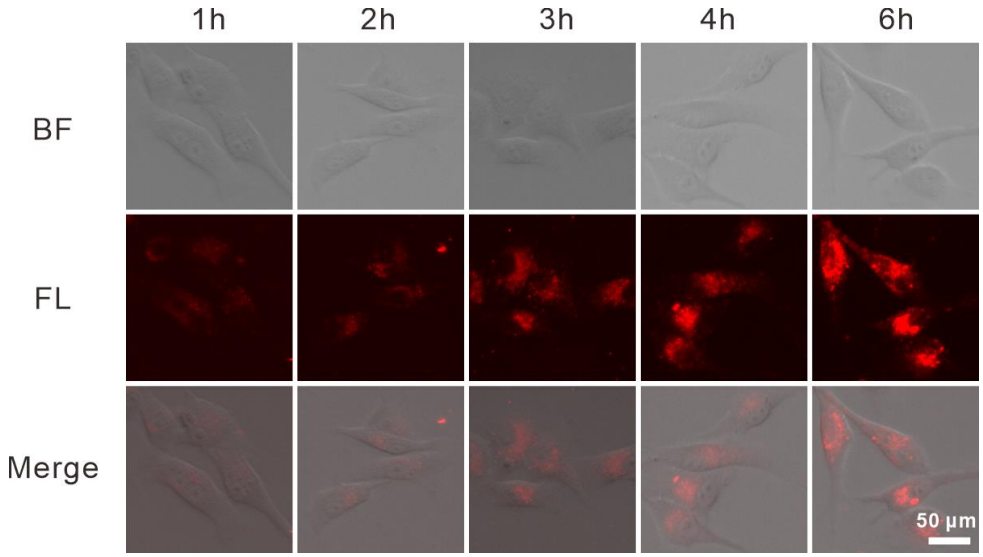

Figure 3-10. Fluorescence images of U87MG cells after incubation with BCGCR (100 μg/mL) for 1, 2, 3, 4, and 6 h.

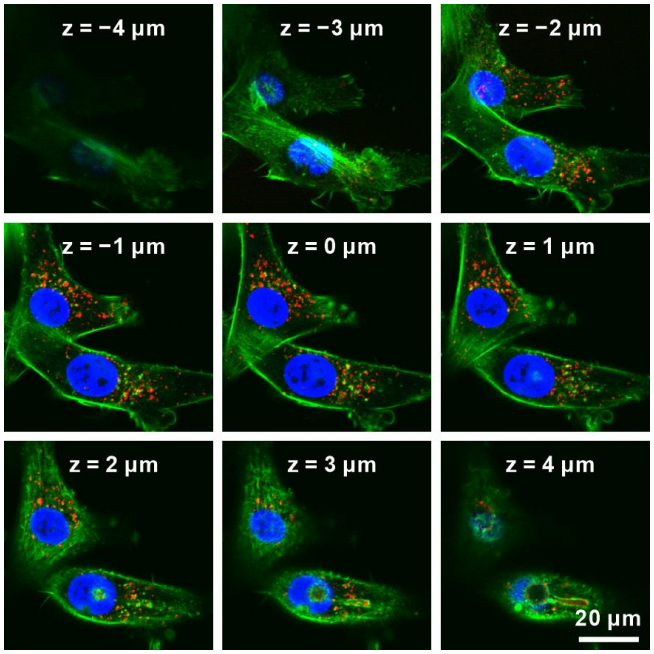

Figure 3-11. A set of confocal fluorescence images at different depths of U87MG cells incubated with BCGCR (50 µg/mL) (red) for 2 h, followed by co-staining with 0.1 µg/mL Hoechst 33342 (blue) and 300 nM Alexa Fluor™ 488 Phalloidin (green) for 30 min.

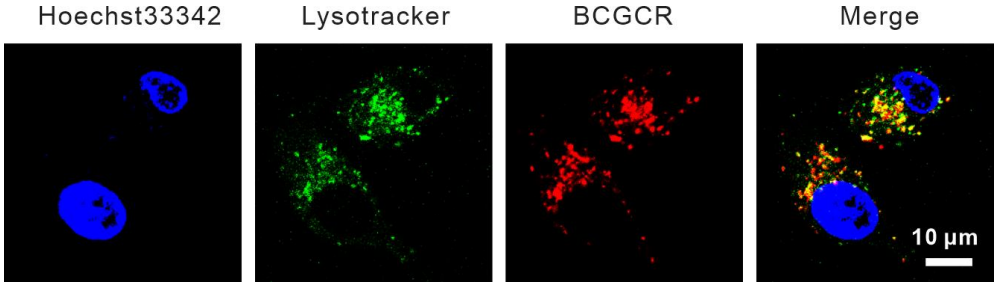

Figure 3-12. Colocalization study of U87MG cells after incubation with BCGCR (50 µg/mL) (red) for 2 h, followed by co-staining with 0.1 µg/mL Hoechst 33342 (blue) and 200 nM Lysotracker (green) for 20 min.

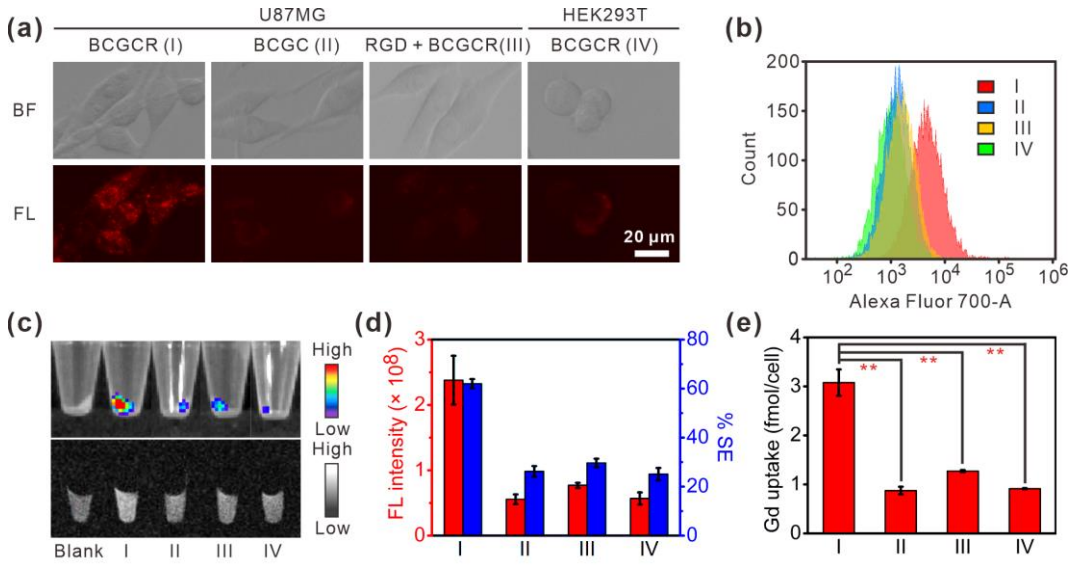

Figure 3-13. *In vitro* bimodal imaging of cells. (a) Fluorescence images of (I) U87MG cells incubated with BCGCR (100 μg/mL, 2 h), (II) U87MG cells incubated with BCGC (100 μg/mL, 2 h), (III) U87MG cells incubated with RGD (10 μM, 1 h) followed by BCGCR (100 μg/mL, 2 h) or (IV) HEK293T cells incubated with BCGCR (100 μg/mL, 2 h) (Ex: 650 ± 22 nm, Em: 720 ± 30 nm). (b) Flow cytometry assays of fluorescence intensity in cells after similar treatments with BCGC or BCGCR (10 μg/mL) for 2 h (Ex: 633 nm, Em: 710 ± 25 nm). (c) Fluorescence (top) (Ex/Em = 675/720 nm) images of cell pellets after similar treatments with BCGC or BCGCR (10 μg/mL) for 2 h and T_1-weighted MR (bottom) (TR/TE = 500/9.0 ms at 1.5 T) images of cell pellets after similar treatments with BCGC or BCGCR (10 μM Gd^{3+}) for 24 h. (d) Statistics of total FL intensities (red) and average %MR signal enhancements (% SE, blue) of cell pellets in (c). (e) The ICP-AES analysis of the average Gd uptake in each cell after indicated treatments in (c, bottom). Values denote the mean ± SD (n = 3, $^{**}P < 0.01$).

Along with the strong intracellular fluorescence, T_1-weighted MR brightness was enhanced in U87MG cells incubated with BCGCR (Figure 3-13c, bottom). The percentage signal enhancement (% SE) against untreated U87MG cell pellets was ~62.0%, which was higher than that of U87MG cells incubated with BCGC (26.2%), U87MG cells pretreated with RGD followed by incubation with BCGCR (29.7%), and HEK293T cells incubated with BCGCR (25.1%) (Figure 3-13d, blue). An

ICP-AES analysis that was performed to investigate the uptake of Gd by cells demonstrates a large amount of intracellular Gd (~3.1 fmol/cell) in U87MG cells incubated with BCGCR against that from other groups (Figure 3-13e). These findings implies that $\alpha_v\beta_3$ integrin overexpressed on the membrane of U87MG cells played a significant role in active recognition and subsequent uptake, leading to strong intracellular NIR fluorescence intensity and MR contrast for *in vitro* bimodal imaging.

3.3.4 *In vitro* synergetic PTT and enhanced CDT evaluation

To investigate the *in vitro* anticancer efficacy of BCGCR under NIR irradiation, we first assessed the feasibility of CDT. A GSH assay kit was applied to monitor the intracellular GSH level. A large quantity of GSH in U87MG cells was consumed after treatment with BCGCR, suggesting the conversion from Cu^{2+} to Cu^{+} for the subsequent Fenton-like reaction (Figure 3-14a). Then we evaluated the intracellular ROS generation with monitoring by 2,7-dichlorodihydrofluorescein diacetate (DCFH-DA), which is able to be oxidized into DCF with green fluorescence emission. [60] As described in Figure 3-14b, green fluorescence could not be observed on U87MG cells treated with either BCGC or BCGCR without laser irradiation, indicating little intracellular ROS generation. Once exposed to laser irradiation, ROS produced by U87MG cells incubated with BCGCR was dramatically enhanced, which demonstrates the photothermal-intensified Fenton-like reaction. In comparison, weak fluorescence was found on U87MG cells treated with BCGC, even if exposed under laser irradiation due to the limited uptake.

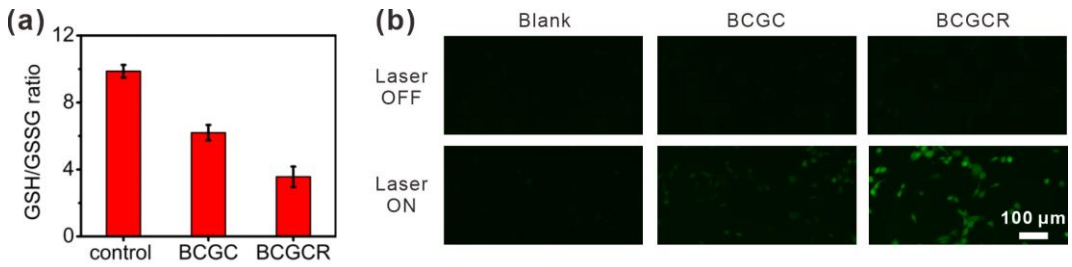

Figure 3-14. (a) The GSH level in U87MG cells (untreated, incubated with 100 μg/mL BCGC or BCGCR, 6 h). (b) Fluorescence images of U87MG cells (untreated, incubated with 100 μg/mL BCGC or BCGCR, 6 h) followed by 10 μM DCFH-DA staining with or without laser irradiation (980 nm, 0.8 W/cm^2) for 5 min (Ex: 470 ± 20

nm, Em: 525 ± 25 nm).

Before applying BCGCR to photo-assisted therapies of *in vitro* U87MG cells, we investigated its cytotoxicity towards normal HEK293T cells via a cytotoxicity assay (CCK-8). Figure 3-15a suggests that BCGCR had no influence on cell viability towards HEK293T cells, indicating excellent biocompatibility for cell studies. Then we tried to examine the PTT/CDT efficacy of BCGCR against tumor cells. Figure 3-15b shows that BCGC and BCGCR had negligible cytotoxicity against U87MG cells without laser irradiation, at concentrations of up to 200 μg/mL. However, it is suggested that the cell viability was negatively correlated with dosage upon laser irradiation (0.8 W/cm^2) for 5 min. In detail, the relative cell viability declined to ~27.0% for 100 μg/mL BCGCR-treated U87MG cells exposed to laser irradiation, which was remarkably lower than that for 100 μg/mL BCGC-treated U87MG cells (~69.2%). The cell death caused by the synergistic PTT and CDT was further demonstrated by fluorescence staining of U87MG cells via calcein AM (live) and propidium iodide (PI) (dead) (Figure 3-16). These results demonstrate that BCGCR had the potential to ablate *in vitro* U87MG tumor cells under laser irradiation by CDT-assisted PTT.

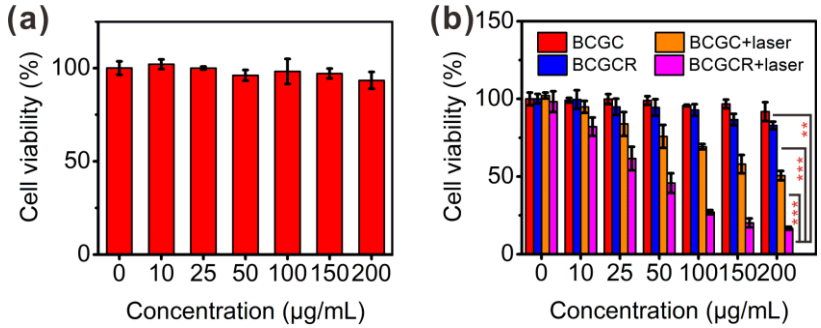

Figure 3-15. (a) HEK293T cell viability after incubation with different concentrations of BCGCR for 24 h. (b) U87MG cell viability after incubation with different concentrations of BCGC or BCGCR for 24 h followed by exposure (or non-exposure) under laser irradiation (980 nm, 0.8 W/cm^2) for 5 min. Values denote the mean ± SD (n = 5, $^{**}P < 0.01$, $^{***}P < 0.001$).

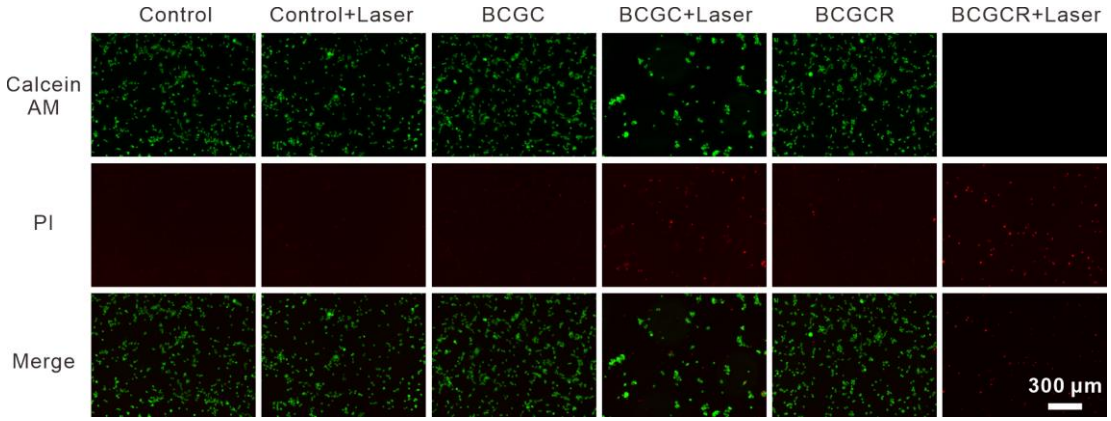

Figure 3-16. Fluorescence images of live (green) and dead (red) U87MG cells. Cells were incubated with BCGC or BCGCR (200 μg/mL) for 24 h followed by exposure under laser irradiation (or non-exposure) (980 nm, 0.8 W/cm^2) for 5 min, and stained with Calcein AM and PI for 30 min.

3.3.5 *In vivo* tumor-targeted bimodal imaging performance

We then applied BCGCR to the detection of U87MG tumor xenografts in living mice via NIR fluorescence and MR dual-modal imaging. Figure 3-17a indicates that after the intravenous (i.v.) injection of BCGCR (5 mg/kg, 100 μL), fluorescence at U87MG tumor gradually augmented, which peaked at 2 d and lasted for at least one week. This strong fluorescence at tumor could be effectively reduced by intratumoral (i.t.) injection of free cRGDfk (~1.51-fold lower) due to the lack of RGD-mediated active transport (Figure 3-17b). Besides, a ~1.58-fold decrease in fluorescence intensity at the tumor was observed in mice that received i.v. injection of BCGC compared with those treated with BCGCR. These apparent differences in fluorescence intensity were further confirmed by the FI of tumor tissue slices resected from mice at 2 days after i.v. injection (Figure 3-18). In accordance with the FI findings, the T_1-weighted MR contrast of the U87MG tumor gradually intensified until 2 days after i.v. injection of BCGCR (20 μmol/kg Gd^{3+}, 200 μL) (Figure 3-19a). The maximum signal enhancement (%SE) of the tumor was ~50.8% at 2 days, which was nearly 1.50-fold as high as that with blocking by RGD and 1.73-fold higher than that with BCGC treatment (Figure 3-19b). This enhanced brightness could be observed throughout the entire tumor tissue on a set of multi-slice MR images, suggesting the superb tissue penetrability of BCGCR (Figure 3-20).

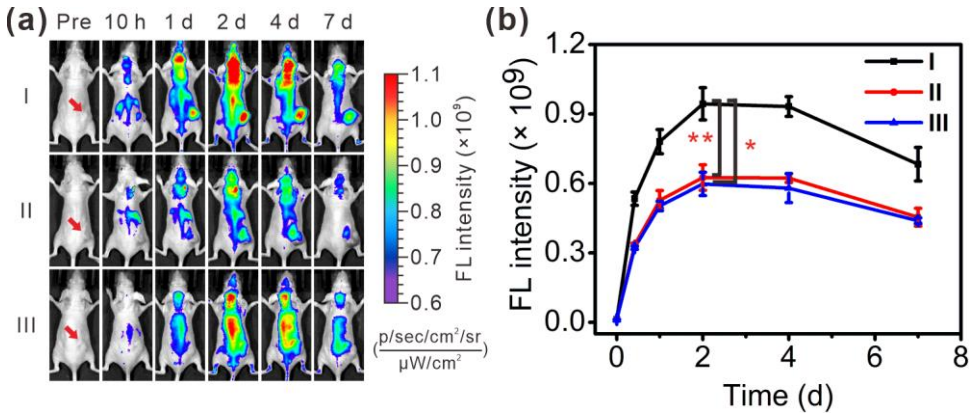

Figure 3-17. (a) FL images and (b) Variations of average FL intensity at tumor of mice receiving (I) i.v. injection of BCGCR (5 mg/kg, 100 μL), (II) i.t. injection of free cRGDfk (2 mM, 100 μL) followed by i.v. injection of BCGCR (5 mg/kg, 100 μL) 1 h later, (III) i.v. injection of BCGC (5 mg/kg, 100 μL) at 0 h, 10 h, 1 day, 2 days, 4 days, 7 days (Ex: 675 nm, Em: 720 nm). Red arrows indicate the tumor locations in mice. Values denote the mean ± SD (n = 3, **P* < 0.05, ***P* < 0.01).

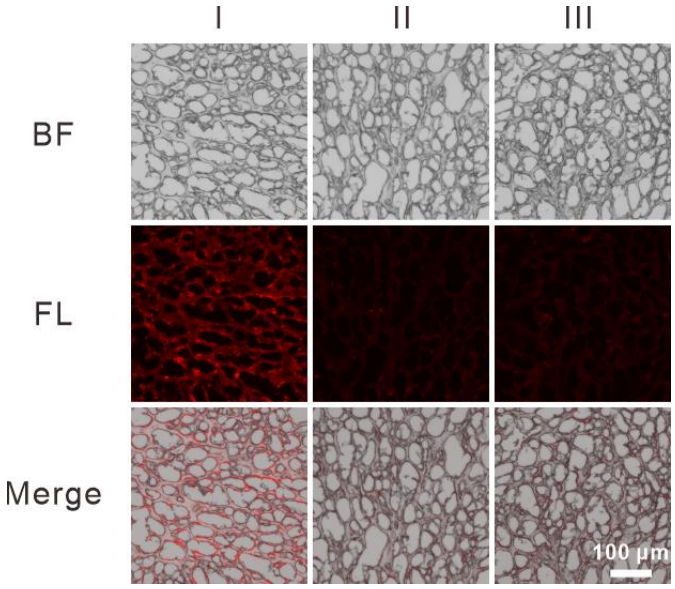

Figure 3-18. Fluorescence images of tumor tissue slices resected from U87MG tumor bearing mice at 2 days after (I) i.v. injection of BCGCR (5 mg/kg, 100 μL), (II) i.t. injection of free cRGDfk (2 mM, 100 μL) followed by i.v. injection of BCGCR (5 mg/kg, 100 μL) 1 h later, (III) i.v. injection of BCGC (5 mg/kg, 100 μL).

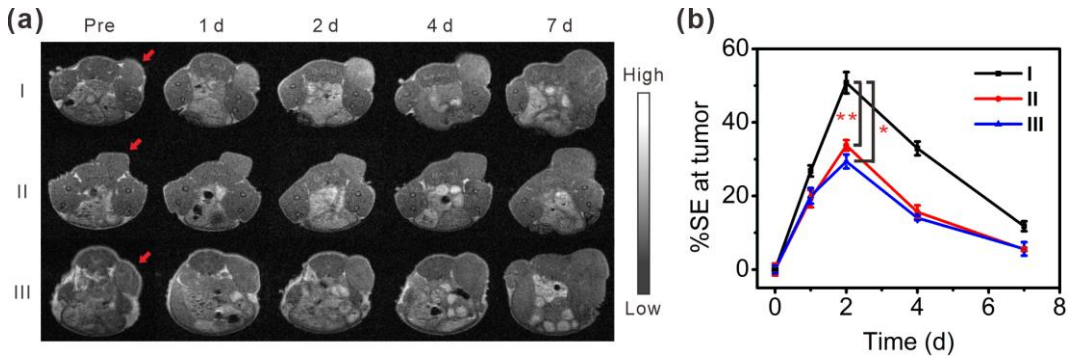

Figure 3-19. (a) T_1-weighted MR images and (b) Variations of average %SE at tumor of mice receiving (I) i.v. injection of BCGCR (20 μmol/kg Gd^{3+}, 200 μL), (II) i.t. injection of free cRGDfk (2 mM, 100 μL) followed by i.v. injection of BCGCR (20 μmol/kg Gd^{3+}, 200 μL) 1 h later, (III) i.v. injection of BCGC (20 μmol/kg Gd^{3+}, 200 μL) at 0 h, 1 day, 2 days, 4 days, 7 days (TR/TE = 500/9.0 ms at 1.5 T). Red arrows indicate the tumor locations in mice. Values denote the mean ± SD (n = 3, $*P < 0.05$, $**P < 0.01$).

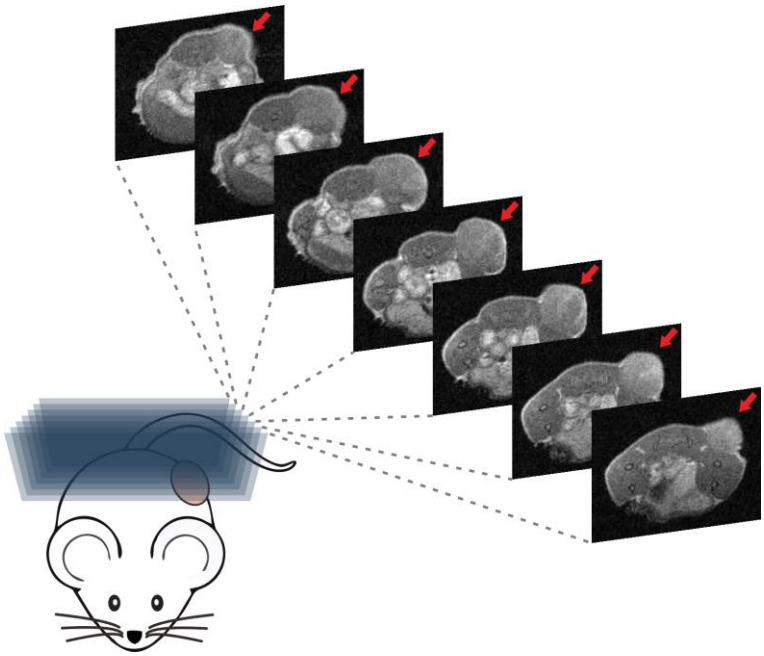

Figure 3-20. T_1-weighted multi-slice MR images of mice at 2 days after the i.v. injection of BCGCR (20 μmol/kg Gd^{3+}, 200 μL) (TR/TE = 500/9.0 ms at 1.5 T). Red arrows indicate tumor locations in mice.

The biodistribution of BCGC and BCGCR was then investigated by *ex vivo* FI of the main organs and tumors resected from mice. Figure 3-21a&b shows that at 2 days after i.v. injection, BCGCR-treated tumors exhibited strong fluorescence, which was

almost 2.04-fold higher than BCGC-treated ones, although most fluorescence was distributed in the liver in both groups. Furthermore, an accurate biodistribution study by ICP-AES reveals that the %ID/g of BCGCR-treated tumors was ~13.3%, which was higher than that of other major organs, with the exception of the liver and BCGC-treated tumors (~7.2%) (Figure 3-21c). Such a high uptake of BCGCR benefited from RGD-induced active recognition assisted by the EPR effect. These findings correspond to strong fluorescence and intensified MR contrast at the tumor, as monitored by real-time imaging of living mice, demonstrating that BCGCR could be efficiently accumulated in U87MG tumors *in vivo* and act as a sensitive fluorescence probe and MR contrast agent for bimodal imaging.

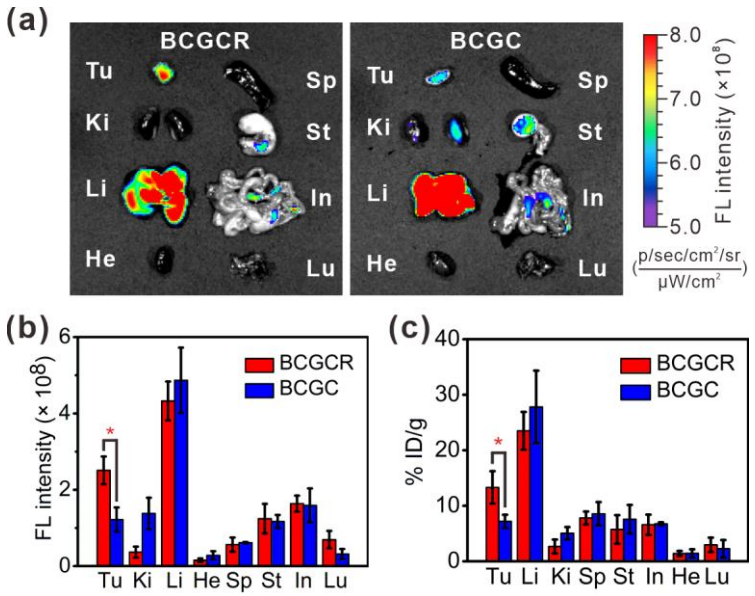

Figure 3-21. Biodistribution in U87MG tumors and main organs. (a) Fluorescence images of tumors and main organs resected from mice at 2 days after i.v. injection of BCGC or BCGCR (2 mg/kg, 50 μL) (Ex: 675 nm, Em: 720 nm). (b) Statistics of average FL intensity of tumors and main organs in (a). (c) Biodistribution (% ID/g) of BCGCR (red) or BCGC (blue) in main organs and U87MG tumor at 2 days after i.v. injection of BCGC (10 mg/kg Cu^{2+}) or BCGCR (10 mg/kg Cu^{2+}) determined via a quantification analysis of the amount of Cu^{2+} by ICP-AES. Tu: tumor; Ki: kidneys; Li: liver; He: heart; Sp: spleen; St: stomach; In: intestines; Lu: lungs. Values denote the mean ± SD (n = 3, **P* < 0.05).

3.3.6 *In vivo* synergetic PTT and enhanced CDT of tumor xenografts

Guided by precise fluorescence/MR bimodal imaging, synergetic PTT and enhanced CDT of U87MG tumors was conducted in living mice that received the i.v. injection of PBS (200 μL) or BCGCR (5 mg/kg Cu^{2+}, 200 μL), followed by exposure (or non-exposure) to 980 nm laser irradiation (0.8 W/cm^2) for 10 min when the accumulation of BCGCR in the tumor peaked (2 days later) (Figure 3-22a). Real-time thermal images, as well as the corresponding temperature variation of the tumors were recorded using an infrared (IR) thermal camera (Figure 3-22b&c). It is clear that the tumor temperature in BCGCR-treated mice was promptly enhanced from ~31.7°C to ~51.8°C after laser irradiation for 5 min, which was higher than that in PBS-treated mice (~37.3°C). This hyperthermia could cause tremendous damage to tumor tissues in living mice.

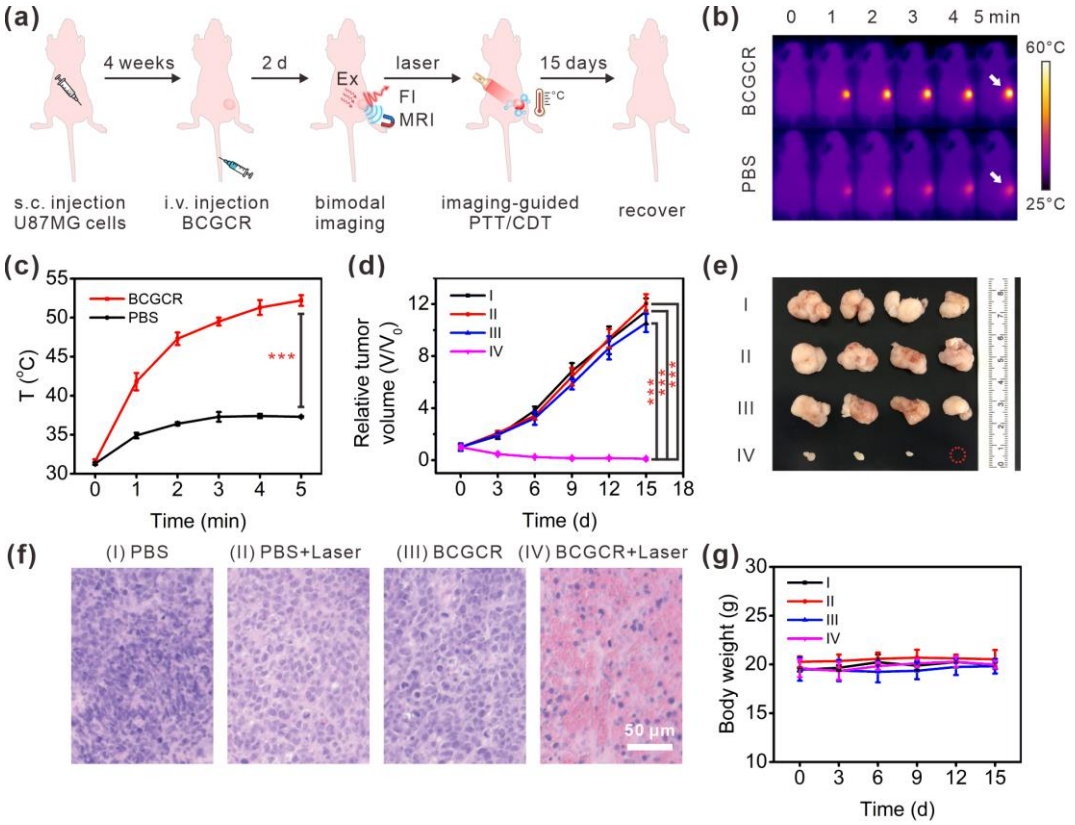

Figure 3-22. Synergetic PTT and intensified CDT of tumors *in vivo*. (a) Schematic illustration of the process of fluorescence/MR bimodal imaging-guided synergetic PTT/CDT of U87MG tumors in living mice. (b) IR thermal images of U87MG tumors in living mice during exposure to 980 nm laser irradiation (0.8 W/cm^2) for 0-5 min at

2 days after i.v. injection of PBS (200 μL) or BCGCR (5 mg/kg Cu^{2+}, 200 μL). White arrows indicate the tumor locations in mice. (c) Average temperature variations of the tumor with time in (b). (d) Relative tumor volume variation in living mice with time after treatments with (I) PBS (200 μL), (II) PBS (200 μL) + laser (0.8 W/cm^2, 10 min), (III) BCGCR (5 mg/kg Cu^{2+}, 200 μL) and (IV) BCGCR (5 mg/kg Cu^{2+}, 200 μL) + laser (0.8 W/cm^2, 10 min). (e) Photograph of tumors resected from mice on the 15^{th} day after the indicated treatments. (f) H&E staining of U87MG tumor slices resected from mice on the 2^{nd} day after indicated treatments. (g) Average body weight variation of mice with time after the indicated treatments. Values denote the mean ± SD (n = 4, ***$P < 0.001$).

We finally evaluated the curative efficacy after the indicated treatments. By measuring the tumor volumes within 15 days after treatment, we found that the tumor growth was successfully inhibited in the case of BCGCR-treated mice followed by laser irradiation, whereas tumor volumes from other groups (I-III) still expanded rapidly (Figure 3-22d). We verified, using a photograph of tumors dissected on the 15^{th} day, that after BCGCR plus laser treatment tumors were much smaller in comparison to the control groups (Figure 3-22e). A histopathological study by hematoxylin and eosin (H&E) staining of tumor tissue slices on the 2^{nd} day after treatment implies that BCGCR plus laser treatment induced tumor necrosis relative to the other three groups (Figure 3-22f). The dose and laser output required for this therapeutic effect were similar to those from previous reports, indicating the potential application of CuS NPs as a photo-assisted tumor therapy agent (Table 3-2).

To assess the *in vivo* toxicity, H&E staining of tissue slices of major resected organs (heart, lungs, liver, spleen and kidneys) was conducted at the end of each treatment, which reveals no apparent pathological variation (Figure 3-23). The Hematological assay of mice at 15 days post-injection indicates negligible differences between BCGCR treated mice and PBS treated ones (Figure 3-24). Moreover, there was no distinct change in the body weight of mice among these four groups after each treatment (Figure 3-22g). These results demonstrate that BCGCR featured synergetic

PTT and intensified CDT against U87MG tumors *in vivo*, as well as excellent biocompatibility in living mice.

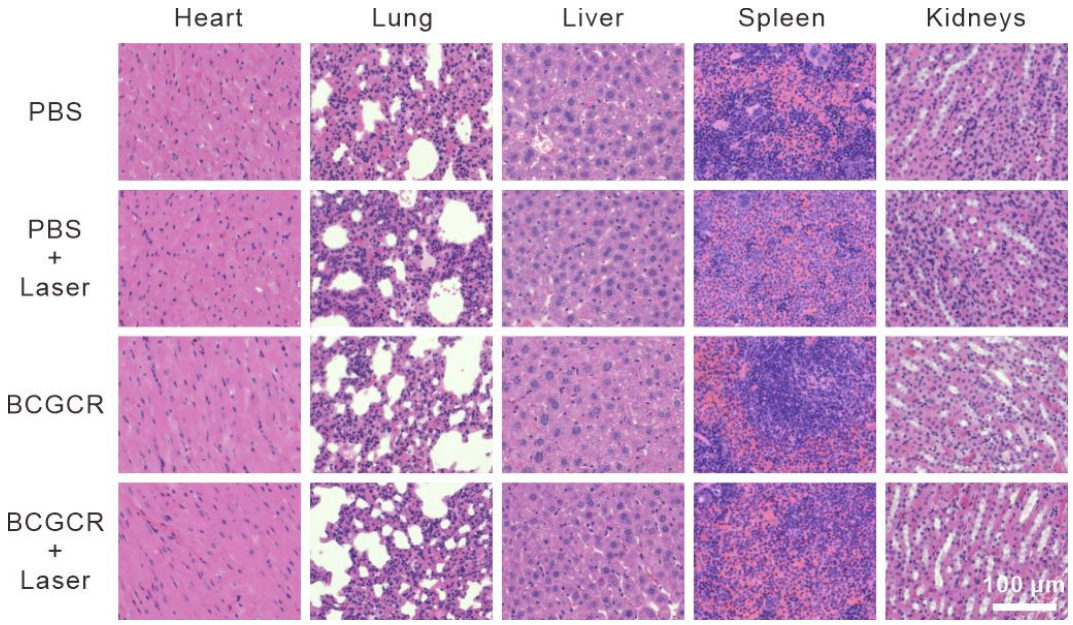

Figure 3-23. H&E-stained images of major organs including the heart, lungs, liver, spleen and kidneys resected from mice on the 15th day after the indicated treatments.

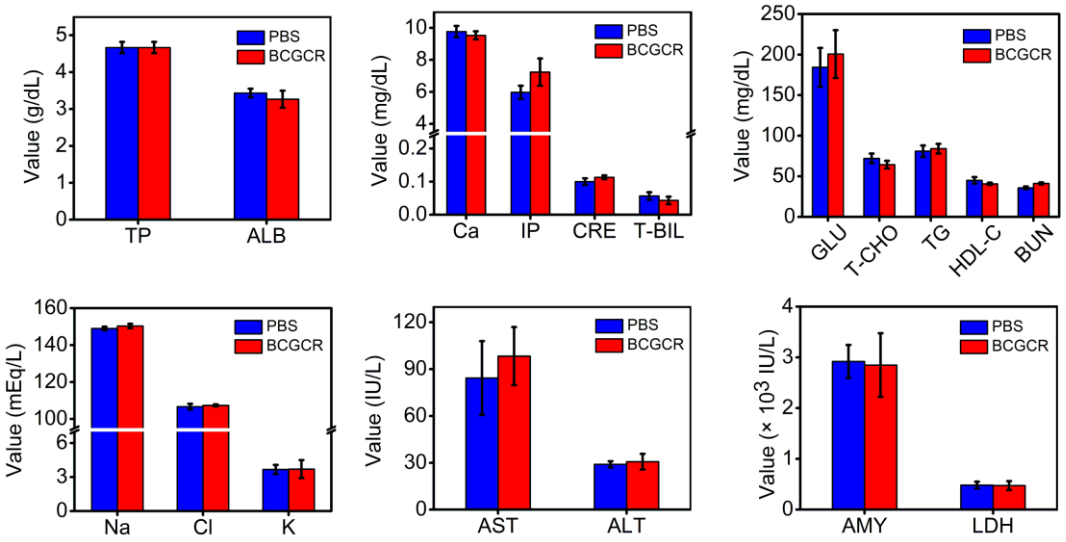

Figure 3-24. Blood routine examinations of mice at 15 days post-injection of 100 μL PBS or BCGCR (5 mg/kg Cu^{2+}).

Table 3-2. Comparison of treatment conditions between reported CuS NPs and BCGCR for tumor therapy.

CuS NPs	Therapy	Tumor cell line	Dose (mg/kg)	Irradiation		Power density (W/cm^2)	Reference
				λ[a] (nm)	Time (min)		
Gd:CuS@BSA	PTT	SK-OV-3	10	980	5	0.8	30
Gd_2O_3/CuS NDs	PTT	4T1	4.8	785	5	1.5	29
T-MAN	PTT	MKN45	5	808	10	0.8	21
PFN	PTT/CDT	Panc02	20	1064	5	1.0	27
BSA@CuS@DOX	PTT/CT[b]	4T1	3 for DOX	1064	6	1.2	50
Gd/CuS@PEI-FA-PS	PTT	KB-LFAR	~3.5	1064	10	0.6	51
IONF@CuS	MHT[c]/PTT	PC3	~0.32[d]	1064	10	1.0	52
RGD-CuS DENPs	PTT/gene	MDA-MB-231	~1.4	1064	5	0.6	53
CuSCDs	PTT	4T1	5[e]	808	5	0.3	54
CuS-MnS_2	PDT/PTT	A2780	~0.56[d]	808	10	1.0	55
Cu_2MnS_2	PTT	S180	20	1064	10	0.6	56
HCuS@Cu_2S@Au	PTT	U87MG	13	808	5	0.8	57
BCGCR	**PTT/CDT**	**U87MG**	**5**	**980**	**10**	**0.8**	**This work**

[a]λ: wavelength; [b]CT: chemotherapy; [c]MHT: magnetic hyperthermia; [d]i.t. injection; [e]injection every two days.

3.4 Conclusion

In summary, a multifunctional tumor-targeted nanoprobe (BCGCR) was developed by embellishing BSA-capped magnetic semiconductor CuS/Gd_2O_3 NPs, and we demonstrated the feasibility of fluorescence/MR bimodal imaging-guided synergetic PTT and intensified CDT of tumors in living mice. The as-prepared BCGCR exhibited intense NIR fluorescence and satisfactory r_1 relaxivity, permitting *in vivo* bimodal imaging of tumors with high sensitivity and spatial resolution. Furthermore, BCGCR possessed a high PCE (30.3%) under 980 nm laser irradiation, which could effectively generate hyperthermia to ablate tumors. On the other hand, a Cu-induced Fenton-like reaction was also promoted to produce abundant ROS in the hyperthermal TME, resulting in oxidative damage to tumors. As a result of this synergistic effect, tumor xenografts in mice were eliminated under guidance by imaging. This study reveals the ability of BCGCR for dual modality imaging and PTT assisted with enhanced CDT of U87MG tumors, which may also be applicable to other malignant tumors as a precise theranostics agent. This strategy is expected to be adopted in the design of other nanoprobes for multimodal imaging, as well as in synergetic therapies for advanced cancer theranostics.

3.5 References

[1] Aggarwal, V.; Tuli, H. S.; Varol, A.; Thakral, F.; Yerer, M. B.; Sak, K.; Varol, M.; Jain, A.; Khan, M. A.; Sethi, G. *Biomolecules* **2019**, *9*, 735.

[2] Yang, B.; Chen, Y.; Shi, J. *Chem. Rev.* **2019**, *119*, 4881-4985.

[3] Jin, H.; Zhu, T.; Huang, X.; Sun, M.; Li, H.; Zhu, X.; Liu, M.; Xie, Y.; Huang, W.; Yan, D. *Biomaterials* **2019**, *211*, 68-80.

[4] Hu, P.; Wang, R.; Zhou, L.; Chen, L.; Wu, Q.; Han, M.; El-Toni, A. M.; Zhao, D.; Zhang, F. *Anal. Chem.* **2017**, *89*, 3492-3500.

[5] Lan, M.; Zhao, S.; Liu, W.; Lee, C.; Zhang, W.; Wang, P. *Adv. Healthcare Mater.* **2019**, *8*, 1900132.

[6] Yue, J.; Shen, Y.; Liang, L.; Cong. L.; Xu, W.; Shi, W.; Liang, C.; Xu, S. *Anal. Chem.* **2020**, *92*, 6081-6087.

[7] Zhang, C.; Xia, D.; Liu, J.; Huo, D.; Jiang, X.; Hu, Y. *Adv. Funct. Mater.* **2020**, *30*, 2000189.

[8] Yi, X.; Hu, J.; Dai, J.; Lou, X.; Zhao, Z.; Xia, F.; Tang, B. Z. *ACS Nano* **2021**, *15*, 3026-3037.

[9] An, R.; Cheng, X.; Wei, S.; Hu, Y.; Sun, Y.; Huang, Z.; Chen, H.; Ye, D. *Angew. Chem.* **2020**, *132*, 20817-20825.

[10] Zhang, L.; Wang, S.; Li, C.; Xu, L.; Cheng, H.; Zhang, X. *Nano Lett.* **2018**, *18*, 7609-7618.

[11] Lin, L.; Song, J.; Song, L.; Ke, K.; Liu, Y.; Zhou, Z.; Shen, Z.; Li, J.; Yang, Z.; Tang, W.; Niu, G.; Yang, H.; Chen, X. *Angew. Chem. Int. Ed.* **2018**, *57*, 4902-4906.

[12] Ma, B.; Wang, S.; Liu, F.; Zhang, S.; Duan, J.; Li, Z.; Kong, Y.; Sang, Y.; Liu, H.; Bu, W.; Li, L. *J. Am. Chem. Soc.* **2019**, *141*, 849-857.

[13] Duesterberg, C. K.; Mylon, S. E.; Waite, T. D. *Environ. Sci. Technol.* **2008**, *42*, 8522-8527.

[14] Brillas, E.; Baños, M. A.; Camps, S.; Arias, C.; Cabot, P. L.; Garrido, J. A.; Rodríguez, R. M. *New J. Chem.* **2004**, *28*, 314-322.

[15] Liu, Y.; Wu, J.; Jin, Y.; Zhen, W.; Wang, Y.; Liu, J.; Jin, L.; Zhang, S.; Zhao, Y.; Song, S.; Yang, Y.; Zhang, H. *Adv. Funct. Mater.* **2019**, *29*, 1904678.

[16] Liu, C.; Wang, D.; Zhang, S.; Cheng, Y.; Yang, F.; Xing, Y.; Xu, T.; Dong, H.; Zhang, X. *ACS Nano* **2019**, *13*, 4267-4277.

[17] Zhong, X.; Wang, X.; Cheng, L.; Tang, Y.; Zhan, G.; Gong, F.; Zhang, R.; Hu, J.; Liu, Z.; Yang, X. *Adv. Funct. Mater.* **2020**, *30*, 1907954.

[18] Zhang, C.; Jing, X.; Guo, L.; Cui, C.; Hou, X.; Zuo, T.; Liu, J.; Shi, J.; Liu, X.; Zuo, X.; Li, J.; Chang, C.; Fan, C.; Wang, L. *Nano Lett.* **2021**, *21*, 5834-5841.

[19] Yan, H.; Chen, J.; Li, Y.; Bai, Y.; Wu, Y.; Sheng, Z.; Song, L.; Liu, C.; Zhang, H. *Biomater. Sci.* **2019**, *7*, 92-103.

[20] Zhang, L.; Gao, S.; Zhang, F.; Yang, K.; Ma, Q.; Zhu, L. *ACS Nano* **2014**, *8*, 12250-12258.

[21] Shi, H.; Sun, Y.; Yan, R.; Liu, S.; Zhu, L.; Liu, S.; Feng, Y.; Wang, P.; He, J.; Zhou, Z.; Ye, D. *Nano Lett.* **2019**, *19*, 937-947.

[22] Jiang, W.; Zhang, H.; Wu, J.; Zhai, G.; Li, Z.; Luan, Y.; Garg, S. *ACS Appl. Mater. Interfaces* **2018**, *10*, 34513-34523.

[23] Hu, J.; Cheng, Y.; Zhang, X. *Nanoscale* **2018**, *10*, 22657-22672.

[24] Sun, H.; Zhang, Q.; Li, J.; Peng, S.; Wang, X.; Cai, R. *Nano Today* **2021**, *37*, 101073.

[25] Li, X.; Zhang, D.; Yin, C.; Lu, G.; Wan, Y.; Huang, Z.; Tan, J.; Li, S.; Luo, J.; Lee, C. *ACS Appl. Mater. Interfaces* **2021**, *13*, 15983-15991.

[26] Zhang, R.; Wang, Z.; Xu, L.; Xu, Y.; Lin, Y.; Zhang, Y.; Sun, Y.; Yang, G. *Anal. Chem.* **2019**, *91*, 12476-12483.

[27] Sun, H.; Zhang, Y.; Chen, S.; Wang, R.; Chen, Q.; Li, J.; Luo, Y.; Wang, X.; Chen, H. *ACS Appl. Mater. Interfaces* **2020**, *12*, 30145-30154.

[28] Liu, C.; Tang, H.; Zheng, X.; Yang, D.; Zhang, Y.; Zhang, J.; Kankala, R. K.; Wang, S.; Liu, G.; Chen, A. *ACS Appl. Mater. Interfaces* **2020**, *12*, 40673-40683.

[29] Wen, R.; Lv, X.; Yang, T.; Li, Y.; Tang, Y.; Bai, X.; Ke, H.; Shen, J.; Chen, H. *Sci. China Mater.* **2017**, *60*, 554-562.

[30] Yang, W.; Guo, W.; Le, W.; Lv, G.; Zhang, F.; Shi, L.; Wang, X.; Wang, J.; Wang, S.; Chang, J.; Zhang, B. *ACS Nano* **2016**, *10*, 10245-10257.

[31] Tanford, C.; Buzzell, J. G.; Rands, D. G.; Swanson, S. A. *J. Am. Chem. Soc.* **1955**, *77*, 6421-6428.

[32] Yukawa, H.; Baba, Y. *Anal. Chem.* **2017**, *89*, 2671-2681.

[33] Yukawa, H.; Watanabe, M.; Kaji, N.; Okamoto, Y.; Tokeshi, M.; Miyamoto, Y.; Noguchi, H.; Baba, Y.; Hayashi, S. *Biomaterials* **2012**, *33*, 2177-2186.

[34] Zhang, C.; Yuan, Y.; Wu, K.; Wang, Y.; Zhu, S.; Shi, J.; Wang, L.; Li, Q.; Zuo, X.; Fan, C.; Chang, C.; Li, J. *Nano Lett.* **2022**, *22*, 468-475.

[35] Li, W.; Wang, C.; LV, H.; Wang, Z.; Zhao, M.; Liu, S.; Gou, L.; Zhou, Y.; Li, J.; Zhang, J.; Li, L.; Wang, Y.; Lou, P.; Wu, L.; Zhou, L.; Chen, Y.; Lu, Y.; Cheng, J.; Han, Y.; Cao, Q.; Huang, W.; Tong, N.; Fu, X.;Liu, J.; Zheng, X.; Berggren, P. *ACS*

Nano **2021**, *15*, 18237-18249.

[36] Nishinaga, Y.; Sato, K.; Yasui, H.; Taki, S.; Kazuomi, T.; Shimizu, M.; Endo, R.; Koike, C.; Kuramoto, N.; Nakamura, S.; Fukui, T.; Yukawa, H.; Baba, Y.; Kaneko, M. K.; Chen-Yoshikawa, T. F.; Kobayashi, H.; Kato, Y.; Hasegawa, Y. *Cells* **2020**, *9*, 1019.

[37] Wahsner, J.; Gale, E. M.; Rodríguez-Rodríguez, A.; Caravan, P. *Chem. Rev.* **2019**, *119*, 957-1057.

[38] Caspani, S.; Magalhães, R.; Araújo, J. P.; Sousa, C. T. *Materials* **2020**, *13*, 2586.

[39] Zhou, Z.; Deng, H.; Yang, W.; Wang, Z.; Lin, L.; Munasinghe, J.; Jacobson, O.; Liu, Y.; Tang, L.; Ni, Q.; Kang, F.; Liu, Y.; Niu, G.; Bai, R.; Qian, C.; Song, J.; Chen, X. *Nat. Commun.* **2020**, *11*, 3032.

[40] Wu, B.; Lu, S.; Yu, H.; Liao, R.; Li, H.; Zafitatsimo, B. V. L.; Li, Y.; Zhang, Y.; Zhu, X.; Liu, H.; Xu, H.; Huang, S.; Cheng, Z. *Biomaterials* **2018**, *159*, 37-47.

[41] Danhier, F.; Breton, A. L.; Préat, V. *Mol. Pharmaceutics* **2012**, *9*, 2961-2973.

[42] Temming, K.; Schiffelers, R. M.; Molema, G.; Kok, R. J. *Drug Resist. Update.* **2005**, *8*, 381-402.

[43] Tang, W.; Gao, H.; Ni, D.; Wang, Q.; Gu, B.; He, X.; Peng, W. *J. Nanobiotechnol.* **2019**, *17*, 68.

[44] Herborn, C. U.; Honold, E.; Wolf, M.; Kemper, J.; Kinner, S.; Adam, G.; Barkhausen, J. *Invest. Radiol.* **2007**, *42*, 58-62.

[45] Kuang, Y.; Cao, Y.; Liu, M.; Zu, G.; Zhang, Y.; Zhang, Y.; Pei, R. *ACS Appl. Mater. Interfaces* **2018**, *10*, 26099-26107.

[46] Wang, L.; Lin, H.; Ma, L.; Sun, C.; Huang, J.; Li, A.; Zhao, T.; Chen, Z.; Gao, J. *J. Mater. Chem. B* **2017**, *5*, 8004-8012.

[47] Younis, M. R.; Wang, C.; An, R.; Wang, S.; Younis, M. A.; Liu, Z.; Wang, Y.; Ihsan, A.; Ye, D.; Xia, X. *ACS Nano* **2019**, *13*, 2544-2557.

[48] Ren, W.; Yan, Y.; Zeng, L.; Shi, Z.; Gong, A.; Schaaf, P.; Wang, D.; Zhao, J.; Zou, B.; Yu, H.; Chen, G.; Brown, E. M. B.; Wu, A. *Adv. Healthcare Mater.* **2015**, *4*,

1526-1536.

[49] Liu, Y.; Ai, K.; Liu, J.; Deng, M.; He, Y.; Lu, L. *Adv. Mater.* **2013**, *25*, 1353-1359.

[50] Zhu, L.; Gao, D.; Xie, L.; Dai, Y.; Zhao, Q. *Mol. Pharmaceutics* **2020**, *17*, 3720-3729.

[51] Zhang, C.; Sun, W.; Wang, Y.; Xu, F.; Qu, J.; Xia, J.; Shen, M.; Shi, X. *ACS Appl. Mater. Interfaces* **2020**, *12*, 9107-9117.

[52] Curcio, A.; Silva, A. K. A.; Cabana, S.; Espinosa, A.; Baptiste, B.; Menguy, N.; Wilhelm, C.; Abou-Hassan, A. *Theranostics* **2019**, *9*, 1288-1302.

[53] Ouyang, Z.; Li, D.; Xiong, Z.; Song, C.; Gao, Y.; Liu, R.; Shen, N.; Shi, X. *ACS Appl. Mater. Interfaces* **2021**, *13*, 6069-6080.

[54] Yu, Y.; Song, M.; Chen, C.; Du, Y.; Li, C.; Han, Y.; Yan, F.; Shi, Z.; Feng, S. *ACS Nano* **2020**, *14*, 10688-10703.

[55] Chen, W.; Wang, X.; Zhao, B.; Zhang, R.; Xie, Z.; He, Y.; Chen, A.; Xie, X.; Yao, K.; Zhong, M.; Yuan, M. *Nanoscale* **2019**, *11*, 12983.

[56] Ke, K.; Yang, W.; Xie, X.; Liu, R.; Wang, L. L.; Lin, W. W.; Huang, G.; Lu, C. H.; Yang, H. H. *Theranostics* **2017**, *7*, 4763-4776.

[57] Deng, X.; Li, K.; Cai, X.; Liu, B.; Wei, Y.; Deng, K.; Xie, Z.; Wu, Z.; Ma, P.; Hou, Z. *Adv. Mater.* **2017**, *29*, 1701266.

[58] Chen, X.; Conti, P. S.; Moats, R. A. *Cancer Res.* **2004**, *64*, 8009-8014.

[59] Robinson, J. T.; Tabakman, S. M.; Liang, Y.; Wang, H.; Casalongue, H. S.; Vinh, D.; Dai, H. *J. Am. Chem. Soc.* **2011**, *133*, 6825-6831.

[60] Tang, Z.; Zhang, H.; Liu, Y.; Ni, D.; Zhang, H.; Zhang, J.; Yao, Z.; He, M.; Shi, J.; Bu, W. *Adv. Mater.* **2017**, *29*, 1701683.

Chapter 4: Summary and perspectives

In this thesis, we focus on the development of versatile NPs for imaging and novel photo-assisted therapy of tumors. First, we report a fluorescent and magnetic nanoprobe (QMNP-RGD) for bimodal imaging of *in vitro* tumor cells. The preparation of this multifunctional nanomaterial is divided into three steps. First, commercial quantum dots (QDs) with high fluorescence intensity are covalently modified with an RGD peptide, which can facilitate the tumor cell uptake by $\alpha_v\beta_3$ integrin-induced active recognition. Superparamagnetic iron oxide (SPIO) nanoparticles (NPs) are then capped using a cationic polysaccharide to improve the stability. Integration is finally achieved by convenient electrostatic binding. We successfully demonstrated that QMNP-RGD can be efficiently delivered into U87MG cells and used for fluorescence/magnetic resonance (MR) bimodal imaging.

In addition, we report a multifunctional nanoprobe (BCGCR) integrating bimodal imaging and photothermal-enhanced CDT of the targeted tumor, which is produced by covalent conjugation of bovine serum albumin (BSA)-stabilized CuS/Gd_2O_3 nanoparticles (NPs) with Cy5.5 fluorophore and tumor-targeting ligand RGD. BCGCR exhibits intense near-infrared (NIR) fluorescence and acceptable r_1 relaxivity ($\sim$15.3 mM^{-1} s^{-1}) for both sensitive fluorescence imaging (FI) and high-spatial-resolution magnetic resonance imaging (MRI) of tumors in living mice. Moreover, owing to the strong NIR absorbance from the internal CuS NPs, BCGCR can generate localized heat and displays a high photothermal conversion efficiency (PCE, 30.3%) under 980 nm laser irradiation, which enables photothermal therapy (PTT) and further intensifies ROS generation arising from the Cu-induced Fenton-like reaction for enhanced CDT. This synergetic effect shows such excellent therapeutic efficacy that it can ablate xenografted tumors *in vivo*.

We believe that the strategy of integrating different components with respective function, such as electrostatic binding, encapsulation and covalent modification, will be beneficial to exploring other advanced nanomaterials for the clinical application of multimodal imaging-guided synergetic cancer therapies.